



HAL
open science

Electronic structures, quasi-particle and gap dynamics in copper oxides superconductors using Time and Angle Resolved Photoemission Spectroscopy

Zailan Zhang

► **To cite this version:**

Zailan Zhang. Electronic structures, quasi-particle and gap dynamics in copper oxides superconductors using Time and Angle Resolved Photoemission Spectroscopy. Physics [physics]. Université Pierre et Marie Curie - Paris VI, 2017. English. NNT : 2017PA066126 . tel-01653083

HAL Id: tel-01653083

<https://theses.hal.science/tel-01653083>

Submitted on 1 Dec 2017

HAL is a multi-disciplinary open access archive for the deposit and dissemination of scientific research documents, whether they are published or not. The documents may come from teaching and research institutions in France or abroad, or from public or private research centers.

L'archive ouverte pluridisciplinaire **HAL**, est destinée au dépôt et à la diffusion de documents scientifiques de niveau recherche, publiés ou non, émanant des établissements d'enseignement et de recherche français ou étrangers, des laboratoires publics ou privés.

Université Pierre et Marie Curie

Physique et Chimie des Matériaux (ED397)

Institut de minéralogie, de physique des matériaux et de cosmochimie

**Electronic structures, quasi-particle and gap
dynamics in copper oxides superconductors using
Time and Angle Resolved Photoemission
Spectroscopy**

Par Zailan ZHANG

Thèse de doctorat de physique

Dirigée par Matteo d'Astuto et Luca Perfetti

Présentée et soutenue publiquement le 29 Mai 2017

Devant un jury composé de:

M. SIROTTI Fausto	Directeur de recherche	Rapporteur
M. SANTANDER Andrés	Maître de conférences, HDR	Rapporteur
M. LÜNING Jan	Professeur UPMC	Examineur
Mme. BROUET Véronique	Directeur de recherche	Examineur
Mme. DECORSE Claudia	Maître de conférences	Examineur
Mme. ROY Pascale	Directeur de recherche	Examineur
M. NOAT Yves	Chargé de recherche	Examineur
M. D'ASTUTO Matteo	Chargé de recherche, HDR	Directeur de thèse
M. PERFETTI Luca	Professeur Ecole Polytechnique	Directeur de thèse



Acknowledgment

First of all, I would like to show my sincere appreciation to my supervisor Dr. Matteo d'Astuto. Thank him for giving me the opportunity to work on this interesting project of thesis; thank him for the kind help in my life in the difficult period when I just arrived in France without any knowledge of French. As the initiator of this project, his trust and patience in me have guided me throughout the thesis and the redaction of the present work. His sharp vision on topic has given me lots of inspirations to carry on the research in this and related fields.

As a thesis co-supervisor, Prof. Luca Perfetti supported me in all stages of this work. He always gave me constant encouragement and advice. I am especially indebted to him for his patient explanation that gave me the basic knowledge of laser system, UHV techniques, Tr-ARPES etc during that time in Femto ARPES lab; for continuous help and support during the last four years, for teaching me how to do the Tr-ARPES experiments, for doing the experiments and analyzing the data together with me; especially on the writing of thesis and paper. His enthusiasm and constant flow of exciting ideas for the experiments were and will continue to be an inspiration to me.

I express my gratitude to Christian Piovera, Evangelis Papalazarou and Julian Mauchain and all the other members in FemtoARPES lab, for their technical support and their helpful discussions and assistance concerning procedure questions and the setup problems.

I have to thank to all the members of IMPMC, for their hospitality, scientific guidance and the great atmosphere. I also want to express my thanks to all the group members: Andrea Gauzzi, Christophe Bellin, Yannick Klein, Yann le Godec, Oleksandr Kurakevych, Geneviève Loupiau, Hicham Moutaabbid and William Sacks, the PhD students: Blair Lebert, Zied Jouini, Marine Verseils, Gilbert Umugabe Hancheng Yang, for their supporting and discussion in experiments results.

I am also grateful to the jury members: M. SIROTTI Fausto, M. SANTANDER Andrés, M. LÜNING Jan, Mme. BROUET, Véronique, Mme. DECORSE Claudia, Mme. ROY Pascale and M. NOAT Yves, for their interest in the work, their proofreading and commenting on the manuscript and suggestion and constructive criticism.

At last, I would like to thank my family, my parents and sisters, for all their love and support. Mostly, I have to thank my husband, Zhesheng Chen, who believes in me and supports me unconditionally during four years. I also want to thank my little, cute son, Zhenyu, giving me so much happiness and making my life colorful.

Résumé

Les supraconducteurs à base d'oxyde de cuivre ont fait l'objet d'études approfondies mais ils restent toujours au centre de nombreux débats. Après 30 années de recherche, certaines questions scientifiques ont été éclairées, alors que d'autres restent controversées. L'évolution du paramètre d'ordre supraconducteur avec la température et le dopage en est un cas exemplaire. Les propriétés d'équilibre des supraconducteurs de cuprates ont été déterminées par un nombre impressionnant de techniques différentes. Dans la phase supraconductrice, les quasi-particules sont bien définies aux antinodes et génèrent un gap électronique avec la symétrie d-wave [Has14, Kan07]. La phase normale de ces composés présente un pseudo-gap antinodale dont l'origine est encore discutée [Nor05]. Contrairement aux supraconducteurs classiques, les cuprates présentent une structure en couches et une interaction d'appariement s'étendant sur quelques mailles élémentaires. Par conséquent, les effets précurseurs du condensat supraconducteur peuvent être observés légèrement au-dessus de la température de transition T_c [Rull11, Ber10, Wan05, Per15]. Dans cette région critique, les variations d'amplitude du paramètre d'ordre reproduisent la plupart des résultats expérimentaux.

La question de l'existence de paires de Cooper incohérentes loin des conditions d'équilibre est au centre de mon travail de thèse. De nombreuses expériences de pompe-sonde ont déjà observé la dynamique du condensat dans les cuprates. Il est reconnu que la supraconductivité se rétablit en plusieurs picosecondes et que cette échelle de temps dépend de la fluence dans un régime d'excitation faible [Dem99, Seg02]. Ces résultats ont été confirmés en mesurant la réponse inductive des supercourants [Kai05] et le spectre des excitations électroniques [Sma12, Sma14]. Une équation maîtresse phénoménologique pourrait très bien expliquer le retour de la supraconductivité dans le régime de perturbation faible [Kai05, Kab05]. Néanmoins, l'état photo-excité généré par des impulsions optiques intenses est encore assez mal compris. Apparemment, la dynamique de la réflectivité transitoire montre un canal de relaxation rapide uniquement si l'échantillon est au-dessus de T_c ou s'il est fortement photo-excité [Gia09, Tod11]. Au-dessous de T_c , l'absence de relaxation rapide suggère que les corrélations supraconductrices inhibent la dissipation des quasi-particules (QPs) [Gia09]. Time and Angle Resolved PhotoElectron Spectroscopy (tr-ARPES) a confirmé l'apparition d'une dynamique rapide uniquement dans le régime

d'excitation élevé de la phase supraconductrice [Cor11].

Dans la première étape de ma thèse, je montre qu'une analyse détaillée (tr-ARPES) de la dynamique des quasi-particules fournit une connaissance approfondie de l'état photoexcité. Nous effectuons des mesures de Angle Resolved PhotoEmission Spectroscopy (ARPES: Spectroscopie de photoémission résolue en angle) avec résolution temporelle de $\text{Bi}_2\text{Sr}_2\text{CaCu}_2\text{O}_{8+\delta}$ (Bi-2212) et $\text{Bi}_2\text{Sr}_{2-x}\text{La}_x\text{CuO}_{6+\delta}$ (Bi-2201) avec dopage optimale. La dynamique des électrons montre que la diffusion inélastique des quasi-particules nodales diminue lorsque la température est inférieure à la valeur critique de la transition de phase supraconductrice. Cette baisse de la dissipation des électrons est étonnamment stable et survit aux densités de photoexcitation beaucoup plus grandes que la valeur soutenue par la supraconductivité à longue portée. Le comportement non conventionnel de la diffusion de QPs est attribué à des corrélations supraconductrices qui apparaissent juste après la photo-excitation et s'étendent sur une échelle de longueur comparable au chemin inélastique. Parallèlement au refroidissement des QPs, nous analysons le décalage et l'élargissement du pic de quasiparticules. Nous proposons que le décalage temporel peut être un effet thermoélectrique lié à la température élevée des électrons juste après la photoexcitation.

Ensuite, nous présentons un étude détaillé de la gap électronique dans le $\text{Bi}_2\text{Sr}_2\text{CaCu}_2\text{O}_{8+\delta}$ (Bi-2212) avec dopage optimal. Au cours des dernières années, ce champ de recherche s'est enrichi par des protocoles expérimentaux capables de détecter les spectres électroniques hors des conditions d'équilibre [Per15, Sma12, Kam16]. Smallwood et al. ont rapporté l'effondrement et la récupération subséquente du gap de particule unique après photoexcitation par une courte impulsion laser [Sma12, Sma14]. Leurs données indiquent que le gap est plus stable lorsqu'on se dirige vers les antinodes. En outre, la fluence minimale nécessaire pour l'effondrement de la gap proche de la région nodale a été liée à un changement qualitatif dans la dynamique des quasi-particules (QPs). Juste après, Ishida *et al.*, en reproduisant le collapse de la gap électronique, ont observé les excitations de Bogoliubov et ont souligné une réduction simultanée de la cohérence des QPs [Ish16]. Apparemment, la récupération de la cohérence de phase se déroule en plusieurs picosecondes, en raison du refroidissement des électrons par émission de phonons. Dans la même échelle de temps, la dynamique d'un condensat en cours de

développement affecte également la réponse électromagnétique [Dem99, Kai05] et la population transitoire d'électrons chauds [Sma12]. En effet, le refroidissement des QPs indique un ralentissement drastique lorsque le système entre dans la phase supraconductrice [Pio15, Yan15]. Un tel effet persiste à une fluence de photoexcitation bien majeure de la valeur de seuil nécessaire pour la destruction de la densité superfluide. En conséquence, nous avons proposé qu'un appariement résidu pourrait protéger les QP de la dissipation d'énergie. Alternativement, Smallwood *et al.* ont développé un modèle qui expliquerait le refroidissement lent des QPs à la suite d'une ouverture dynamique de la gap électronique [Sma16].

Dans notre deuxième série d'expériences, nous avons utilisé des impulsions de sonde à bande étroite pour résoudre les détails fins de la fonction spectrale en tenant compte de la température, de la densité de photo-excitation et du temps de retard de l'impulsion de la pompe. Nos données de ARPES résolue en temps sur $\text{Bi}_2\text{Sr}_2\text{CaCu}_2\text{O}_{8+\delta}$, montrent que l'effondrement du gap dépend du moment. Nos résultats confirment les travaux antérieurs et étendent la recherche dans un régime de haute densité de photo-excitation. Le seuil de fluence nécessaire pour remplir complètement le gap dépend sensiblement de l'angle azimutal. Comme prévu, les paires de Cooper sont plus stable aux anti-nodes. Bien que les données dans la région anti-nodale ne soient pas encore disponibles, le travail en cours suggère que la signature spectrale de l'appariement est complètement perdu pour une fluence de F_{pair} . La dynamique des états photo-excités peut être obtenue en faisant varier le retard entre la pompe et le faisceau de sonde. Pour une large densité de photo-excitation, la gap électronique reste rempli pour ~ 1 ps et se rétablit avec un temps caractéristique de 4-5 ps. Nous avons comparé cette dépendance temporelle à la dissipation d'énergie des QPs. Fait intéressant, la relaxation des QPs développe une composante rapide à la fluence de seuil F_{pair} que est nécessaire pour un effondrement complet de la gap. Néanmoins, la relaxation des électrons chauds est affectée par les corrélations dynamiques d'une phase supraconductrice naissante. La comparaison entre les F_{pair} et la F_{phase} extraite par tr-THz a suggéré l'existence d'un régime de fluence dans laquelle les paires Cooper sont présentes, mais ne portent pas un courant superfluide. Des mesure de F_{pair} et de F_{phase} sur le même échantillon et avec la même source seraient obligatoire pour tirer des conclusions solides.

D'autre part, la nature du gap d'état normal (pseudo-gap) et sa relation avec la supraconductivité sont encore incertaines. De nombreuses expériences antérieures suggèrent que le pseudo-gap est distinct du gap supraconducteur et que le pseudogap est un gap unique d-wave. Une grande partie des données expérimentales suggère maintenant qu'au moins dans une petite région du diagramme de phase sous-dopé, il existe un état de symétrie brisée qui est distinct de la supraconductivité homogène. Dans la "famille 214", la phase de basse température est accompagnée d'un ordre de charge et de spin [Tra95, Zaa89]. Il a été proposé que ces modulations de la densité de charge et du spin pourraient être à l'origine de l'état de symétrie brisée, en prenant la forme de "stripes" [Kiv03], ou dans la forme d'onde de densité [Tor13]. Des expériences de diffusion sont possibles dans la région du diagramme de phase où ces modulations de charge deviennent statiques. Ceci ont suggéré que les "stripes" rivalisent avec la supraconductivité [Cha12, Com14, Net14], mais cette conclusion fait encore l'objet de débat [Kiv03]. On peut rendre statique l'ordre de charge du $\text{La}_{2-x}\text{Sr}_x\text{CuO}_{4+d}$ (LSCO) en remplaçant Sr avec Ba dans $\text{La}_{2-x}\text{Ba}_x\text{CuO}_{4+d}$ (LBCO), ou avec une substitution partielle de Nd sur le site La dans $\text{La}_{2-x-y}\text{Nd}_y\text{Sr}_x\text{CuO}_{4+d}$ (LNSCO). Généralement, l'ordre de charge statique supprime la supraconductivité dans une région étroite de dopage autour de $x = 1/8$ [Axe89]. Par contre, dans l'LSCO l'impact de la modulation de densité est mineur, ne causant qu'une légère dépression dans T_c au voisinage de $x = 1/8$ [Bil11]. He *et al.* [He09] à été étudié la nature du pseudo-gap sur LBCO proche du dopage $1/8$, en établissant une déviation prononcée par rapport à la simple forme de d-wave. Le lien entre le pseudo-gap anti-nodal et les modulations de charge (CDW/stripe phase) à été exploré par C. Matt et ses collègues par un étude ARPES du système $\text{La}_{1.6-x}\text{Nd}_{0.4}\text{Sr}_x\text{CuO}_4$ à dopage $1/8$ [Mat15]. Ces auteurs ont observé une différence de taux de diffusion des quasiparticules entre la phase LTT et la phase LTO dans la région anti-nodale. Ils ont interprétés ces résultats comme la signature de "stripes" sur les temps de vie des excitations électroniques. Plus récemment, la nature du pseudo-gap proche de nœuds a été étudiée dans le système LSCO 214 à faible dopage [Dra14]. Les auteurs ont montré qu'un gap nodal se forme à 30K et ils ont associé cette évolution électronique à la formation d'une ondes de densité de spin. En réalité, dans cuprates LSCO 214, le rôle des modulations de charge/spin ("stripes") sur les propriétés électroniques n'est toujours pas clair.

Dans cette thèse, nous montrons des mesures ARPES pour $\text{La}_{2-x}\text{Sr}_x\text{CuO}_{4+\delta}$ ($x=1/8$,

$y=0$, LSCO), $\text{La}_{2-x-y}\text{Nd}_y\text{Sr}_x\text{CuO}_{4+\delta}$ ($x=1/8$, $y=0.4$, LNSCO) et $\text{La}_{2-x}\text{Ba}_x\text{CuO}_{4+\delta}$ ($x=0.14$, LBCO). Ainsi nous nous proposons d'étudier la nature du pseudo-gap et sa relation avec la supraconductivité, le lien possible entre les modulations spin/charge et la dispersion des quasiparticules. Au chapitre 5, nous discutons les données ARPES dans LBCO et nous montrons que les propriétés électroniques près du nœud à un lien apparent avec la transition LTT-LTO. Les données suggèrent que un petit gap s'ouvre à la transition de phase. En plus, nous pouvons corrélérer la renormalisation de la structure de bande dans LBCO avec le ramollissement d'un phonon de la liaison Cu-O. En combinant le comportement de la partie imaginaire de la self-energy mesuré par ARPES avec le spectre des phonons, nous confirmons dans LBCO l'observation d'une connexion entre vecteur ondulatoire reliant les surfaces de Fermi FS anti-nodal et un mode phononique de la liaison Cu-O.

Néanmoins, beaucoup de problèmes restent encore à résoudre pour élucider pleinement les propriétés des cuprates High-Tc. Afin de comprendre le mécanisme d'appariement de la supraconductivité, non seulement les caractéristiques universelles, mais aussi l'origine des phénomènes dépendantes du matériau telles que un petit pseudo-gap nodal nécessitent une clarification.

Contents

1	Introduction	1
	Preface	1
	Structure of the thesis	2
1.1	Historical background.....	4
1.1.1	Fundamentals of superconductivity	4
1.1.2	Discovery of High Critical Temperature.....	5
1.2	Cuprate HTSCs.....	7
1.3	Superconductivity of Cuprates.....	13
1.3.1	Unconventional pairing symmetry.....	13
1.3.2	Pseudogap.....	15
1.3.3	Fluctuations of the superconducting order parameter	17
1.3.4	Competing or intertwined electronic ordered phases.....	21
1.3.5	The Electron-Boson coupling in HTSC	23
2	Experimental Techniques.....	29
2.1	Basic Principles.....	29
2.2	The Three-step and One-step Model of Photoemission	30
2.3	Angle-resolved Photoemission Spectroscopy.....	32
2.3.1	ARPES CASSIOPEE end station.....	38
2.4	Time- and Angle-Resolved Photoemission Spectroscopy	40
2.4.1	Experimental setup	45
2.5	Magnetisation Measurements Using a SQUID	49
2.6	Sample Preparation, Orientation and Cleaving Procedure	51
3	Time- and angle-resolved photoemission spectroscopy (Tr-ARPES)	
	study of the $\text{Bi}_2\text{Sr}_2\text{CaCu}_2\text{O}_{8+\delta}$.....	53
3.1	Time resolved Optical and THz measurements	53
3.2	Detection of quasiparticle dissipation rate by time resolved ARPES.....	58
3.3	Preparations and Experimental details.....	59
3.4	Quasiparticle dynamics in $\text{Bi}_2\text{Sr}_2\text{CaCu}_2\text{O}_{8+\delta}$	61
3.4.1	Redistribution of spectral weight in the Quasiparticle peak	61
3.4.2	Quasiparticle dissipation in the normal phase	62
3.4.3	Quasiparticles relaxation at different temperatures across the superconducting phase transition	65
3.4.4	Comparison of quasiparticles relaxation between Bi-2212 and Bi-2201	68
3.4.5	Quasiparticles relaxation at different photoexcitation densities	71

3.5 Pump-induced band shift and broadening in $\text{Bi}_2\text{Sr}_2\text{CaCu}_2\text{O}_{8+\delta}$ at high fluence	74
3.5.1 Experimental reports of transient shifts and quasiparticles broadening	74
3.5.2 Photoinduced changes of time resolved ARPES maps	76
3.5.3 Pump-induced band shift	79
3.5.4 Pump-induced band broadening.....	82
3.6 Conclusions	84
4 Time- and momentum-resolved gap dynamics in $\text{Bi}_2\text{Sr}_2\text{CaCu}_2\text{O}_{8+\delta}$...	85
4.1 Introduction	85
4.2 Near nodal gap	90
4.2.1 The near-nodal superconducting gap in the equilibrium state	91
4.2.2 The near nodal gap in the photoexcited state at low pump fluence	93
4.2.3 Pump fluence dependence of the near nodal nonequilibrium gap in the photoexcited state	94
4.2.4 The dynamics of the near nodal transient gap at high pump fluence	96
4.3 Off nodal gap	98
4.3.1 The off nodal dispersion in the photoexcited state at high pump fluence	98
4.3.2 Pump fluence dependence of the off nodal nonequilibrium gap in the photoexcited state	99
4.3.3 The dynamics of the off nodal transient gap at high pump fluence	100
4.4 Momentum and pump fluence dependence of the nonequilibrium gap in the photoexcitation state	102
5 Angle resolved photoemission spectroscopy study of the $\text{La}_{2-x-y}\text{Nd}_y\text{M}_x\text{CuO}_4$ (M=Sr, Ba; $x=0.12-0.14$; $y=0,0.4$) high temperature superconductor	105
5.1 Motivation	105
5.2 Preparations and Measurements	110
5.2.1 ARPES Data Treatment:	111
5.3 Results of the study	113
5.3.1 The LSCO results at the critical doping $x = 0.12$	113
5.3.2 The LNSCO results at the critical doping $x = 0.12$	117
5.3.3 The LBCO results at doping $x = 0.14$	122
5.3.3.1 Temperature and angle resolved dependence of the pseudo-gap	122
5.3.3.2 Angle resolved dependence of the kink and possible scattering kinetics	128
5.4 Discussion of the results	134
6 Conclusion and Outlook	136
Bibliography	138

Chapter 1

Introduction

Preface

High temperature superconductivity in the copper-oxide based doped antiferromagnetic insulators has presented the foremost challenge in solid state physics since the discovery of the primordial compound $\text{La}_{2-x}\text{Ba}_x\text{CuO}_4$ in 1986. After three decades, much has been learned about the novel forms of quantum matters that exhibited in these strongly correlated electron system. A detailed understanding of the unconventional properties of copper oxides superconductors has been achieved, in particular using different spectroscopy techniques. It is now well established that the single particle gap near the nodal direction is a hallmark of phase coherent superconductivity. Moreover a remnant pairing persists up to temperatures higher than the critical value T_c . However, unresolved issues include the complexity of the phase diagram, the unprecedented prominence of various forms of collective fluctuations, and the simplicity and insensitivity to material detail of the normal state at elevated temperature, and, above all, the very mechanism leading to the superconducting state in cuprates.

In the last years, the field has been enriched by experimental protocols that are capable of detecting the single particle spectra out of equilibrium conditions. Such

techniques can be helpful to identify in the time domain distinct mechanisms having close energy scales. In particular, the present work aims to explore the possibility that an intense photoexcitation of the superconductor can generate a state with incoherent copper pairs and no superfluid density. In this thesis, we report a systematic Time-resolved ARPES study of the optimally doped $\text{Bi}_2\text{Sr}_2\text{CaCu}_2\text{O}_{8+\delta}$. The employed experimental methods allow us to measure the dynamics of non-equilibrium electrons and of the superconducting gap, providing complementary information to conventional ARPES and optics.

A second major challenge in the physics of HTSCs is the poor understanding of the normal phase at high temperature. Several experiments underlined the strong deviations from a Fermi liquid behavior at low doping level, as well as the presence of fluctuating orders. These density waves affect the electronic properties of the material and often leave clear signatures in the response functions. The second half of this thesis is devoted to the ARPES study of the so-called stripes state, a spatially modulated superconducting state that is suggested to exist in some of the cuprates above the superconducting transition temperature. The presence of fluctuating stripes should have an impact on the pseudogap. We use the ARPES to study the effects of competing orders on spectral function and on the scattering rate of electronic states near E_F .

Structure of the thesis

The thesis will be organized in the following way.

Chapter 1 provides a broad introduction to high temperature superconductivity, with a main focus on the aspects relevant to my results. I introduce the basic concepts and the main open question in the field of cuprates, as well as more exotic phenomena explored throughout the thesis. In particular, the different scenarios for the phase diagram are discussed.

Chapter 2 describes the two experimental techniques: angle resolved photoemission spectroscopy (ARPES) and Time-resolved Angle-resolved photoemission spectroscopy (Tr-ARPES) used in thesis.

Chapter 3 reports on the non-equilibrium physics of BSCCO. We perform time-

resolved photoelectron spectroscopy measurements of optimally doped $\text{Bi}_2\text{Sr}_2\text{CaCu}_2\text{O}_{8+\delta}$ (Bi-2212) and $\text{Bi}_2\text{Sr}_{2-x}\text{La}_x\text{CuO}_{6+\delta}$ (Bi-2201). The first part is partially based on my first contribution to Ref. [Pio15]. The quasiparticles relaxation rates exhibit a marked temperature and fluence dependence. Our observations display that a fast relaxation channel appears if the sample is above T_c or if it is strongly photoexcited. Moreover, the drop of quasiparticles dissipation is related to superconducting correlations but not to the pseudogap. In the second part of this chapter, I will also discuss the effects of photoexcitation on the band dispersion and broadening.

Chapter 4 explores the superconducting gap in the photoexcited state of $\text{Bi}_2\text{Sr}_2\text{CaCu}_2\text{O}_{8+\delta}$ (Bi-2212) by Tr-ARPES [Zha17]. The established results in the field of time-resolved measurements on cuprates are briefly reviewed. We will demonstrate that the photoexcitation and thermal fluctuations are comparable and that the superconducting gap collapses upon an intense photoexcitation. Due to the d-wave nature of the pairing, the critical fluence and recovery time of the superconducting gap is not isotropic but depends on the electronic wavevector.

Chapter 5 reports the electronic structure of the stripes 1/8 La-214 system with ARPES study. We present a well-defined ARPES kink in the quasi-particle dispersion and a nodal gap existing in the stripes state. The temperature evolution of the kink and nodal gap of LNSCO and LBCO could uncover the possible relationship between quasiparticle dressing, the stripe ordering, pseudo-gap and superconductivity.

Chapter 6 provides a summary of our work and the conclusion.

1.1 Historical background

1.1.1 Fundamentals of superconductivity

In 1911, H. K. Onnes discovered that the resistance of Mercury (Hg) abruptly dropped to zero upon lowering temperature [see figure 1.1(a)]. This phenomenon became known as superconductivity: is a quantum phenomena which manifests at macroscopic scale and it is characterized by zero electrical resistance. Subsequently it has been reported that many metals and alloys develop a superconducting phase.

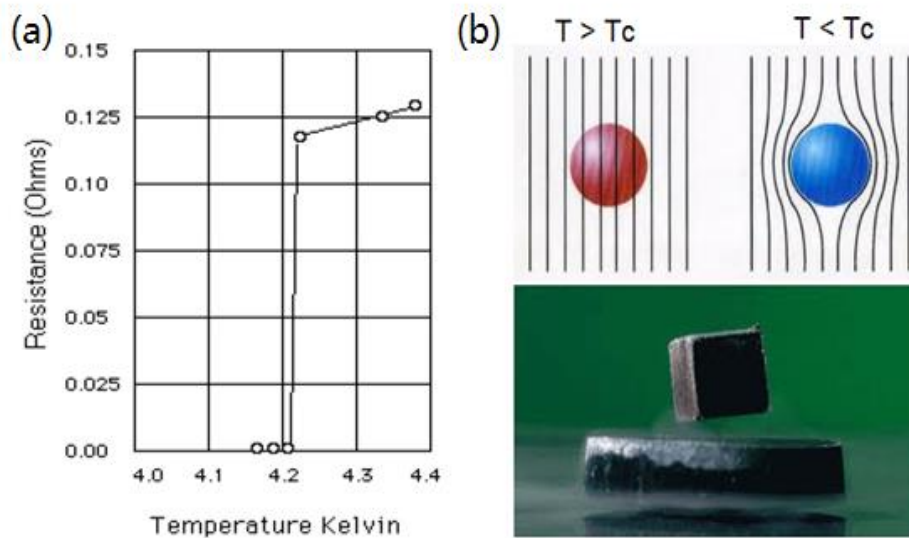


Figure 1.1 (a) Resistivity versus temperature plot for mercury. Superconducting phase transition takes place at ~ 4.2 K. (adapted from H. K. Onnes *et al*) (b) Meissner effect. Upper panel: Magnetic field lines are excluded from a superconductor when it is cooled below T_c ; lower panel: a magnet levitating above a high temperature superconductor cooled by liquid nitrogen

A very fundamental property associated with the superconductivity is the perfect diamagnetism discovered by W. Meissner and R. Ochsenfeld [Meissner1933] [see figure 1.1(b)]. Once a normal metal undergo SC transition the supercurrents expel an applied magnetic field from the bulk of the superconductor. The fascinating resistive and magnetic properties of superconductors immediately attracted a lot of attention from scientists.

The brothers Fritz and Heinz London developed the first phenomenological description of superconductor's electromagnetic properties [Lon35], accounting for the zero resistance property and Meissner effect. In 1950, the Russian theorists Lev Landau and Vitaly Ginzburg generalized the London theory to the case a superconducting order parameter that can vary in space and time. Ginzburg-Landau theory is especially useful in situations where the superconductivity is not homogeneous, such as superconducting-normal interfaces, Josephson tunneling junctions, superconductors in the presence of magnetic fields, etc. However the Ginzburg-Landau theory remains a phenomenological approach that does not explain the origin of the observed transition.

In 1957, the first microscopic theory of superconductivity, was formulated by Bardeen, Cooper and Schrieffer (BCS theory) [Bar57]. According to BCS theory, even a weak net attractive interaction between electrons in the Fermi sea can give rise to bound pairs known as Cooper pairs. It turned out that such effective attraction could be explained by second order interaction that is mediated by phonons. The electrons forming bound Cooper pairs condense into a coherent quantum state and give rise to superconductivity. The phase transition to the superconducting state is accompanied by an energy gain for the system and an energy gap Δ opens between the occupied and the unoccupied density of electronic states. This is the so-called superconducting gap, and its magnitude is equal to the pair binding energy. In phonon mediated BCS superconductors, the gap is isotropic in the k -space, showing an s-wave like symmetry and a magnitude that depends on the temperature, being zero at $T=T_c$, and maximum at $T=0$ K. The $\Delta(T)$ value is of the order of few meV and governed by the so-called "gap equation" in BCS superconductors. The microscopic BCS theory provides excellent explanations of various properties of superconductors such as nuclear relaxation, energy gap, elementary excitation etc., where energy gap is constant over space.

1.1.2 Discovery of High Critical Temperature

After the great success of BCS theory, the field was considered mostly solved, until the discovery of the high temperature superconductivity in copper oxide perovskite in 1986. In that year, Alex Muller and Georg Bednorz found that a brittle ceramic

compound $\text{La}_{2-x}\text{Ba}_x\text{CuO}_4$ became superconducting at the highest temperature known at that time, namely 30 K [Bed86]. This discovery triggered a flurry of activity in the field of superconductivity, as it was widely believed that the superconducting transition temperature T_c of conventional superconductors could never exceed 30K [Coh72]. In the following year, the liquid nitrogen temperature barrier (77K) was broken with the discovery of $\text{YBa}_2\text{Cu}_3\text{O}_{7-\delta}$, superconducting at 90 K [Wu87]. Soon after, a whole host of related material was found, as, e.g., $\text{Bi}_2\text{Sr}_2\text{Ca}_n\text{Cu}_{n+1}\text{O}_{6+2n+\delta}$, $\text{Tl}_2\text{Ba}_2\text{Ca}_n\text{Cu}_{n+1}\text{O}_{6+2n+\delta}$, and $\text{HgBa}_2\text{Ca}_n\text{Cu}_{n+1}\text{O}_{2n+4+\delta}$. All of these new high temperature superconductors are copper oxides known as cuprates in chemistry. The progress in newly discovered superconductors is show by the plot of T_c at atmospheric pressure as a function of year of discovery (see figure 1.2). Among these exotic superconductors, the cuprates and pnictides (Iron based superconductors, discovered in 2006 [Kam06]) are called High Temperature SuperConductors (HTSCs) because their T_c 's are much higher compared to conventional superconductors. High temperature superconductivity in the copper oxides is characterized by the same fundamental macroscopic phenomena – zero electrical resistance and the Meissner effect – as elemental BCS superconductivity. There are several macroscopic differences however. First, the copper oxide materials, or cuprates, are not metals over an appreciable portion of their doping temperature phase diagram. Second, the magnitude of the supercurrent that flows between superconducting crystals in direct contact with each other depends on the relative orientation of their crystal structures. Certain orientations will allow no supercurrent at all to flow between them while others permit the maximum amount. Finally, the macroscopic critical values for temperature and magnetic field can be up to two or three times greater in the cuprates than in any know classical superconductors at ambient pressure. This last fact is the origin of great practical as well as academic interest in the high T_c cuprates. Within this thesis work, however, the term high temperature superconductors /superconductivity will be referred to cuprates.

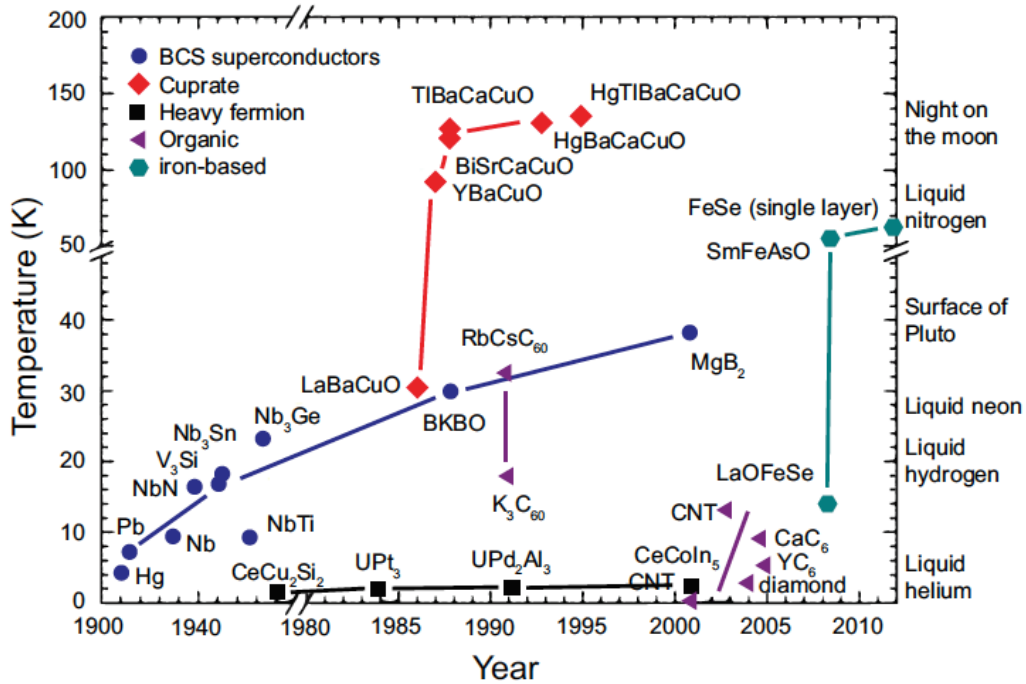


Figure 1.2 A roadmap for the discovery of higher T_c (T_c at atmospheric pressure) superconductor materials ([adapted from Smallwood *et al.*]).

The high transition temperature of cuprates cannot be explained in the frame of the electron-phonon mediated BCS theory. Until recently, many alternative theories have been proposed. However, there has been no consensus on which one to apply.

1.2 Cuprate HTSCs

There exist several families of cuprate HTSCs, which differ by their chemical composition. Within each family, the compounds are characterized by the number of CuO layers per unit cell, which are the common building block of all cuprate HTSCs. These superconductors share common features:

(1) They have layered perovskite like crystal structure containing one or more CuO_2 planes. A selection of the most intensely studied compounds includes e.g. $\text{La}_{2-x}\text{Sr}_x\text{CuO}_4$ (LSCO), $\text{YBa}_2\text{Cu}_3\text{O}_{7-\delta}$ (YBCO) and $\text{Bi}_2\text{Sr}_2\text{CaCu}_2\text{O}_{8+\delta}$ (BSCCO). As shown in figure 1.3, CuO_2 layers in HTSCs are separated from each other by the so-called charge reservoirs, the insulating block. Typically in $\text{Bi}_2\text{Sr}_2\text{CaCu}_2\text{O}_{8+\delta}$ (BSCCO, or Bi-2212) system (figure 1.3c), the bonding between two Bi-O layers is caused by

Vander-Waals interaction, which is very weak, and therefore leads to natural cleavage planes. In figure 1.3 (c), we can see that the tetragonal unit cell of Bi-2212 has lattice constant $a=b=5.4 \text{ \AA}$, and $c=30.7 \text{ \AA}$.

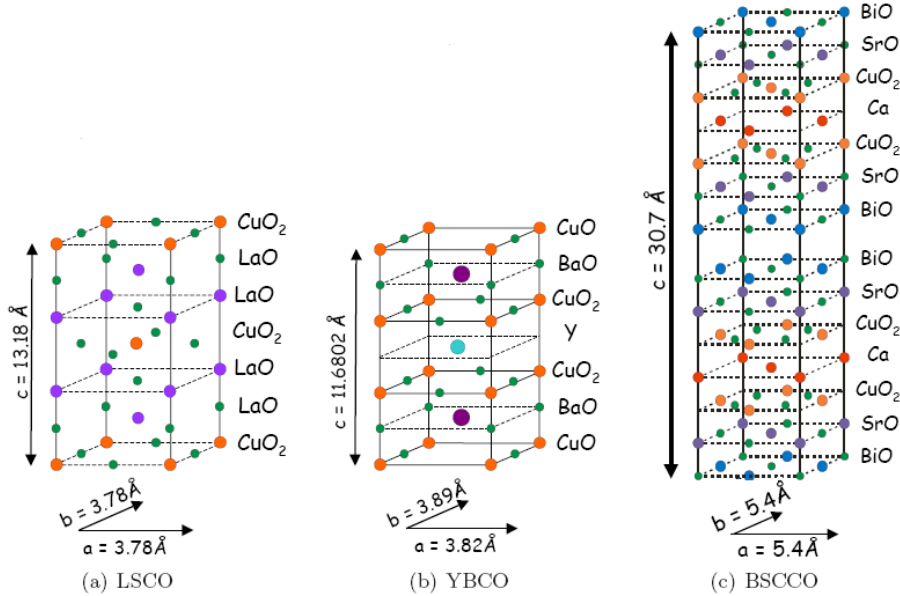


Figure 1.3 Crystal structures of three high temperature superconductor families: $\text{La}_{2-x}\text{Sr}_x\text{CuO}_4$ (LSCO), (b) $\text{YBa}_2\text{Cu}_3\text{O}_{7-\delta}$ (YBCO), and (c) $\text{Bi}_2\text{Sr}_2\text{CaCu}_2\text{O}_{8+\delta}$ (BSCCO)

(2) All the superconducting cuprates have similar phase diagram. The parent compounds of the cuprates are layered, quasi-two-dimensional (2D) ceramic copper oxides, that are antiferromagnetic (AF) charge transfer insulators due to the very strong electron-electron (el-el) correlations (i.e. large on-site Coulomb repulsion U) found in these materials [Dam03]. A prototypical phase diagram of the cuprates for electron and hole doping is depicted in figure 1.4. For both electron and hole doping, the insulating AF phase is rapidly suppressed and a pseudogap phase can be observed on the hole-doped side. At higher doping levels, superconductivity emerges in the so-called "superconducting dome", with the highest T_c at a hole or electron concentration of $x \sim 0.15$ electrons or holes/Cu.

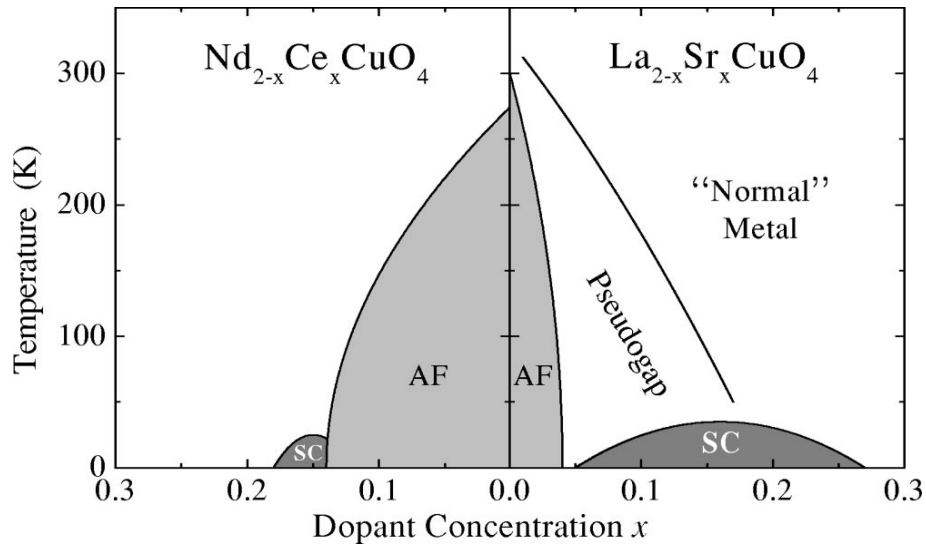


Figure 1.4 Schematic phase diagram of the cuprate HTSCs. The undoped cuprates are antiferromagnetic (AF) Mott-insulators. After suppression of the AF phase by either hole (right) or electron (left) doping, superconductivity emerges in the "superconducting dome" ([adapted from Dam03]).

(3) The generic features of cuprates electronic structure are similar. The HTSCs exhibit a quasi-2D electronic structure with weak out-of plane band dispersion. In a parent compound like BSCCO, Cu is divalent with $3d^9$ electronic configuration, with its degeneracy lifted by the crystal field, all the states are fully occupied except the topmost $3dx^2-y^2$, which is half filled (see figure 1.5).

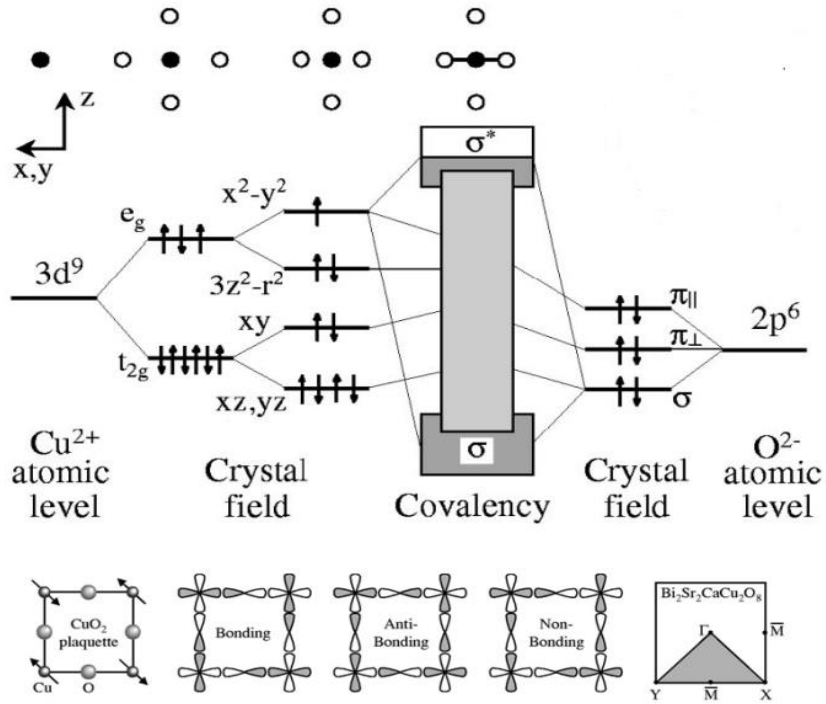


Figure 1.5 Upper panel: a schematic picture of the origin of the Cu-O bands in the cuprates. Lower panel: phase at (π, π) of Cu $d_{x^2-y^2}$ and O $2p_x$ and $2p_y$ orbitals for bonding, antibonding, and nonbonding hybridized wave functions for the bare CuO_2 plane, and 2D projected Brillouin zones with conventional notations for BSCCO ([adapted from Dam03]).

As shown in figure 1.5 (a), the band structure of the three orbitals (Cu $d_{x^2-y^2}$ and O $2p_x$ and $2p_y$) at half filling displays an antibonding band at the Fermi level, and the nonbonding and bonding bands at higher binding energy. According to band theory, this system with odd number of electrons per unit cell should be a paramagnetic metal, with a partially filled d band in metal oxides. In reality undoped cuprates are very good insulator and are fundamentally different from conventional band insulators.

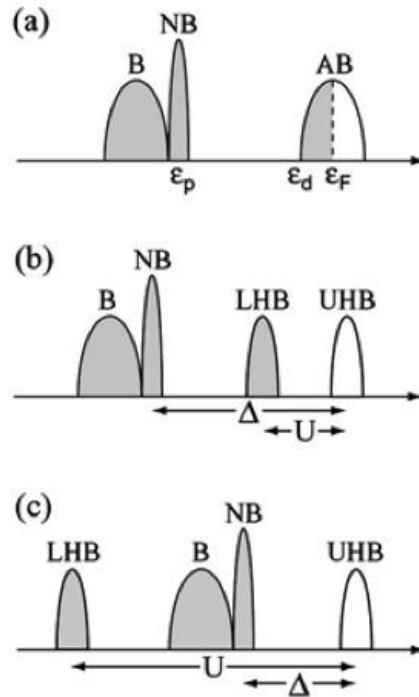


Figure 1.6 Density of states for (a) metallic system in the absence of electronic correlations, (b) a Mott insulator for $\Delta > U > W$ (c) a charge-transfer insulator, $U > \Delta > W$ ([adapted from Dam03]).

The reason why single electron band structure theory fails is the presence of strong electronic correlations. In considering the motion of one electron band structure theory treats the rest of electrons as a mean static potential. However, in highly correlated systems, the single particle excitations depend dramatically on the many-body electronic state. When all sites are half filled and the electron-electron interaction (Columb interaction) is much larger than the hopping term (the overlap of two neighbor electrons wave function), two electrons cannot occupy the same site, so they become localized in space.

In the strong correlation limit, the large Columb repulsion U is much larger than the bandwidth W . When this is the case an electronic gap develops between the fully occupied site (upper Hubbard band) and half occupied site (lower Hubbard band). As shown in figure 1.6, the material is a rather good insulator (Mott-Hubbard insulator) [Mott49 Hub64] with an electronic gap of a few eV between the two Hubbard bands.

In the case of the copper oxides, as the on-site electron-electron repulsion U for the

Cu $3d$ electrons is larger than the bandwidth W . The antibonding band splits into upper and lower Hubbard bands and charge fluctuations are suppressed [see figure 1.6 (b)]. However, Cu-O charge-transfer energy Δ in the cuprates is smaller than the on-site Coulomb repulsion U [see figure 1.6 (c)]. This energy defines the electronic gap and characterizes the cuprates more precisely as charge-transfer insulators [Zaa85].

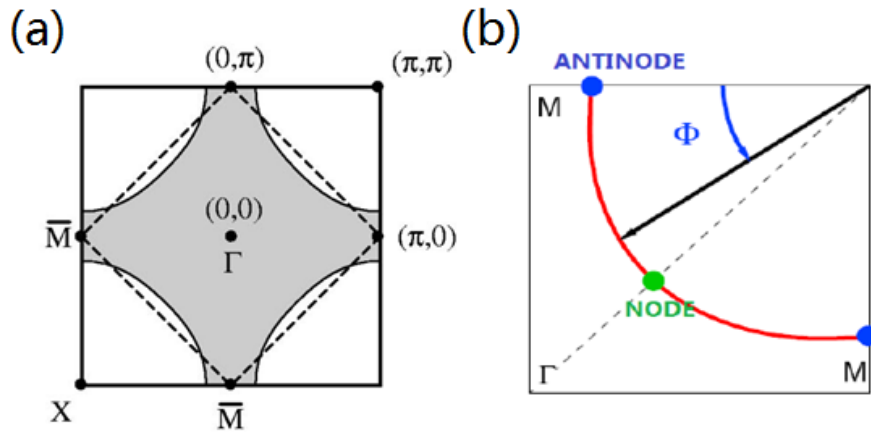


Figure 1.7 (a) Calculated Fermi surface for the CuO_2 plane. Diamond, Fermi surface at half filling calculated with only the nearest-neighbor hopping gray, Fermi surface obtained including also the next nearest- neighbor hopping [Dic93]. (b) Nodes, which are indicated by green dots, are the Fermi momenta k_F , where there is no energy gap. Antinodes, which are indicated by blue dots, are the Fermi momenta having maximum energy gap. The angle ϕ is called Fermi surface angle.

Upon doping the CuO_2 layers with holes, the antiferromagnetic Mott phase is lost, while an exotic phase without well-defined Fermi surface takes over. In the intermediate doping range between 0.8 holes and 0.26 holes the material is a bad metal at room temperature but becomes superconductors at low temperature. Finally, in the high doping regime the normal phase resembles nearly the one of a Fermi liquid and holds a well-defined Fermi surface [Loe96][Din96].

The idealized Fermi surface of a half filled square lattice is shown in figure 1.7 (a). For the calculation, only nearest-neighbor hopping (Cu-O, t_{pd}) was considered, a diamond like Fermi surface is obtained. A distortion of this surface takes place with the more realistic inclusion of next nearest- neighbor hopping (O-O, t_{pp}), which results in the Fermi surface given by the gray area in figure 1.7 (a) [Dic93]. These

results seem to correspond well to the photoemission spectrum. As the cuprate high temperature superconductors have a quasi-2D electronic structure with weak dispersion along z-axis, in the discussion of the ARPES data we shall refer to the 2D projected zones as the one presented in figure 1.7 (a).

1.3 Superconductivity of Cuprates

1.3.1 Unconventional pairing symmetry

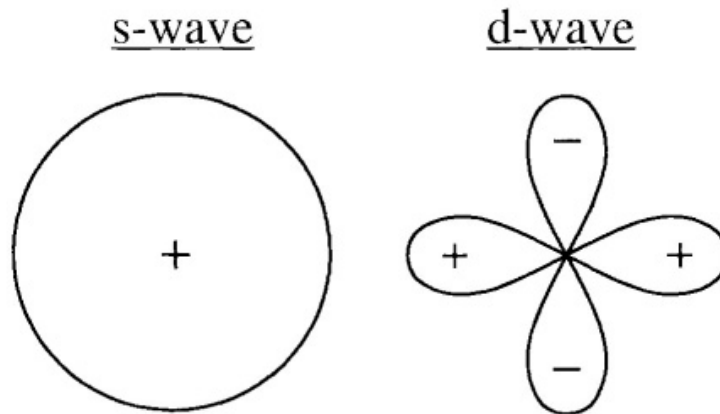


Figure 1.8 left Panel shows the s-wave gap symmetry for the conventional superconductors. The circle represents a constant gap as a function of k . The right panel shows d-wave superconducting order parameter of the cuprates, with the different phases marked by “+” and “-”.

The proximity of antiferromagnetic phase and the presence of strong antiferromagnetic fluctuations have strong impact on the electronic properties of the strange "pseudogap" phase. Most authors now agree that such properties also affect the superconducting instability. Indeed the superconducting order parameter of cuprates has a different symmetry than the one of the standard BCS systems (see figure 1.8). In conventional superconductors, the order parameter is isotropic and the energy gap has no nodes.

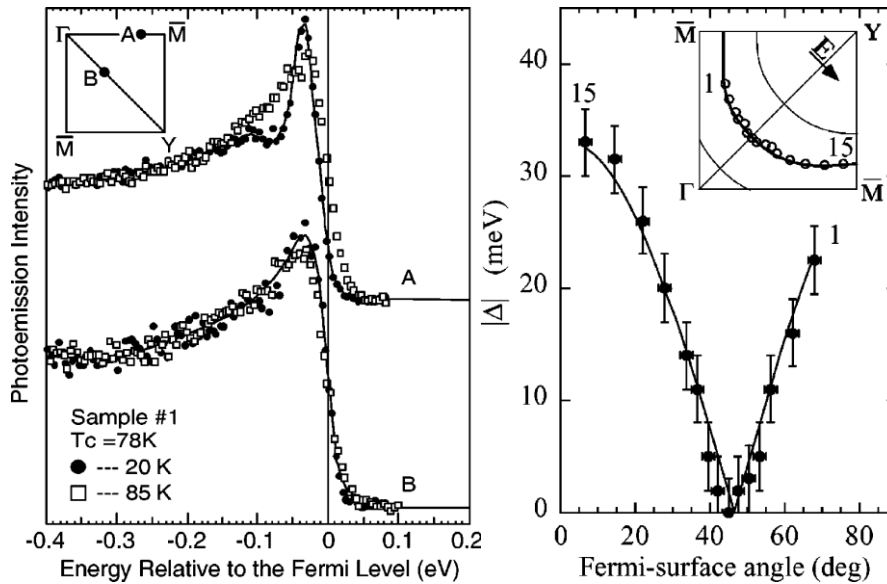


Figure 1.9 Early ARPES measurements of Superconducting gap versus Fermi surface angle (ϕ) in Bi-2212, with fits to a d-wave form. (Left panel From Shen *et al.*, 1993, right panel From Ding, Norman, *et al.*, 1996)

The situation in cuprates is more complex and interesting. All phase-sensitive techniques [Tsu00a Tsu00b and reference therein] show that hole-doped and electron-doped cuprates have an anisotropic superconducting ground state with dominant $d_{x^2-y^2}$ symmetry. Accordingly, most of the ARPES measurements observe a four-fold symmetry of energy gap. Only in special cases, some authors discussed the possible small s-wave contributions as well as more exotic ground states. In a pure $d_{x^2-y^2}$ symmetry the gap is given by $\Delta_k = \Delta_0(\cos(k_x) - \cos(k_y))$, where $k = (k_x, k_y)$ is the wave vector and Δ_0 is the zero-temperature value of the d -wave gap amplitude [She93]. The gap is maximal for momenta parallel to the Cu-O-Cu bond (anti-nodal direction) and zero for momenta at angles of 45° to this bond (nodal direction). Figure 1.9 shows the angle-resolved photoemission spectroscopy (ARPES) data on one Bi-2212 sample, and its energy gap anisotropy following a d-wave pattern [She93][Din96]. For samples in the optimal and overdoping region, their gap symmetry is d-wave like, and Δ_0 becomes smaller with the increase of doping.

1.3.2 Pseudogap

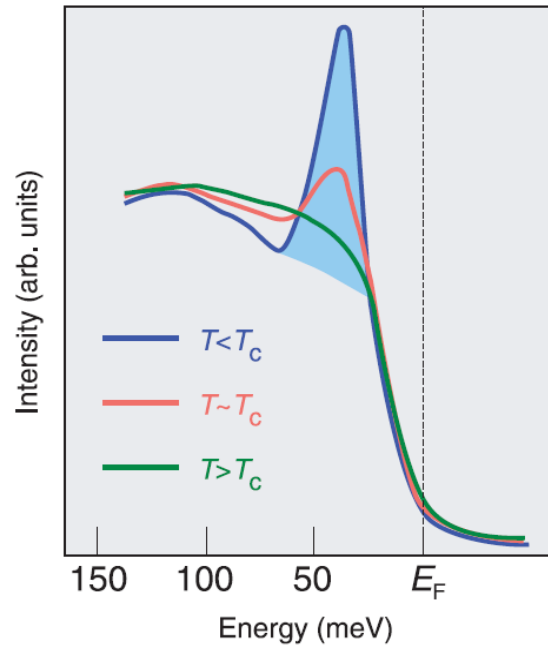


Figure 1.10 Representation of ARPES spectra for underdoped high- T_c superconductor at momentum near the antinodal point of the Brillouin zone. [Adapted from [Loe97]]

As we previously stated, one of the main problems in cuprates is that superconductivity does not emerge from a well-defined Fermi liquid state. The normal phase of these compounds is indeed very exotic.

In the underdoped side of the cuprates' phase diagram, it was observed by angle-resolved photoemission spectroscopy [Tim99, Loe96, dIN96, Ren98] measurements that a soft gap called “pseudogap”, opens up in electronic density of states at a temperature T^* well above T_c (as shown in figure 1.10). The origin of this gap in electronic excitation spectra without zero resistance is a major unresolved issue in cuprate physics. As for the superconducting gap also the pseudogap is absent along the nodal direction and maximal at the antinodal region. However the pseudogap does not have the momentum dependence predicted by a d-wave order parameter. Instead, it leaves a non-gapped section of the Fermi surface near to node, also known as Fermi arc [Nor98]. The magnitude of the pseudogap is large in underdoped samples and progressively shrinks with increasing hole doping. In the overdoped case, a complete and well-defined Fermi surface can be observed in the normal phase [Loe96][Din96].

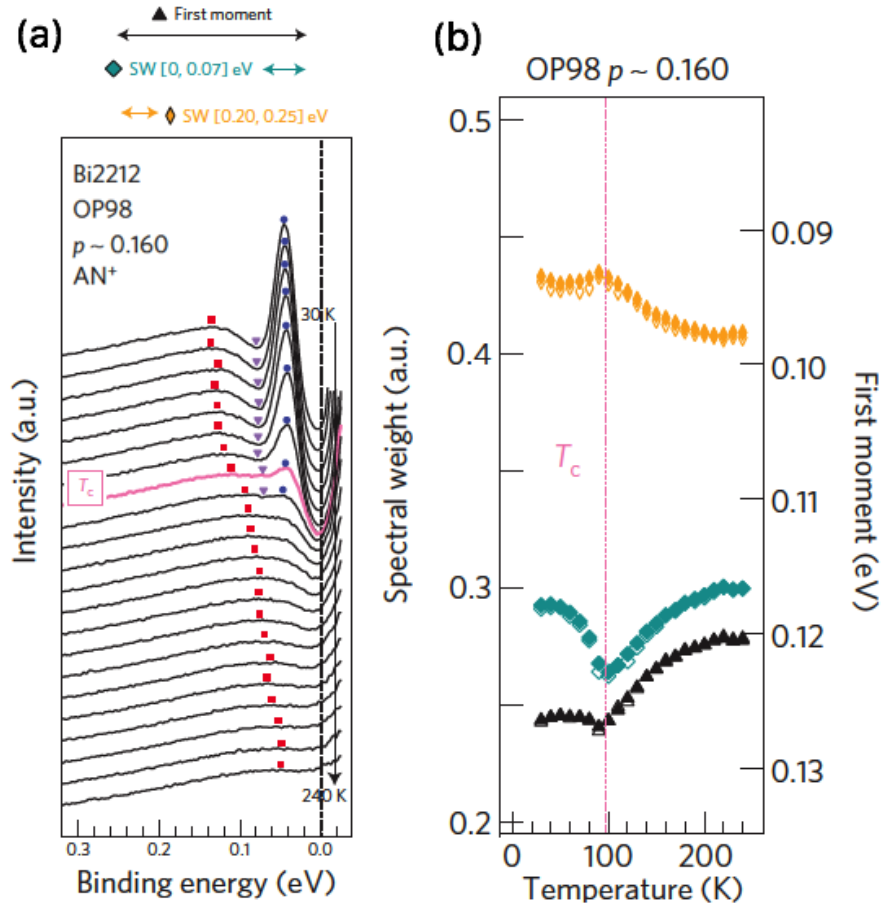


Figure 1.11 Temperature dependence of the antinodal electronic states in optimally doped Bi-2212. (a) FD-divided spectra at antinodal. (b) Antinodal spectral weights in the ranges [0, 0.07] and [0.20, 0.25] eV (left axis) and the first moment in the range [0, 0.25] eV (right axis) for optimal doped Bi-2212. From Ref. [Nmat 4166]

Many authors suggested that the pseudogap is due to the presence of short antiferromagnetic fluctuations. In this scenario is the proximity of a Mott insulating phase that causes the presence of Fermi arcs near to the nodes and that destroy quasiparticles in the antinodal direction. Other authors suggest that such pseudogap arises from a competing order, whose origin is still to be identified. In particular Hashimoto *et al.* reported a non-monotonic evolution of the low energy spectral weight in Bi-2212 (see figure 1.11). Figure 1.11 (b) shows the normalized spectral weights in the ranges [0, 0.07] and [0.20, 0.25] eV, which we denote as the low- and high-energy spectral weight. Below T_c , the first moment and the low- and high-energy spectral weights show the opposite trends. They interpreted this result as compelling evidence for an exotic phase that competes with superconductivity.

1.3.3 Fluctuations of the superconducting order parameter

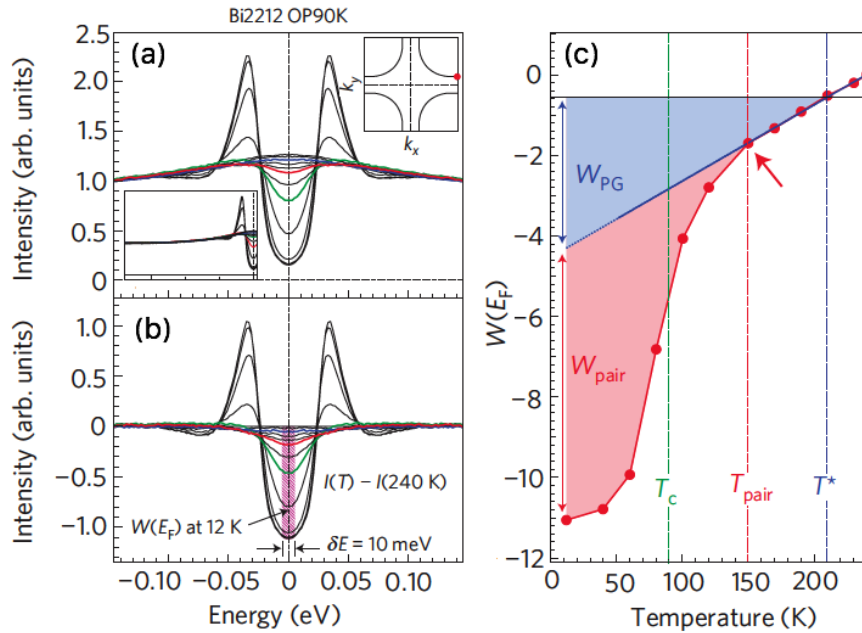


Figure 1.12 Temperature dependence of the spectral weight at the Fermi energy at the antinode in optimally doped Bi-2212 ($T_c=90\text{ K}$). (a) Symmetrized EDCs for various temperatures. (b) Difference spectra: the spectrum measured at the highest temperature is subtracted from each of spectra in (a). (c) Spectral weight close to the Fermi level ($W(E_F)$, hatched area) is estimated by integrating the spectral intensity in b within an energy window of the experimental energy resolution (10 meV). [Adapted from [Kon11]]

Competition of the pseudogap with superconductivity does not preclude the formation of Cooper pairs above T_c . This is possible because of short coherence length that Cooper pairs have in high temperature superconductors. Kondo *et al.* found a spectroscopic evidence of pair formation and were able to establish the value of the pairing temperature using a quantitative approach [Kon11]. Figure 1.12 shows the temperature evolution of the spectral line shape measured at the antinodal Fermi momentum in optimally doped Bi-2212 ($T_c=90\text{ K}$). Symmetrized energy distribution curves (EDCs) show the opening of the pseudogap on cooling below T^* ($\sim 210\text{ K}$). The spectral changes with temperature have been highlighted by subtracting the spectrum at the highest temperature from all the spectra measured, as shown in figure 1.12 (b). The temperature dependence of the loss of spectral weight close to the Fermi level $W(E_F)$ is plotted in figure 1.12 (c). The blue line is an extrapolation of the linear

behavior observed at high temperatures and has been interpreted as the signature of the pseudogap. By decreasing the temperature, there is a deviation from the linear form at T_{onset} due to the formation of Cooper pairs without long-range order.

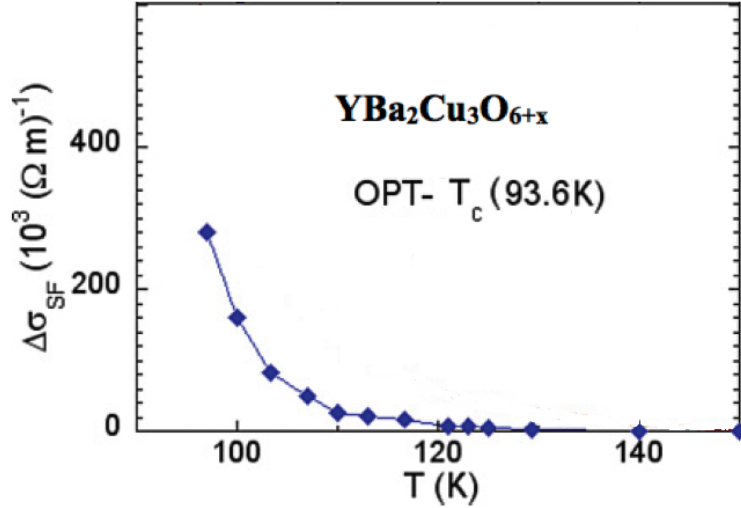


Figure 1.13 The variation of superconducting fluctuation conductivity $\Delta\sigma_{SF}$ (T) deduced with the magnetoresistance (MR) measurements. From Ref. [Rul11]

The presence of strong superconducting fluctuations above T_c has been highlighted by many other experiments. Transport measurements have been performed to detect the paraconductivity in optimally doped high- T_c cuprates [Rul11]. The authors employed pulsed magnetic fields of very high intensity in order to suppress the superconductivity (SCF) in a series of $YBa_2Cu_3O_{6+x}$ samples. By these means they have been able to isolate the contribution $\Delta\sigma_{SF}$ of the superconducting fluctuations to the dc-conductivity. Figure 1.13 shows that $\Delta\sigma_{SF}$ extend above $T_c=93.6$ K and are still detectable until 120 K. It has been now established that such region superconducting fluctuation (SCF) disappear at an onset temperature $T_{\text{onset}} \sim 1.3T_c$ that is different from the pseudogap temperature T^* .

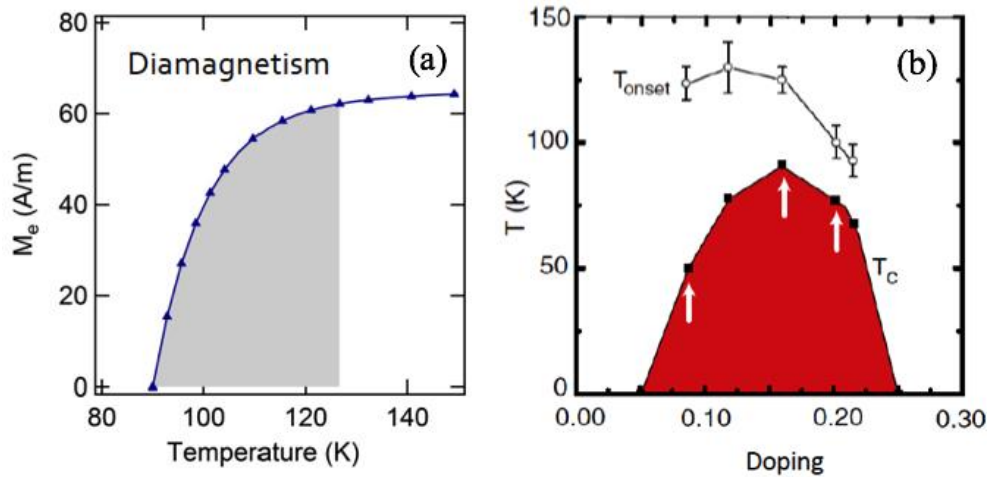


Figure 1.14 (a) The temperature dependence of diamagnetism signals M_{eff} in single-crystal optimal doped Bi-2212 at $B = 14$ T. (b) Onset temperature (T_{onset}) for the diamagnetic signal is plotted vs x (hole content) together with T_c . Arrows indicate the 3 samples studied by torque magnetometry. From Ref. [Wan05]

The formation of a fluctuating condensate affects also the diamagnetic response of the material. Wang *et al.* reported a diamagnetic signal M in optimal doped Bi-2212 samples ($T_c = 87.5$ K) above T_c [see Figure 1.14(a)]. As shown in figure 1.14 (b), the onset temperature of torque diamagnetic signal follows nearly the evolution of the superconducting dome over the doping range of $0.08 < x < 0.25$.

The non-equilibrium spectroscopies offer also a new tool to investigate the role of the fluctuations in the superconducting transition. THz spectroscopy directly probes the superfluid response and is thus a useful tool for measuring the temporal fluctuations of the superconducting order parameter.

Broadband time-domain THz spectroscopy in Bi-2212 [Cor99] and $\text{La}_{2-x}\text{Sr}_x\text{CuO}_4$ [Bil11] unveiled the persistence of superconducting correlations up to 16 K above T_c . The further development of the techniques also led to the development of more elaborate techniques in optical pump-probe experiments aimed at investigating the relaxation dynamics with high temporal resolution. Indeed, using an all-optical three-pulse technique on Bi-2212, the fluctuation dynamics of the superconducting pairing amplitude was separated from pseudogap signal above the critical transition temperature. A more detailed analysis of the critical behavior near T_c has been recently obtained on thin Bi-2212 films with optical pump-THz probe measurements,

directly monitoring the dynamics of the mid-infrared conductivity [Per15]. As shown by figure 1.15, the data allowed to discriminate the temperature regimes where superconductivity is either coherent, fluctuating or vanishingly small.

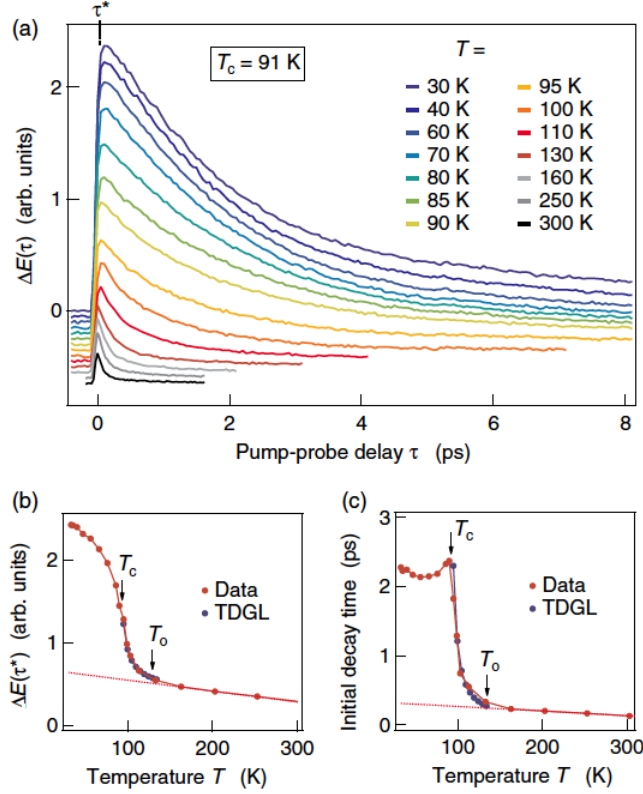


Figure 1.15 Nonequilibrium data of optimally doped BSCCO ($T_c = 91$ K). (a) Pump-induced changes $\Delta E(\tau)$ in the transmitted MIR electric field as a function of pump-probe delay τ . $\Delta E(\tau)$ scales with the pump induced change $\text{Re}\Delta\sigma(\nu, T)$ in the instantaneous BSCCO conductivity averaged from 15 to 25 THz. (b) Signal magnitude ΔE and (c) relaxation time directly after sample excitation ($\tau = \tau^* = 50$ fs) as a function of temperature (red circles). Blue squares result from a model based on the Time dependent Ginzburg Landau model. The transition temperature ($T_c = 91$ K) and the onset of superconducting fluctuations (at $T_0 = 130$ K) are indicated by arrows. From Ref. [Per15]

Finally, also our recent time-resolved ARPES measurements [Piovera15] suggested that the pump-induced modification of the nodal QP population is affected by the onset of superconducting pairing fluctuations at $T_{\text{onset}} > T_c$. Overall, these results strongly support the scenario in which the pairing amplitude of underdoped cuprates extends a few tens of degrees above T_c .

1.3.4 Competing or intertwined electronic ordered phases.

In the case of cuprates, a well defined ground state is antiferromagnetism [Ore00, Lee06, Arm10] clearly in competition with superconductivity, although other states came to light later as spin glass and magnetic fluctuations, charge modulations, either in the form of "stripes" [Ore00, Kiv03], or of Charge-Density-Waves (CDW) [Wis08] and, more recently, ordered loop-currents [Li_08,Li_10]. Covering all these possible cases would go far beyond the limit of this work, so we limit our discussion of other (competing) orders to the underdoped cuprates, particularly of "214" type, where charge modulation have been clearly identified and investigated. In the following we briefly discuss some evidence of phase ordering that competes with superconductivity. These phases generally appear around specific doping levels. Therefore it is unlikely that they can explain the broad extension of the pseudogap in the phase diagram. However the connection and the observed competing orders to the electronic properties is currently under strong debate and we review here few major aspects.

In general, a competition between the superconductivity and the crystallization of the electrons in forms of some kind of charge modulation is a very natural way to account for the diminishing superfluid density in the pseudogap regime. Indeed, the physics of the CDW instability is also relevant for copper oxides superconductors. The universal tendency to develop short-ranged incommensurate CDWs that break the translational symmetry has been recently reported in both hole- and electron-doped copper oxides [Com14, Ghi12, Cha12, Sil15]. These findings opened new intriguing questions about the origin of the CDW instability and its competition to the superconducting phase. Evidence for charge and spin stripes, was established as early as 1992 near $p = 0.125$ hole doping in LBCO, LSCO, and related cuprate compounds within the "lanthanum-214" crystal structure family [Tra95, Fuj02, Tra04, Kiv03]. The stripe order, characterized by incommensurate antiferromagnetic order and charge segregation, was initially found in underdoped version of LSCO, where a low-temperature tetragonal lattice deformation apparently acts as a pinning potential for the stripes [Tra95].

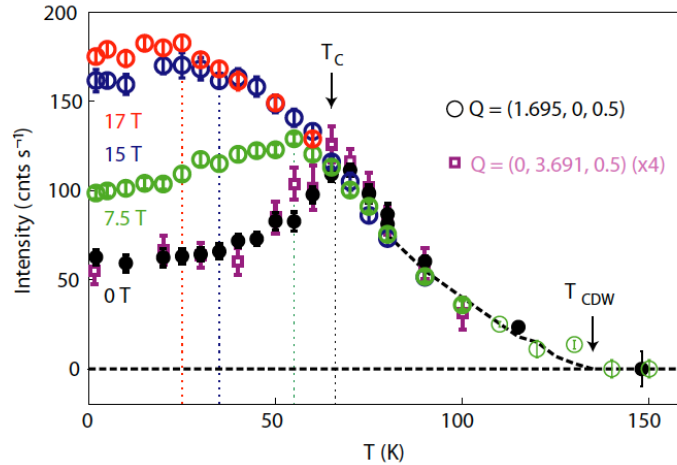


Figure 1.16 Charge density wave Bragg peak in YBCO as measured by x-ray diffraction. The cusp at T_c in the black data points, which indicates competition between the CDW and superconductivity, can be eliminated by the application of a large magnetic field as shown by the green, red and blue data points. From Ref. [Cha12]

More recently experiments in this field of research have been performed by means of non-resonant X-ray diffraction. As shown in figure 1.16, the incommensurate CDW Bragg peaks signal builds up smoothly upon cooling below a characteristic charge ordering temperature (T_{cdw}) typically less than T^* , to attain a maximum at the superconducting T_c , then drops noticeably below T_c , indicating competition between the charge order and superconductivity [Ghi12][Cha12][Bla14].

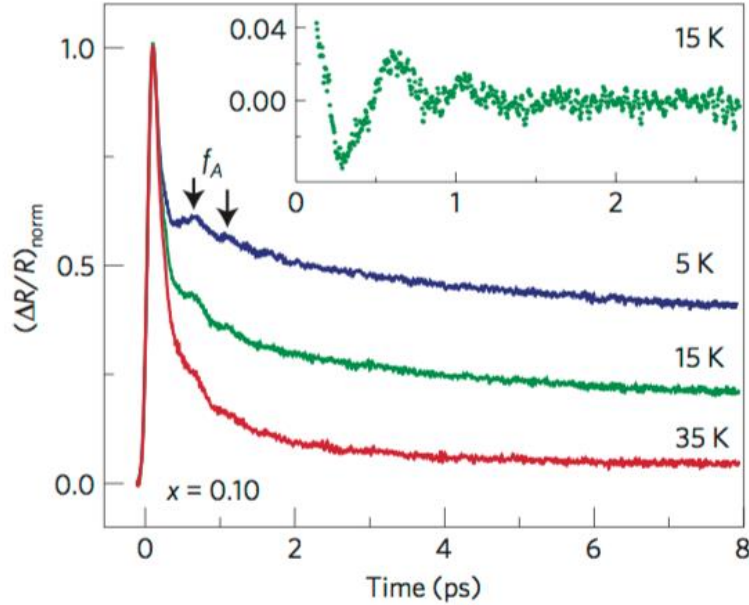


Figure 1.17 Relative reflectivity variation measured in a single-colour Pump-probe experiment on $\text{La}_{1.9}\text{Sr}_{0.1}\text{CuO}_4$ at different temperatures. From Ref. [Tor13]

The possibility of impulsively removing the CDW order and of achieving its control by optical means would open interesting, though challenging, ways to increase the critical temperature of copper oxides. Recently, the observation of a coherent oscillation at 2 THz in a single-colour Pump-probe experiment has been reported in underdoped $\text{La}_{1.9}\text{Sr}_{0.1}\text{CuO}_4$ films ($T_c=26$ K) up to a temperature of ~ 100 K (see figure 1.17) [Tor13]. This oscillating signal has been attributed to a highly damped collective mode of the fluctuating CDW. The observation that the CDW mode vanishes in the optimally doped $\text{La}_{1.84}\text{Sr}_{0.16}\text{CuO}_4$ compound ($T_c=38.5$ K), supports the scenario of a competing interaction between the CDW order and superconductivity.

1.3.5 The Electron-Boson coupling in HTSC

Coupling between the electrons and phonons drives the formation of the electron pairs responsible for conventional superconductivity. The electron-phonon interaction is thus an essential topic to be investigated in the framework of the BCS case. However, no consensus has been reached yet on the nature of the (bosonic) glue in the High- T_c : a strong debate is on whether the pairing is due to phonons, spin fluctuations, or both (bosons or phononic), or it is of pure electronic origin. It follows that phonons may as

well have not-trivial role on the development of a superconducting phase. By determining the electron-phonon coupling strength in High-Tc materials, it is possible to point out whether the material is in the weak or strong coupling regime, and possibly whether phonons contribute (cooperatively) to the pairing. Many techniques, such as ARPES, inelastic neutron scattering, tunneling spectroscopy, optical conductivity, have been exploited to measure the electron-phonon coupling constant in superconductors. Recently, a large body of experimental result from angle-resolved photoemission, suggest that the average electron-phonon coupling in cuprates is not strong but that such interaction is distinct from a conventional one. In particular, the momentum dependence of the coupling strength and the interplay between electron-phonon interaction and electron-electron interaction are very important.

The first ARPES experimental investigation of electron phonon coupling is done by Lanzara *at al.* [Lan01]. A coupling of an electron to a phonon branch result in an abrupt change the quasiparticle velocity and scattering rate near the phonon energy. In particular, they identify the kink with an oxygen related optical phonon. Figure 1.18 shows the dispersion along the nodal direction in several cuprate families. The kink is a universal feature and exists in both the normal and superconducting state. Given that the kink occurs at 60-70meV, the source of the renormalization is attributed to the 70 meV in-plane oxygen half breathing mode seen by neutron scattering. This interpretation explains the data fairly well in the normal state, but is inconsistent with established electron-phonon coupling theory in the superconducting state, where the energy at which a mode couples to the electrons should change with the opening of the superconducting gap to the boson frequency plus Δ_0 . This issue is puzzling but not conclusive. Indeed, even in MgB₂, the 65 meV Kink that originates from the coupling of electrons to the E_{2g} does not significantly change across T_c [Mou15].

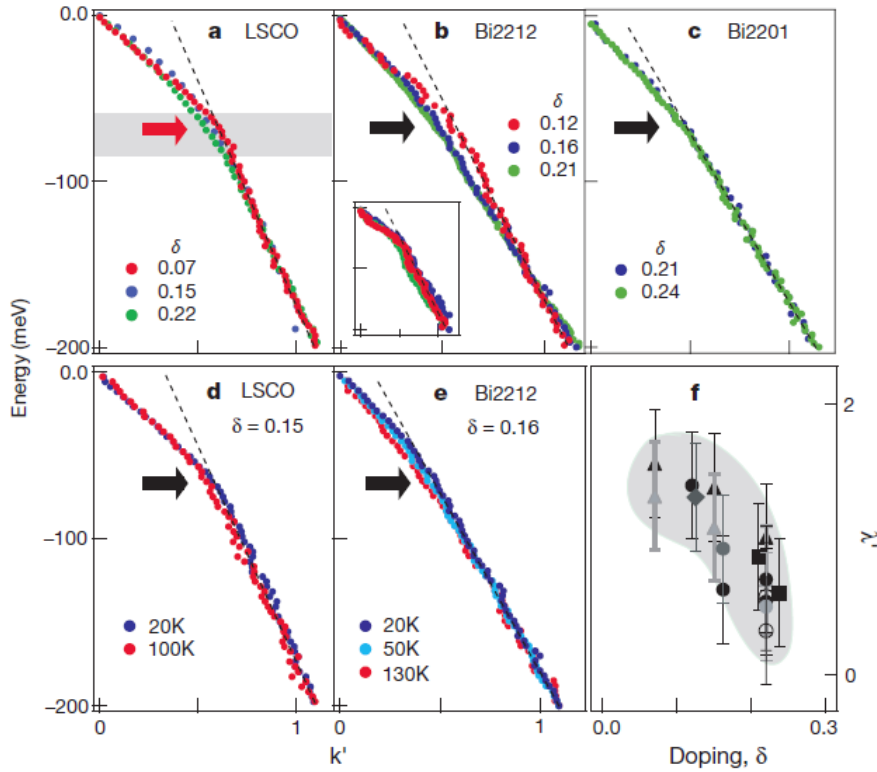


Figure 1.18 Evidence for widespread electron-phonon coupling in cuprate superconductors. (a)–(e) Nodal electronic dispersions in LSCO, Bi-2212, and Bi-2201. All dispersions exhibit a prominent electron-boson-coupling kink feature at 70 meV. (f) Doping-dependent coupling constant, defined by comparing the low- and high binding energy slopes of the data displayed in (a)–(e). From Ref. [Lan01]

Meanwhile, a wealth of non-equilibrium spectroscopies, such as time-resolved optics, photoemission and electron or X-ray diffraction have been applied to investigate the electron-phonon coupling problem from a different perspective. Addressing this issue is of particular relevance, since it may be intimately connected to the pairing in unconventional superconductors. The non-equilibrium approach offers a direct way of extracting the electron-phonon coupling. Indeed, the timescale of the return-to-equilibrium of an excited system of electrons and phonons is related to the electron-phonon coupling strength.

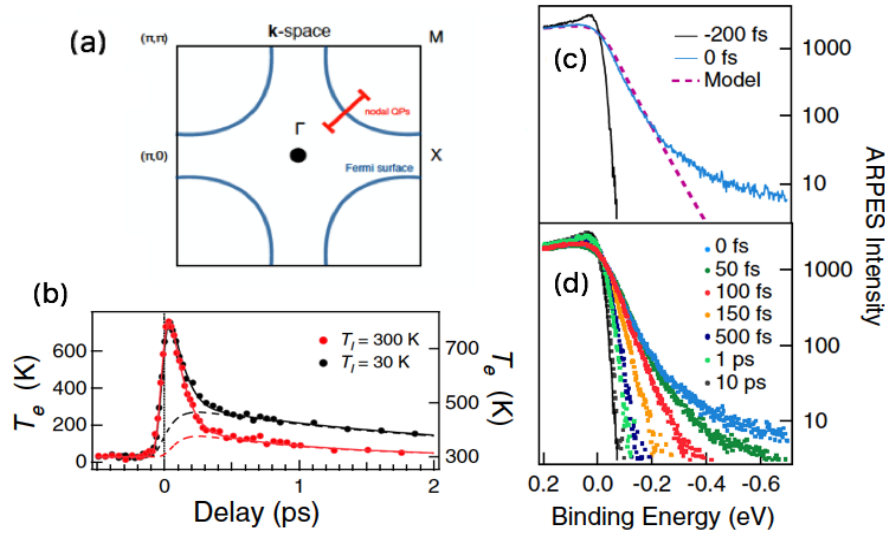


Figure 1.19 Dynamics of the time-resolved ARPES spectra in optimally-doped Bi-2212 ($T_c=91$ K). a) Prototypical two-dimensional Brillouin zone of copper oxides. The time-resolved ARPES experiment probes the transient occupation along a k-space cut perpendicular to the Fermi surface in the nodal region. b) Dynamics of the effective electronic temperature at different equilibrium temperatures before the pump excitation. c) Transient quasiparticle occupation at the maximum overlap between the pump and probe pulses (blue line, $t=0$) contrasted to the equilibrium Fermi-Dirac QP distribution (black line, $t < 0$). The dashed red line is the fit to the data of a hot Fermi-Dirac distribution at the effective electronic temperature T_e . d) Picosecond evolution of the non-equilibrium nodal QP distribution. Taken from [Per07].

Profound insights into the charge relaxation dynamics in cuprates are given by time-resolved ARPES experiments (see figure 1.19), in which the transient electronic occupation is probed during the relaxation process triggered by a 1.5 eV ultrafast pump pulse. The QP distribution quickly evolves from a non-thermal distribution to a hot-Fermi-Dirac function with effective temperature $T_e > T_0$. In figure 1.19 (c) the cooling dynamics of the QP is reported by fitting the hot Fermi-Dirac at the different pump-probe delays. Similarly to the case of MgB_2 [Dem03], the relaxation exhibits two different dynamics. The first (~ 100 fs) is related to the fast and effective energy exchange with the strongly-coupled lattice modes, while the second ($\sim 1-2$ ps) accounts for the thermalization with the entire phonon spectrum. A simulation of the measured curves by the 3-temperature model provides a coupling to strongly coupled optical phonons smaller than 0.3.

Recent TR-ARPES experiments on Bi-2212 and Pb-Bi2201 also evidenced a transient decrease of the electron self-energy upon photoexcitation, [Zha14]. The tight relation between the dynamics of the electron-boson coupling and that of the superconducting gap is also supported by the fact that the electron boson coupling is unresponsive to the ultrafast excitation above the superconducting critical temperature [Zha14].

Chapter 2

Experimental Techniques

2.1 Basic Principles

Photoemission spectroscopy (PES) is a photon-in electron-out type of experiment. It is based on a very simple physical phenomenon of solids: the photoelectric effect. Light with enough photon energy impinging on the surface of a material can liberate electrons from it. These free electrons are collected by an analyzer which then determines the kinetic energy E_{kin} of the electrons. Knowing, the binding energy E_B of the electron is determined by the following equation:

$$E_{kin} = h\nu - \Phi - |E_B|$$

where $h\nu$ is the photon energy and Φ is the work function of the sample. The work function is the amount of energy needed for the electrons at the Fermi level to overcome the attractive potential of the material to escape in the vacuum. In practical PES experiments, since both the sample and the electron energy analyzer are grounded, the measured kinetic energy E_{kin} of the emitted electron is referred to E_F . The work function can of our graphitized analyzer is equal to 4.375 eV.

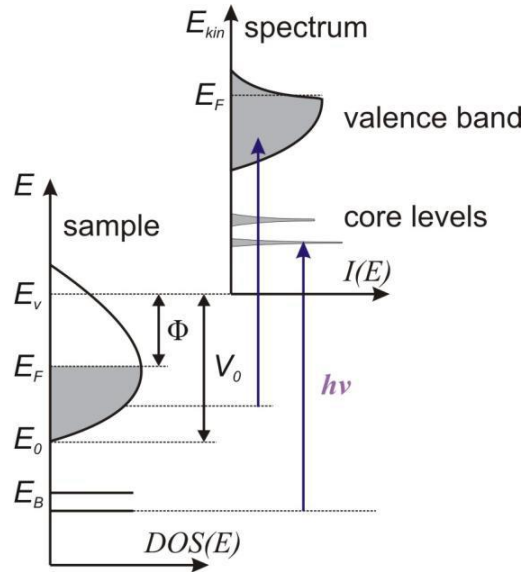


Figure 2.1 Energy diagram showing the bands inside a solid and its relation to the kinetic energy of photoelectrons. (Adapted from [Hüf95])

2.2 The Three-step and One-step Model of Photoemission

The process of photoemission is complicated from the viewpoint of quantum physics, and it is a single-step quantum mechanics event. Some phenomenological models, such as the three-step and one-step model of the photoemission process have been established. For the one-step model [Fei74], photon absorption, electron removal, and electron detection are treated as a single coherent process. In this case bulk, surface, and vacuum have to be included in the Hamiltonian describing the crystal, which implies that not only bulk states have to be considered, but also surface and evanescent states, as well as surface resonances. To develop a formal description and due to the complexity of the one-step model, a phenomenological three-step model is introduced to describe the process of photoemission. The simpler three-step [Fan45 Ber64] model breaks the photoemission process up into three distinct processes:

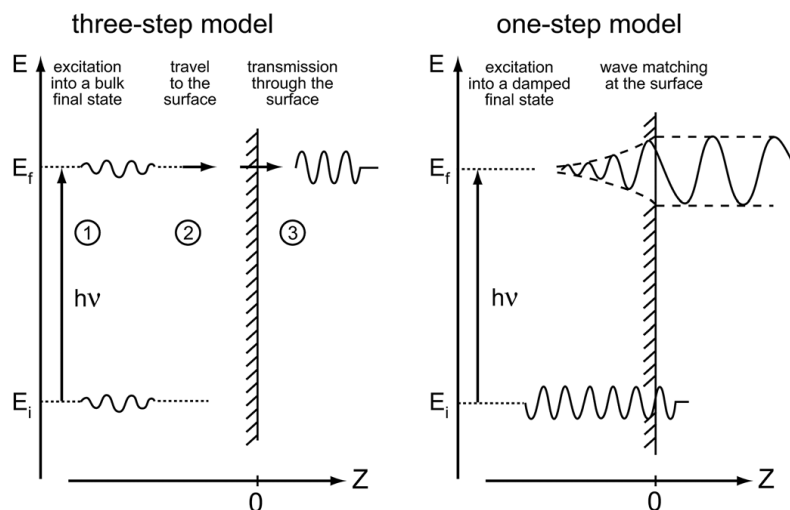


Figure 2.2 Pictorial representation of three-step and one-step model descriptions of the photoemission process. (Adapted from [Hüf95])

Step 1: Optical excitation of the electron in the bulk, a photon interacts with a single electron. The probability is proportional to Fermi's golden rule where the electron interacts with the electromagnetic potential inside the crystal and the energy and momentum are conserved.

Step 2: Travel of the excited electron to the surface, the electron travels to the surface of the crystal with a probability proportional to its mean free path. In this step, scattering processes such as e-e scattering or scattering at defects can modify the electron momentum and energy, which contributes to the background of the photoemission signal in form of secondary electrons. The classical example of electron inelastic mean free path vs. kinetic energy of the photoelectrons is given by figure 2.2. The electron mean free path determines how deep into a sample ARPES studies, one can achieve better bulk sensitivity by using either lower or significant higher photon energy.

Step 3: Escape of the photoelectron into the vacuum, the electron is only allowed to leave the surface if it has enough energy as compared to the work function of the material. Specifically, the perpendicular component of momentum corresponding to a kinetic energy needs to be larger than the sum of the work function and the inner potential.

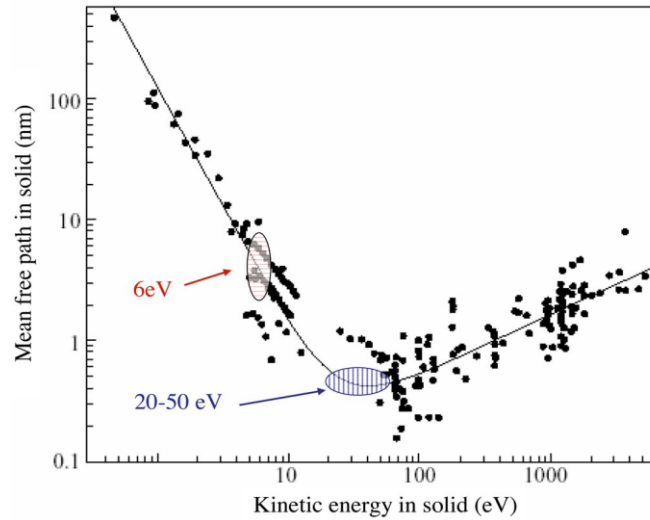


Figure 2.3 The mean free path of photoelectrons in solids is mostly material independent and determined by the kinetic energy of the photoelectrons via the "universal curve" of the mean free path of electrons, which exhibits a pronounced minimum around $E_{\text{kin}} \sim 30$ eV. From Ref.[Sea79, Kor07].

The photoemission data are usually discussed within the three-step model, which, although purely phenomenological, has proven to be rather successful. While the three-step model works as a conceptual idea, there are some issues that still need to be addressed in Step 1. Actually, to deduce the electronic structure of solids from photoelectrons, the sudden approximation should be satisfied. To make sure the photoelectrons carry the information of the electronic structure of solids, one has to assume that the time of photoelectrons traveling from the bulk to vacuum is much shorter than recovery time of the transient electronic system after emitting electrons. Based on this approximation, one could deduce the momentum and energy of electrons in solids using momentum and energy conservations.

2.3 Angle-resolved Photoemission Spectroscopy

Angle-resolved photoemission spectroscopy (ARPES) is one of the most direct methods of studying the electronic structure of solids. By measuring the kinetic energy and angular distribution of the electrons photoemitted from a sample illuminated with sufficiently high-energy radiation, one can gain information on both the energy and momentum of the electrons propagating inside a material. This is of

vital importance in elucidating the connection between electronic, magnetic, and chemical structure of solids, in particular for those complex systems, which cannot be appropriately described within the independent particle picture.

As shown in Fig. 2.1 an electron that absorb a photon with energy larger than the work function gains sufficient energy to escape from the sample. By measuring the energy and momentum of the photoelectron outside the sample and using conservation laws, one can derive the properties of the electron prior to the photoemission process. This information can then be used to reconstruct the energy-momentum dispersion relationship (band structure), and many other electronic properties of the solid. The momentum of the photo-electron in the vacuum (K) is related to the energy of the photo-electron, E_{kin} , by the following equation:

$$K = \sqrt{\frac{2mE_{kin}}{\hbar^2}}$$

where m is the mass of the free electron and \hbar is the Planck's constant ($4.135 \times 10^{-15} \text{ eV} \cdot \text{s}$). The coefficient $\sqrt{\frac{2m}{\hbar^2}}$ is $0.512 \text{ \AA}^{-1}(\text{eV})^{-1/2}$. The momentum of the electron can be written as the sum of two components, parallel and perpendicular to the sample's surface:

$$K_p = K_x + K_y$$

and

$$K_{\perp} = K_z$$

The momentum and energy relation for the individual components, according to their emission angles in spherical coordinates in the reference of sample surface (see the frame in figure 2.4) are as follows:

$$K_x = \sqrt{\frac{2mE_{kin}}{\hbar^2}} \cdot \sin\theta \cos\varphi$$

$$K_y = \sqrt{\frac{2mE_{kin}}{\hbar^2}} \cdot \sin\theta \sin\varphi$$

and

$$K_z = \sqrt{\frac{2mE_{kin}}{\hbar^2}} \cdot \cos\theta$$

The two angles are defined in Figure 2.4. These are the energy-momentum [$E_{kin}(K)$] relationships for the electron outside the sample, however, one actually wants to determine $E(k)$, the energy-momentum relation inside the sample. Lower case "k" is used for the momentum of the electron in the sample, and a upper case "K" for the momentum of the vacuum electron.

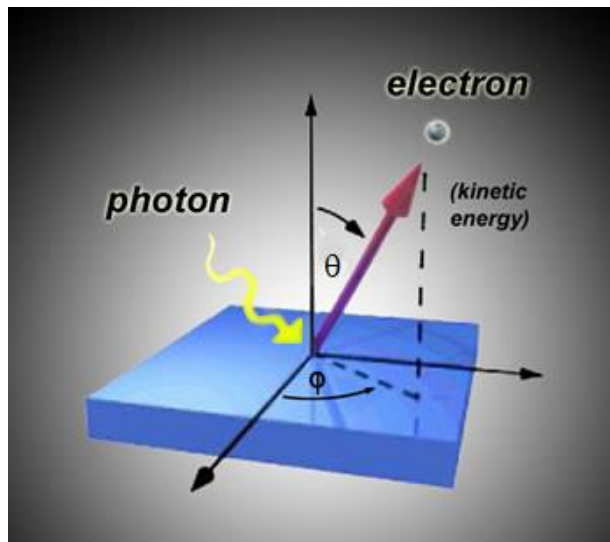


Figure 2.4 schematic diagrams of a outgoing excited electrons in a ARPES setup [Adapted from Wan13].

During the photoemission process, some of the components of the electrons momentum and energy are conserved while others are not. Because of the translational symmetry in the x-y plane (the surface plane of the sample) and the absences of a parallel component of the surface potential, the electron's parallel component of momentum is conserved:

$$k_p = K_p = \sqrt{\frac{2mE_{kin}}{\hbar^2}} \cdot \sin\theta$$

The momentum of the photon is very small compared to the momentum of the photoelectrons (for the typical photon energies used in low energy ARPES experiments) so it was neglected. The situation for k_{\perp} becomes more complicated because of the presence of a surface potential (V_0) whose gradient is perpendicular to the surface. The surface potential is an adjustable parameter that describes the dispersion of the final state within the free electron approximation. The perpendicular component of momentum is not conserved but it will reasonably peak around a value related to the surface potential V_0 by:

$$K_{\perp} = \sqrt{\frac{2m(E_{kin} + V_0)}{\hbar^2}} \cdot \cos\theta$$

V_0 can be determined by examining only the electrons emitted perpendicular to the surface, measuring their kinetic energy as a function of incident photon energy. But a particular case in which the uncertainty in k_{\perp} is less relevant is the one of the low-dimensional systems. These ones are characterized by an anisotropic electronic structure and, in particular, a negligible dispersion along the z-axis. It is the case for two-dimensional copper oxide superconductors, which hold weak forces between crystallographic planes. In the following of this work we will always consider such quasi-2D materials and the electronic dispersion will be exclusively determined by the parallel component of the electronic wavevector k_{\parallel} . As a result, one can map out in detail the electronic dispersion relations $E(k_p)$ simply by tracking, as a function of K_p , the energy position of the peaks detected in the ARPES spectra for different take-off angles.

Even more interestingly, ARPES can be easily extended to the case of strongly interacting electronic systems. If one keeps many-body interactions into account, the final state is no longer an eigenstate of system with the photo-hole. Its spectrum is not infinitely sharp, but has an internal energetic structure given by the spectral function $A(\vec{k}, \omega)$ of the removed electron. This represent the overlap of a single particle

excitation with the eigenstates of the N-1 correlated electron.

Remarkably, in two-dimensional systems, the PES spectrum $I(\vec{k}, \omega)$ of intensity is a direct measure of the single-particle spectral function $A(\vec{k}, \omega)$ and it is given by:

$$I(\vec{k}, \omega) = M A(\vec{k}, \omega) f(\omega)$$

where $M = \sum_{i,j} \left| \langle f | \vec{P} \cdot \vec{A} | i \rangle \right|^2$ (\vec{P} is the QP momentum and \vec{A} is the vector potential) is a (generally angle- and photon-energy-dependent) photoemission matrix element, and $f(E)$ is the Fermi-Dirac distribution function. $A(\vec{k}, \omega)$ describes the probability of removing or adding an electron with a given K momentum and energy $\hbar\omega$ to a many body system.

$$A(\vec{k}, \omega) = -\frac{1}{\pi} \frac{\Sigma''(\vec{k}, \omega)}{[\omega - \varepsilon_k - \Sigma'(\vec{k}, \omega)]^2 + [\Sigma''(\vec{k}, \omega)]^2}$$

$A(\vec{k}, \omega)$ can be also expressed in terms of a 'self-energy' $\Sigma(\vec{k}, \omega)$, which encodes information on the dressing of quasiparticles via interactions with the remainder of the system. As shown in figure 2.5, the real part of the self-energy gives the shift of the particles binding energy while the imaginary part is related to the lifetime of the particle's state. And ε_k is the bare electronic dispersion of the sample without interactions.

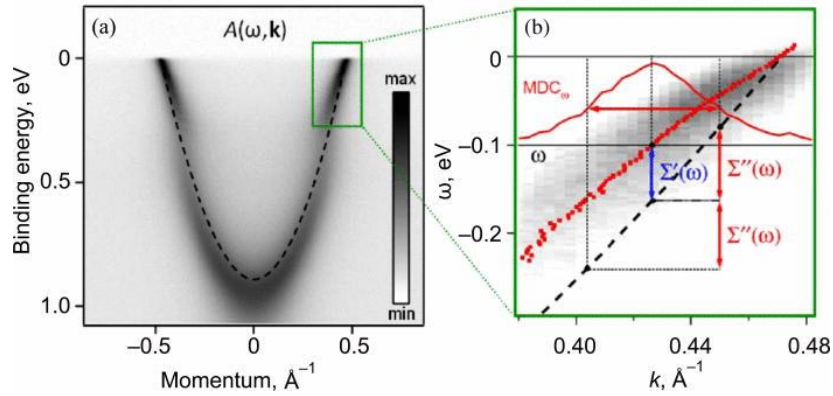


Figure 2.5 ARPES-spectrum which represents, the one-electron spectral function $A(\omega, k)$ (a). Relation of the experimental distribution of electrons with the “bare” dispersion of non-interacting electrons $\epsilon(k)$ and the self-energy of quasiparticles (one-electron excitations) $\Sigma = \Sigma' + i \Sigma''$ (b). [Kor14]

ARPES has become a very important technique because it offers direct access to the single-particle spectral function in reciprocal k -space [Dam03]. In the last decades, its contributions had a significant impact on our current understanding of the electronic ground state properties of solid state materials. In particular, in the case of the cuprate HTSCs, ARPES has played a crucial role in determining the effects of correlations on the electronic structure throughout the phase diagram. Part of the experiment reported in this thesis were performed at the ARPES end-station at the CASSIOPPE beamline of SOLEIL in France. In the following we will provide a detailed description of the end station with the manipulator and the electron analyzer.

It is important to notice that ARPES is highly surface sensitive, because of the strong inelastic scattering that may experience the electrons tunneling out of the sample. It is possible to quantify the effective thickness probed by the ARPES technique by measuring such scattering rate. The mean free path of electrons in solids, as depicted in figure 2.3, is nearly independent of the material and shows a strong variation with the kinetic energy of the photoelectrons given by the so-called "universal curve". The escape depth exhibits a minimum of only a few \AA at $E_{\text{kin}} \sim 30 \text{ eV}$, where the PES is most surface sensitive. For the low kinetic energies at a probe photon energy of 6 eV as used in this thesis for the Tr-ARPES and 55eV for ARPES at CASSIOPEE, the escape depth amounts to a $\sim 30 \text{ \AA}$ and 5 \AA , respectively. This aspect limits somehow our investigations only to samples in which high quality crystalline surfaces can be

prepared.

2.3.1 ARPES CASSIOPEE end station

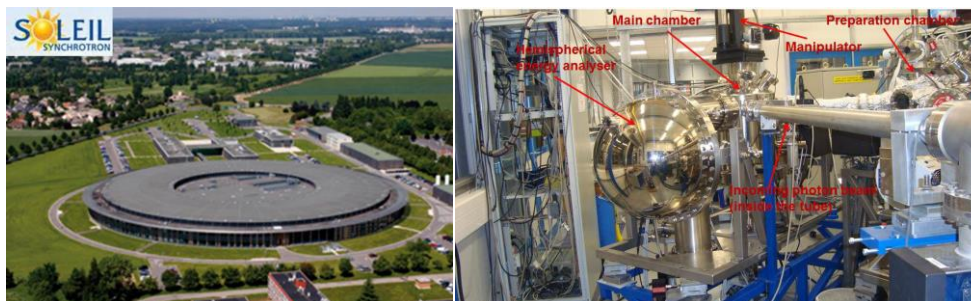


Figure 2.6 (a) A picture of the Soleil synchrotron radiation facility situated in Paris, France. (b) A picture of the Cassiopee beamline of the Soleil synchrotron. Different main parts of this beamline (hemispherical energy analyser, preparation chamber, incoming photon beam tube, main chamber and manipulator) are shown of this picture.

Figure 2.6 (a) shows a picture of the Soleil synchrotron radiation facility situated in Paris, France. All the ARPES data of LNSCO, LSCO, LBCO collected in this work were taken at Cassiopee (Combined Angle and Spin Spectroscopies Of PhotoEmitted Electrons) beamline at Soleil. Figure 2.6 (b) shows the picture of the experimental chamber at Cassiopee ARPES end station, and the main parts of this beamline are labelled on this picture. Cassiopee is a soft X-ray beamline dedicated to high resolution ARPES, spin-resolved photoemission and resonant spectroscopies in the 8 to 1500 eV photon energy range. This beamline uses two undulators as a source of radiation, characterized by high flux and adjustable polarization. The energy is selected by a high-resolution plane grating monochromator (PGM) with variable line spacing (VLC) and variable groove depth (VGD) gratings for the best flux intensity and monochromaticity of light. After the monochromator, the beamline is divided into two branches, supplying photons to two end stations, namely the high-resolution ARPES endstation and spin-resolved photoemission endstation, both connected to a molecular beam epitaxy chamber for sample growth and characterisation. The measurement chamber of Cassiopee is equipped with a 4-axis sample holder. The ARPES endstation is equipped with a Scienta R4000 electron energy analyser that is used to measure the photoemitted electrons from the sample.

The ARPES setup is composed of three UHV chambers: a load-lock, one-preparation chambers and a measurement chamber. A picture of the CASSIOPEE end-station is shown in figure 2.6 (b). The actual ARPES experiment is performed in the measurement chamber, which is directly connected to the beamline. The electron analyzer is also connected to the measurement chamber and its optical axis is aligned at 45° to the beamline in the horizontal plane. To avoid sample degradation and preserve the high vacuum of the beamline, the typical pressure is in the order of 5×10^{-11} mbar. The sample should first be introduced into load-lock and then transferred through preparation chamber to the cryogenic manipulator of the measurement chamber, where the sample is mounted. In addition, the sample in the measurement chamber can be cooled down to 5 K using a liquid He cryostat. The common method to obtain a clean and atomically flat surface is to *in situ* cleave the sample under UHV (10^{-11} mbar). This process is usually performed in the measurement chamber.

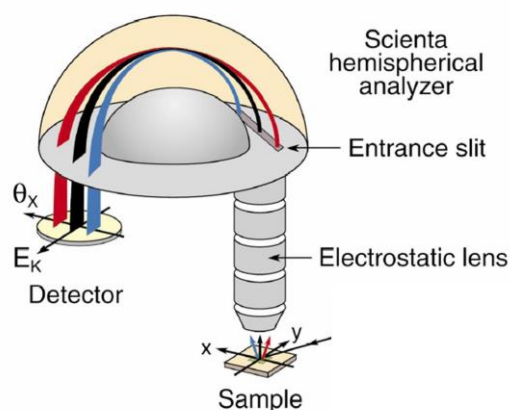


Figure 2.7 A schematic illustration of the functionality of a Scienta electron analyzer with 2D detector, showing energy and angular detection system. (Figure from Ref. [Dam03].)

The photon beam from the beamline hits the sample where electrons are "kicked out" and guided through the analyser. Figure 2.7 shows a picture of a typical Scienta R4000 electron energy analyser that was used in the ARPES experiment of this work at Cassiopee. The analyzer is composed of two parts; the lens that does the angular sorting and the hemisphere that does the energy sorting. After electrons have passed through the hemispheres, they are separated according to their angle and kinetic energy and subsequently hit a multichanneltron detector. The Gammadata Scienta

analyser, which mounts such kind of 2-dimensional detectors, has brought great efficiency in the rate of data acquisition since many kinetic energies and emission angles of the photoelectrons can be detected in parallel. In one direction, the emission angle φ of the photoemitted electrons is resolved whereas on the other perpendicular direction, the kinetic energy is being measured. The energetic and angular resolution of the analyzer can be tuned by changing, e.g the analyzer slit or its pass energy. Moreover, depending on how the analyzer is attached to the UHV chamber, the slit can be vertical or horizontal. These two geometrical configurations have to be taken into account, particularly when converting the detector angles into \vec{k} -space. For the ARPES experiment, samples were mounted on a cryostat, with a rotation around the vertical direction, and cleaved in situ in the ultravacuum with pressure less than 5×10^{-11} torr at low temperature. The light source is a HU256 electromagnetic undulator followed by a customized SX700 Variable Groove Depth Gratings monochromator. For our experiments, we selected a horizontal linear polarized light, at 55eV, and we set the monochromator slit in order to guaranty a spectral broadening below of 15meV. Photoemitted electrons were collected using the wide-angle 30° mode, with vertical slits 0.3 mm and pass energy 10eV, allowing for a total resolution of about 21meV. We could cover several Brillouin zones in reciprocal space by rotating the polar angle of the cryogenic manipulator where our sample is mounted. By these means, we could study the Fermi surface topology (e.g. the nesting and Fermi arcs) at low and high energy, and how the pseudo-gap and superconducting gap evolve as a function of temperature and doping.

2.4 Time- and Angle-Resolved Photoemission Spectroscopy

Roughly 30 years ago, with the development of ultrafast laser sources, it has been possible to extend the ARPES measurements to the investigation of non equilibrium systems. An experimental technique that has been successfully employed to perform a time dependent spectroscopy of unoccupied states is two-photon photoemission (2PPE). Nowadays, this is an established and powerful tool to study the dynamics of the hot electron distribution and of surface- and image potential states at energies high above the Fermi level. The 2PPE uses an ultra-short pump pulse to transiently excite electrons into states with $E > E_F$, and a subsequent probe pulse to photoemit electrons above the vacuum level. This approach allows also to monitor the temporal evolution

of the transient population of unoccupied states by varying the delay between the two pulses with Femtosecond (fs) resolution. In the usual scheme of 2PPE, both photon energies are below the metal work function so that no signal arising from direct photoemission can take place. The excitation densities are usually weak in order to study a small perturbation of the system.

In parallel to the development of 2PPE, the first study on the electron thermalization in metals has been performed by Time-resolved photoemission spectroscopy [Fuj84 Hai88]. Time and Angle resolved photoelectron spectroscopy (TrARPES) is conceptually similar to 2PPE but, the former makes use of a probe photon energy that is larger than the work function, which allows for the spectroscopy of both occupied and unoccupied electronic states.

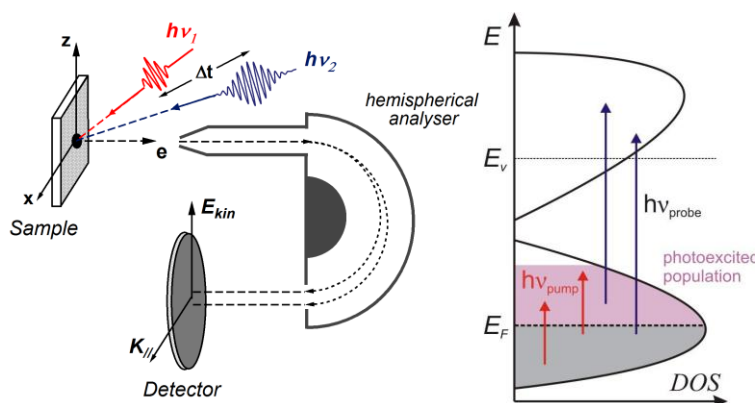


Figure 2.8 (a) Experimental geometry of the pump-probe ARPES configuration: $h\nu_1$ is the pump excitation and $h\nu_2$ is the probe photon. (b) A time-resolved ARPES energy diagram. Infrared photons (red) transfer electrons from the states below the Fermi level to states above E_F . Upon the illumination of UV photons that arrive at certain delay from the pump pulse, all the states that have finite electron occupation undergo photoemission and are thus detected. ([Adapted from Wan12])

Time-resolved ARPES (TrARPES) is based on the usual pump-probe scheme widely employed in the study of ultrafast dynamics. As shown in figure 2.8, optical transitions induced by the pump pulse promote electrons into the empty states above the Fermi level. The probe beam impinges the sample at variable time delay Δt after the excitation from the pump pulse. Being in Ultraviolet spectral region the probe photons can induce photoemission and thereby provide a snapshot of the transient

state of the sample. The photoemitted electrons are collected by an ARPES spectrometer to map out the spectrum as a function of kinetic energy and emission angle. By gradually delaying the arrival time of the probe pulse with respect to the pump pulse, represented by the Δt in figure 2.8(a), the temporal evolution of the photoexcited sample can be followed in time: from short time scales, about tenth of fs, to longer time scales of more than a few hundreds of ps. Different types of relaxations processes (electron-electron, electron-phonon scattering...) have different characteristic decay times, and allow for a relaxation of the system back to the equilibrium state.

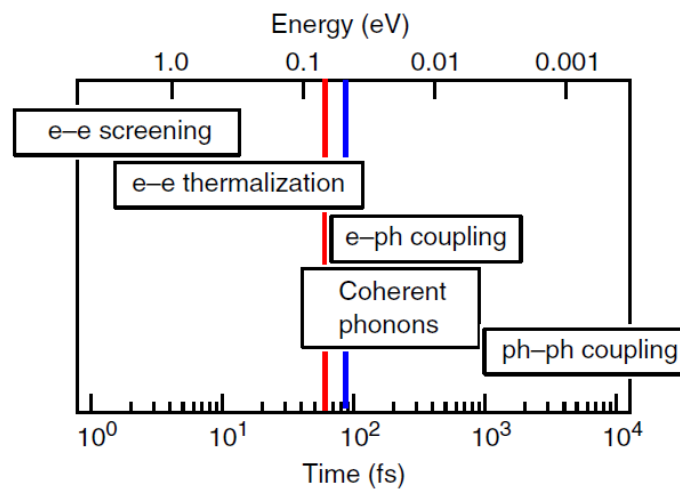


Figure 2.9 Typical timescales (bottom axis) and energy scales (top axis) of coherent phonons, e–e interaction, e–ph interaction and ph–ph interaction in correlated metals. The red and blue line indicates the temporal duration of our pump pulse and probe pulse, respectively [Per08].

As shown in figure 2.9 [Per08], the scattering processes due to el–el and el–ph interactions take place on quite different timescales. It follows that laser pulses with duration of 10–100 fs are short enough in order to monitor the energy dissipation of the hot electrons into lattice modes but long enough in order to perform a spectroscopic investigation of the electronic degrees of freedom. For this approach to be possible it is indeed necessary that the duration of the probing pulse is larger than the typical timescale of electron-electron interaction. When this condition is satisfied, the time resolved photoemission signal will be proportional to the Fourier transform of the electronic propagator with respect to the relative time, namely:

$$P(t) \propto -\frac{i}{\hbar^2} \int_{t_0}^t dt_2 \int_{t_0}^{t_2} dt_1 s(t_2) s(t_1) e^{i\omega(t_2-t_1)} G_k^{ret}(t_1, t_2)$$

in which t_0 is the time when pump is turned on, and t is the delay time between the pump and probe pulse, $s(t_1)$ and $s(t_2)$ are probe pulse envelope function, G_k^{ret} represents the retarded Green's function. In the following we will implicitly make this assumption for the data analysis. The reader interested in the more general theory of time resolved photoemission can find it in Ref. [Fre09].

The rather intense pump pulses that are commonly employed in Tr-ARPES drive the system far from equilibrium condition. Within the arrival of the pump pulse electrons are photoexcited in initially unoccupied states, giving rise to a non-thermal state. As shown by the schematic sketch of figure 2.10, few tens of femtoseconds after photoexcitation, the hot electrons thermalize via e-e scattering and converge to a Fermi-Dirac distribution with effective electronic temperature T_e much larger than the lattice temperature T_l .

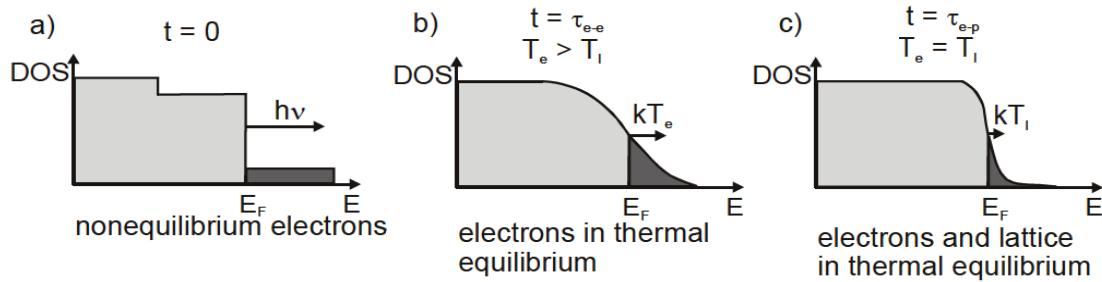


Figure 2.10 Ultrafast thermalization of electrons after photoexcitation. The electrons and lattice are under thermal equilibrium before the photoexcitation. ([Adapted from Wan12])

To illustrate the “cooling” of hot electrons after the sudden photoexcitation, the electron and lattice (phonon) temperatures are shown in figure 2.11. In most metallic systems, a rapid cooling of the thermalized hot electrons can be observed. Depending on the phonon and electronic spectrum of the material, this relaxation can last from 100 fs up to few picoseconds. In practice, the excited electronic system exchanges heat with the lattice by emitting phonons, so that the electronic temperature decreases. At the same time the lattice temperature increases until the electrons and phonons

reach a quasi-thermal equilibrium. To a first approximation, the electronic temperature (T_e) and lattice temperature (T_l) as a function of t can be described by the two coupled differential equations [Per07, All87]. The big heat capacity of the lattice in comparison with the one of the electrons explains the low rise of lattice temperature after hot electrons cooling. The relaxation time of electrons gives us important information about the electron-phonon interaction and helps us to assess the relevance of lattice modes to electronic transport and to the pairing mechanism in high temperature superconductors [Per07].

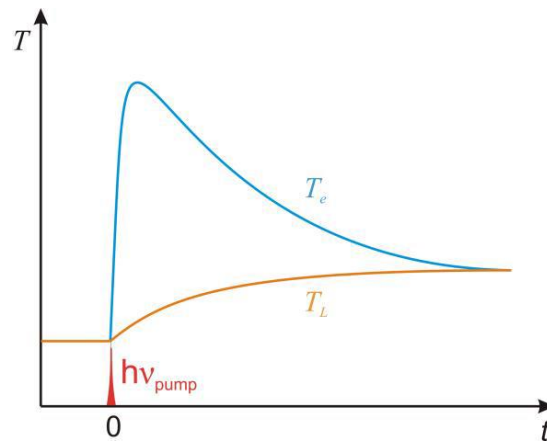


Figure 2.11 Ultrafast electron cooling by the lattice. The electronic temperature (T_e) and lattice temperature (T_l) as a function of t can be described by the two-temperature model. ([adapted from Wan12])

More generally, TrARPES represents a powerful technique that is capable of adding information about emergent phenomena in condensed matter. Using Tr-ARPES, one can observe photoinduced phase transitions [Per06 Roh11] and transient states that have analog in equilibrium conditions. This opens completely new benchmarks for theories describing dynamical phase transitions far from equilibrium [Fre09, Mor10]. Nowadays trARPES has become a rather established technique and it is often employed to study the dynamics of electronic, lattice and magnetic order in many strongly correlated electron systems [Huf03, Sma12]. The Tr-ARPES setup used for our experiments is FemtoARPES, and is located in Synchrotron Soleil (France). In the following I will provide a more detailed description of this setup, as well as a general introduction to pump-probe spectroscopies.

2.4.1 Experimental setup

As shown in figure 2.12, we combine a Ti: Sapphire laser source with a state of the art ARPES setup. FemtoARPES has three major components: laser source, the optics for generating UV and pulses and an Ultra High Vacuum platform, where to perform Angle Resolved Photoelectron Spectroscopy.

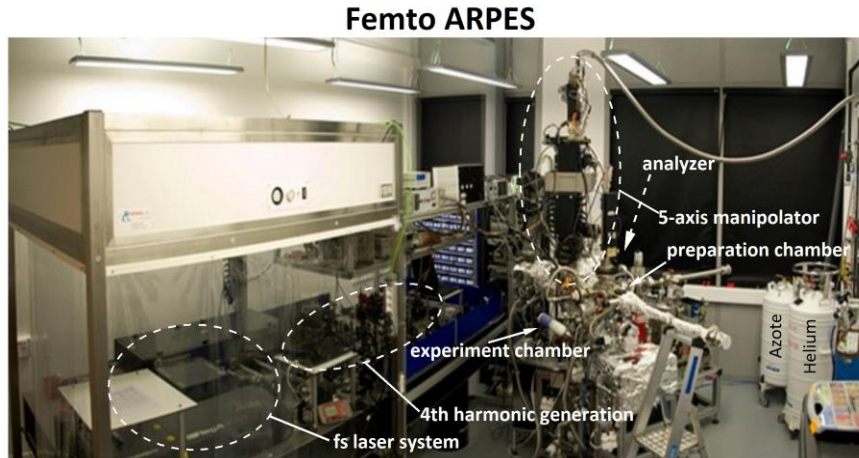


Figure 2.12 FemtoARPES experiment room

The femtosecond laser system is a regenerative Ti: Sapphire laser system (RegA by Coherent). The laser has high repetition rate (250 kHz) and delivers $6\mu\text{J}$ per pulse with 35 fs duration at FWHM (Full Width Half Maximum). On one hand the available energy per pulse allows to strongly photoexcite the system. On the other hand the high repetition rate is essential in order to acquire spectra with good statistic and negligible space charge distortion. The space charge effect originates from repulsive Coulomb forces that photoelectrons exert on each other when they pass in vacuum between the sample and the photoelectron detector, and results in a reduced kinetic energy for the lowest-energy photoelectrons, an increased kinetic energy for photoelectrons at the Fermi edge, and an overall smearing of the wave packet features.

The laser wavelength can be tuned between 780 nm and 820 nm for a safe and stable operation. Since the laser light generated from a Ti: Sapphire regenerative amplifier or Oscillator is only 1.55 eV, much less than the 4~5eV work function of most materials, higher harmonics of these light are needed for the photoemission process.

This is realized through the nonlinear optical processes. The generation of the fourth harmonics (FH) of the laser system is depicted on figure 2.13. A beam splitter selects a portion of the energy, which is then used for FH generation.

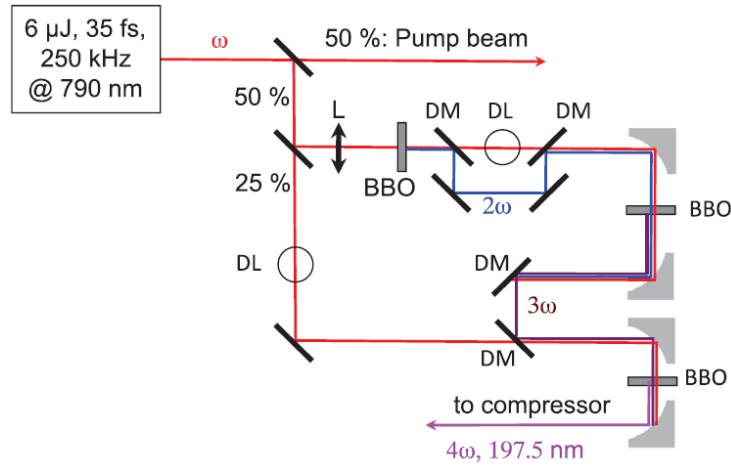


Figure 2.13 The generation of the fourth harmonic using crystal (β -BBO). (Adapted from [Fau12])

The schematic of the setup is shown on figure 2.13. The fundamental light with center wavelength at 790 nm enters the first BBO crystal and the second harmonic (SH) light is generated. The second harmonic pulse is delayed with respect to the fundamental when both leave the first BBO crystals. This time difference can reach 100 fs for a 1mm thick crystal and are compensated by the optical delay line (DL) with a delay stage in order to generate the third harmonic. Following SH generation, all optics on UV beams are reflective in order to avoid dispersion. There are two ways to reach the fourth harmonic of a Ti: Sapphire laser for photoemission using BBO crystals. The first is frequency-doubling (SH) twice and the second is mixing the fundamental with doubled light for third harmonic (TH) and mixing fundamental and third again to get to the fourth harmonic (FH). The latter approach has been chosen for our setup. The fourth-harmonic light has photon energy of 6.28 eV (197.5nm) and can reach 10^{12} photons/s.

Because of the presence of dispersion in any material, including air, a short pulse becomes broadened due to group velocity dispersion which causes a frequency chirps in the pulse. The pulsewidth of such kind of pulse can be compressed temporally by either using gratings or prisms to compensate for the chirp. By using a prism pair

compressor, these components could overlap in time when they pass through two prisms and result in the shortest pulse duration. This compensation can be adjusted by controlling the distance between the two prisms as well as the distance the beam travels in the second prism. After compression, the pulsewidth is typically 80 fs.

The temporal delay between the 6.28 eV probe and the 1.55 eV pump beam is controlled via a motorized delay stage. The polarization of the pump and the probe beams can be controlled independently. The two beams are focused on to the sample surface inside the UHV chamber, allowing for the independently control of the focal diameters on the sample. To verify the spatial overlap of the two beams outside the UHV chamber, a flip mirror are placed in front of the chamber and a CCD is used to monitor the beam profiles. We always verify that the spatial quality is good, with a profile close to a Gaussian and a spot size at FWHM of $\sim 50\mu\text{m}$.

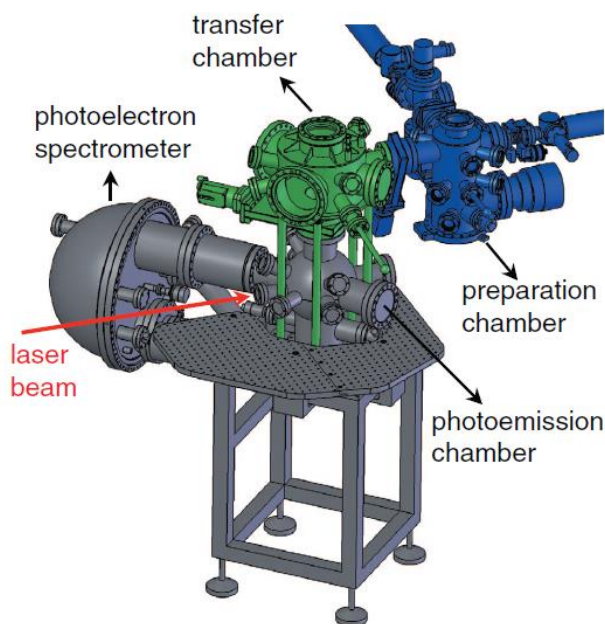


Figure 2.14 A 3D view of the experimental chambers and the analyzer. (Adapted from [Fau12])

As depicted in figure 2.14, the vacuum system consists of a preparation chamber, a transfer chamber and a photoemission chamber connected to the photoelectron spectrometer. The preparation chamber is equipped with an Ar gun for sputtering and the sample can be heated up to 1100 K in order to perform annealing-sputtering

cycles for surface preparation. In the transfer chamber, a low energy electron diffraction setup allows us to verify the quality of the surface *in situ*, just before performing photoemission experiments. The photoemission chamber is made of μ -metal in order to shield the magnetic fields at the sample position. Sources of residual static electric and magnetic fields have been carefully analyzed and removed. The spectrometer is a commercial hemispherical electron analyzer (Phoibos 150, Specs) providing angular resolution better than 0.1° and an energy resolution of about <10 meV. In order to minimize the adsorption of residual gas atoms, our measurement chamber has base pressure of a few 10^{-11} mbar, ensuring a relatively long lifetime of the clean surfaces to be analyzed.

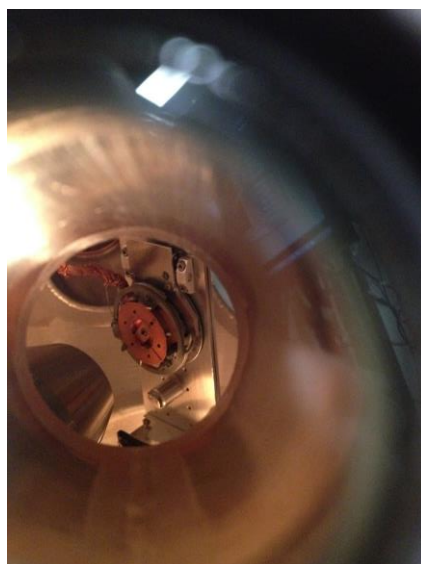


Figure 2.15 Sample holder with sample under photoexcitation

The sample manipulator has three translations (x, y, z) and two rotations, horizontal tilt, and azimuth (θ, φ) to control the emission angles and the sample's position. A cryostat is connected to the manipulator so that the sample can be cooled down to 35 K using liquid helium and 130 K using liquid nitrogen. The sample can also be heated to 1100 K, allowing one to perform experiments at both at cryogenic or high temperatures. The experiment is fully computer controlled via a homemade LabVIEW program. The program is able to acquire data while moving the manipulator and the translation stage of the delay line that is used for pump-probe experiment. This allows one to acquire large amounts of data automatically and in a consistent manner.

2.5 Magnetisation Measurements Using a SQUID

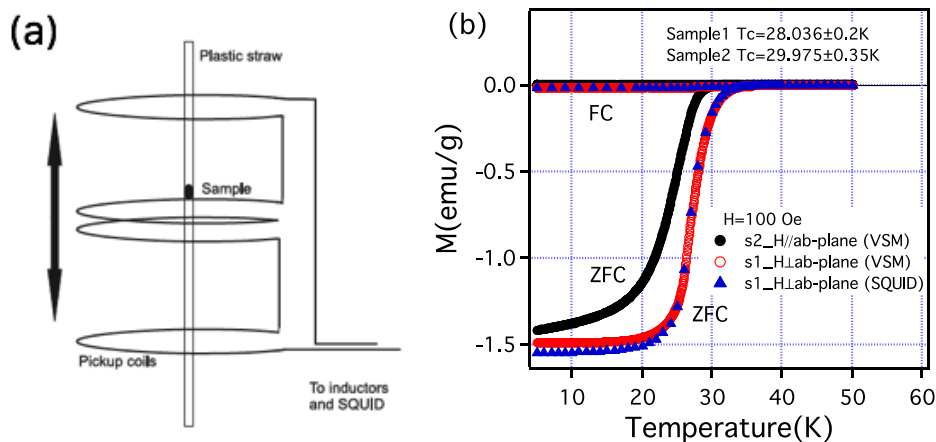


Figure 2.16 (a) The pickup coils of the SQUID magnetometer. (b) The Magnetization measurements of $\text{La}_{1.48}\text{Sr}_{0.12}\text{CuO}_4$ (LSCO) crystals grown the by floating zone technique. Temperature dependence of the magnetization under a filed of 100 Oe for the zero field cooled / field cooled (ZFC/FC) condition.

In this thesis the magnetization measurements are used to determine the superconducting transition temperature (T_c) of our superconductor samples and place them in the phase diagram of doped cuprates.

The magnetization measurements presented in this thesis were all taken using a Quantum Design MPMS XL magnetometer. This magnetometer works using a superconducting quantum interference device (SQUID) coil. The SQUID magnetometer is one of the most effective and sensitive ways of measuring magnetic properties and the only method, which allows us to directly determine the overall magnetic moment of a sample in absolute units. It can measure the strength of the magnetic moment produced by the magnetized sample with sensitivity of 10^{-8} emu. The sample environment is a Helium flow cryostat, which can be cooled to a base temperature of 1.9 K. A magnetic field is applied in the vertical direction by a superconducting magnet, which has a practical range of about ± 7 T. All of the measurements are computer controlled using software, which was designed specifically for this magnetometer by Quantum Design Inc. For a measurement of the magnetic susceptibility the sample is typically mounted in side a plastic straw of diameter ~ 5 mm, the diamagnetic moment of which is very small. It can be secured

inside the plastic straw either by placed inside a plastic capsule or wedged by two folded over straws inserted into the straw. The method chosen depended on the particular geometry of the sample and the crystallographic direction in which the field needed to be applied. The principle of operation of the apparatus is shown schematically in figure 2.16 (a). The detection coil is a single piece of superconducting wire wound is a set of three soils configured as a second-order (second-derivative) gradiometer. When installed in the MPMS, the coils are positioned at the center of the superconducting magnet outside the sample chamber. The plastic straw containing the sample is translated vertically between three superconducting coils, which are connected to the SQUID with superconducting wires, allowing the current from the detection coils to inductively couple to the SQUID sensor (extremely sensitive current to voltage convertor). Thus small changes in the sample magnetisation are measured as small current changes, which are converted into small changes in magnetic field near the SQUID. Two typical different measurements commonly used are the zero-field-cooled (ZFC) and the field-cooled (FC) measurement. The sample is cooled down to the lowest measurement temperature in $H=0$. Once stabilized, a magnetic field (50 Oe) is applied and the moment is measured as a function of temperature up to the highest desired temperature. This is the ZFC part. Next, the sample is cooled in this same field to the lowest temperature and again measured as a function of temperature. This is the FC part. The ZFC/FC method is very useful for determining the temperatures range over which system are irreversible. For our superconductor samples, the results of the ZFC measurement are shown in the following chapter.

2.6 Sample Preparation, Orientation and Cleaving Procedure

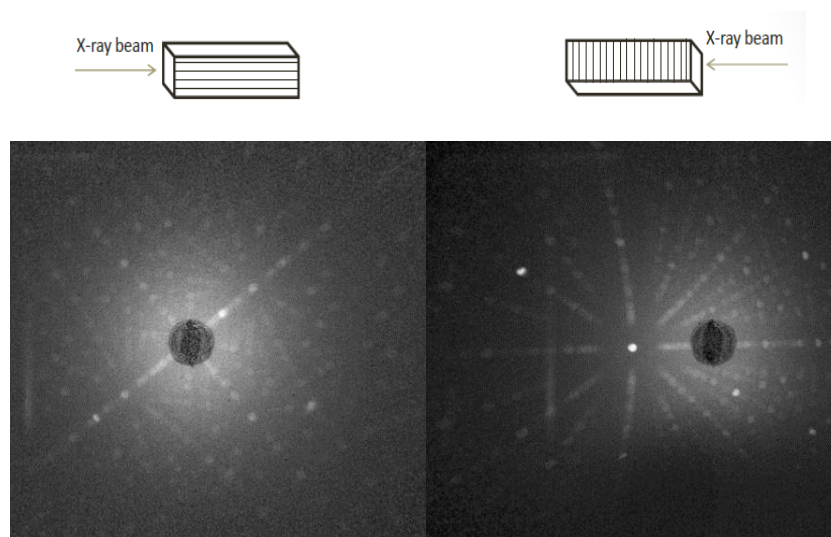


Figure 2.17 Needle like sample geometries were used for the measurements. X-ray laue pattern of (100/001) direction. The white spots mark the intensity from the backscattered Bragg peaks, and the black circle in the middle shows the center of the beam.

The lattice parameters of the crystals were first determined by powder X-ray diffraction, at LPCES (Orsay). Before the actual ARPES experiment, the crystallographic orientation of all samples were determined by the backscattering Laue X-ray technique, at LPCES (Orsay), so that the experimental measured Fermi surface maps are symmetric and unrotated in the first Brillouin zone in order to identify easily different matrix elements on the ARPES measured Fermi surface maps. Two examples of the Laue picture of LSCO samples are given in figure 2.17, the single crystal has a tetragonal symmetry and the lattice parameter were determined to be approximately $a \approx b = 3.74 \text{ \AA}$ and $c = 13.240 \text{ \AA}$ in usual High Temperature Tetragonal (HTT) phase. The recorded diffracted beam shows up as an array of spots forming a pattern on the image plate. These spots correspond to the intensity peaks from the Bragg diffraction. The created patterns have asymmetry reflecting the one of the crystal and the direction of the crystal axes are therefore determined by the symmetry axes of the pattern. With the help of the program Orient Express, by using the parameters from crystal unit cell and the high symmetry spots from the pattern, we are able to make a

fit of the spots and calculate from which plane each single point has been reflected. By labeling the spot/planes it is possible to determine the directions of the axes. The figure 2.17 (a) and (b) show that the X-ray beam is along the a-axis and c-axis, respectively.

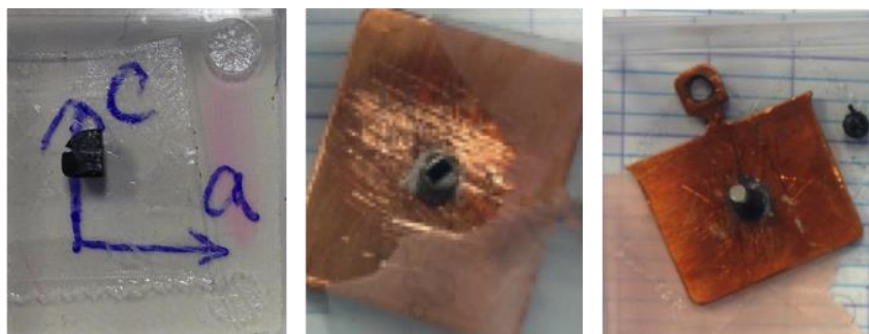


Figure 2.18 (a) A LSCO sample with a special notch on the side. (b) and (c) A LSCO sample positioned at the top of the sample holder before and after the top post has been glued on it.

The ARPES and Tr-ARPES measurements require a special mounting: single crystals of our samples were first mounted onto the sample holder using a conducting silver epoxy. This conductive glue was used in order to keep the sample electrically neutral under the photoemission process. Figure 2.18 (b) shows the top view of a sample, which is fixed on a sample holder using silver epoxy. After that, a top-post was glued at the top of the sample so that the sample is sandwiched between the sample holder and the top-post (see figure 2.18 (c) right). Then graphite was sprayed on the sample, including the sample holder, in order to create contrast in the signal coming from the sample during the experiment, so that it will be noticed when the photon beam is not well focused on the measured sample as well as increase conduction from the top of the sample. After that, the sample was inserted in the airlock chamber before it was transferred into the preparation chamber. Once the sample was transferred into the measurement chamber, on the manipulator, it was cleaved by mechanically removing the top-post with a screwdriver. In Figure 2.18 (a), we can see a special notch were put along the ab-plane of LSCO family samples, which can help us to get a flat surface during the *in-situ* cleave. But for the BSCCO samples measured with the Tr-ARPES, a notch is not necessary, as the CuO_2 planes are weakly bound, allowing easy cleaving perpendicular to them.

Chapter 3

Time- and angle-resolved photoemission spectroscopy (Tr-ARPES) study of the $\text{Bi}_2\text{Sr}_2\text{CaCu}_2\text{O}_{8+\delta}$

3.1 Time resolved Optical and THz measurements

The equilibrium properties of cuprates superconductors have been characterized by an impressive number of different techniques. Advances in ultrafast spectroscopy have facilitated an unprecedented ability to characterize and control quantum materials, as it makes it possible to track similarities and correlations that are not evident near equilibrium. Many pump-probe experiments have already monitored the dynamics of the condensate in copper oxides superconductors. The results reveal the typical relaxation timescales of quasiparticles in the superconducting phase.

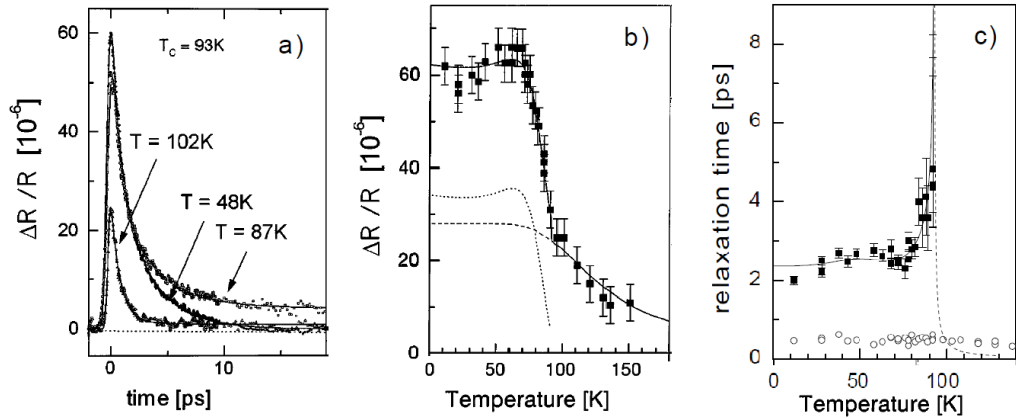


Figure 3.1 Transient reflectivity curve (a), maximal intensity of the response (b) and decay time constant (c) acquired in optimally doped YBCO for different base temperatures. This image has been freely adapted from Ref. [Dem99].

We show in figure 3.1(a) the time resolved reflectivity measurements that have been performed by Demsar *et al.* in optimally doped YBCO. The low excitation density employed for these measurements, lead to a weak perturbation of the superconducting phase. Just after photoexcitation, the electrons-holes pairs excited by the transient response rapidly relax near the Fermi energy by electron-electron and electron-phonon scattering, creating a non-equilibrium distribution of quasiparticles. The relaxation of such low energy excitations strongly depends on the sample temperature. When YBCO is in the superconducting state, the presence of an electronic gap at E_F causes a bottleneck in the relaxation dynamics. The recombination of quasiparticles into Cooper pairs takes place in several picoseconds and depends on pumping fluence [Dem99][Seg02]. Notice in figure 3.1(b) that an appreciable signal increase is already observed for temperatures 30% larger than the critical value. This effect can be explained by the combined presence of superconducting fluctuations and a pseudogap over a temperature range extending above the presence of long-range superconductivity. Many subsequent works have been focused on the detection of the pseudogap by time resolved optical means. The phase diagram that emerged from such kind of experiments is consistent with the one that we already introduced in chapter 1.

In the limit of the weak perturbation, the response of quasiparticle recombination can be isolated and modeled. Phenomenological rate equations, first introduced by

Rothwarf and Taylor (RT), could successfully account for the quasiparticle recombination in presence of non-equilibrium phonons. On the other hand, the photoexcited state generated by intense optical pulses is still poorly understood. Apparently, the dynamics of transient reflectivity changes only upon strong perturbation of the superconductor.

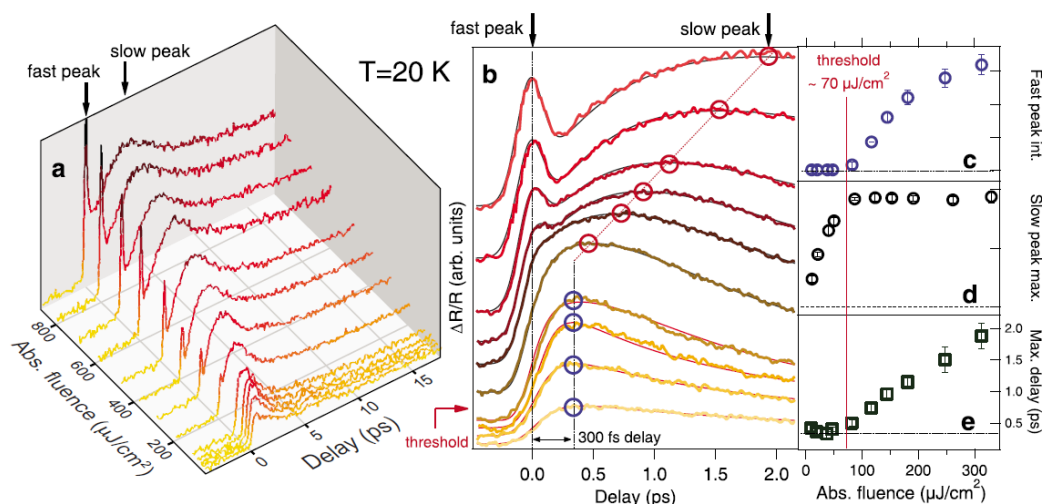


Figure 3.2 (a,b) Transient reflectivity traces of the superconducting phase ($T=20\text{ K}$) as a function of both the time delay and the absorbed pump fluence. (c) Intensity of the fast peak, after subtraction of the slow dynamics, as a function of the pump fluence. (d) Saturation of the slow component maximum above $70\ \mu\text{J}/\text{cm}^2$. (e) Position of the maximum of the transient signal as the pump fluence is increased. From Ref. [Gia09].

As shown in figure 3.2, Giannetti *et al.* reported a discontinuity of the transient optical response observed at the critical fluence of $70\ \mu\text{J}/\text{cm}^2$ [Gia09]. Below this threshold, they describe the dynamics by RT equations, whereas above the critical intensity a fast response is superimposed to the slower dynamics of the superconducting recovery. Remarkably, the electrons dynamics of the strongly driven superconductor is very different from the electronic relaxation observed in the normal phase. This finding suggests that superconducting correlations deeply affect the quasiparticle dynamics. One possibility is that superconducting coherence is lost whereas pairing survives to higher fluence. The second scenario would be a dramatic slowing down of the quasiparticles relaxation arising from a dynamical gap opening. Despite these interesting insights, many aspects of the non-equilibrium state induced by an intense and sudden photoexcitations can be only conjectured. This is because of the limited

information of an optical spectroscopy response, which does not directly probe elementary properties as the superfluid density, the single particle gap or the quasiparticle spectrum. As a consequence it is hard to relate the monitored signal to elementary properties of the superconducting phase. Such constrains calls for experimental probes that can address more directly the different aspect of the broken symmetry phase. One of such techniques is Time resolved THz. The low-energy electromagnetic response at THz frequencies couples directly to Cooper pairs. It can be expressed by the frequency-dependent complex conductivity governing the currents induced by a transverse THz electromagnetic field. Fourier transformation of the fields and straightforward electrodynamical relations yield both the equilibrium value and the pump-induced transient change of the THz conductivity. The conductivity within this spectral range can be described by the well-known two-fluid model, where ρ_{QP} and ρ_S denote the quasiparticle and superfluid densities. The first term is a Drude response of quasiparticles with momentum scattering rate $1/\tau$. This component fully accounts for the broadband conductivity above T_c . The ρ_S term constitutes the superfluid response emerging below T_c .

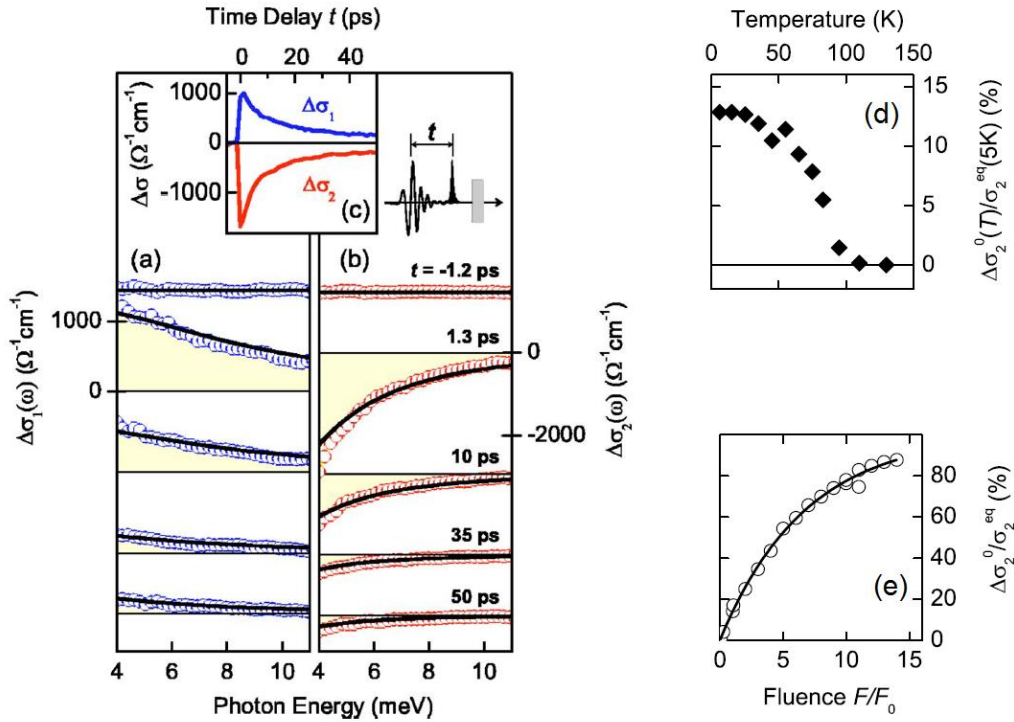


Figure 3.3 Induced THz conductivity changes, for $T=6$ K and $0.7 \mu\text{J}/\text{cm}^2$ excitation fluence. (a,b) Measured changes in the real part of conductivity and the imaginary part at different time delays t after excitation. Solid lines are fit based on the two-fluid model.(c) The transient conductivity changes at center probe energy vs pump-probe time delay. (d) Temperature dependent signal amplitude of imaginary part σ_2 at fixed pump fluence F_0 , normalized by the low-temperature equilibrium value (e) Amplitude σ_2 as a function of fluence, at $T=5$ K. The value of F_0 correspond to an incident fluence of $0.8 \mu\text{J}/\text{cm}^2$. From Ref. [Kai05] and Ref. [Car04].

Nonequilibrium changes of the THz conductivity in the superconducting state are shown in figure 3.3 for different time delays t after optical excitation. Immediately after excitation $t=1.3$ ps, the spectra exhibit a strongly frequency-dependent reduction of the imaginary part, along with a marked increase of the real part. Signs and shapes of these features indicate a reduced density of the superconducting condensate, with the spectral weight transferred into dissipative excitations. This conclusion is confirmed by corresponding changes predicted by the two-fluid model. The loss of superfluid density arises on a subpicosecond time scale via interactions with the initially photoexcited carriers. The temperature dependence of the signal amplitude is shown in figure 3.3 (d) which plots the fraction of the initial imaginary conductivity

change $\Delta\sigma_2^0(T)$ relative to its $T = 5$ K equilibrium value. It closely follows the temperature evolution of the equilibrium condensate spectral weight, and thus shows that a constant fraction of the supercurrents is suppressed through the near-visible excitation pulse. At fixed temperature, the photoinduced change in the imaginary part spectral weight does not increase above the equilibrium value but rather saturates with increasing pump fluence. Indeed, a plot of $\Delta\sigma_2^0/\sigma_2^{eq}$ at $T = 5\text{K}$ versus pump fluence (see figure 3.3 (e)) exhibits a saturation that yields an estimate of the saturation energy of $F_{phase} = 12 \mu\text{J}/\text{cm}^2$. This value is of relevance for the following of our work, since it allow us a comparison of the photoinduced loss of superfluid density with other observables.

3.2 Detection of quasiparticle dissipation rate by time resolved ARPES

Time and angle-resolved photoemission spectroscopy (Tr-ARPES) [Car09][Kir10][Fau12][Sma12_1] is ideally suited for probing both momentum-dependent quasiparticles [Nes98][Per07][Gra11][Cor11][Zha13][Ram14][Yan15] and related nonequilibrium properties in cuprates. In this work, we show that a detailed (tr-ARPES) analysis of the quasiparticles dynamics provides deep insights on the photoexcited state. The employed pumping fluence is always above the largest value sustained by long-range superconductivity. Despite it, the inelastic scattering of photoexcited quasiparticles displays a downturn below T_c . We ascribe such unusual finding to the buildup of superconducting correlations soon after the arrival of the pump pulse. This non-equilibrium state is qualitatively different from the fluctuating superconductor in equilibrium conditions. In the latter case, our measurements confirm that the pairing amplitude vanish when the temperature is raised slightly above T_c .

In this chapter, we present the results of time- and angle-resolved photoemission to measure quasiparticle relaxation dynamics of optimally doped $\text{Bi}_2\text{Sr}_2\text{CaCu}_2\text{O}_{8+\delta}$ (Bi-2212, $T_c=91\text{K}$). Whereas high fluence measurements of quasiparticle relaxation reveal a smoothly recovering picosecond dynamics, a sharply defined femtosecond quasiparticle relaxation component emerges when the sample is above T_c and the pump fluence is above $F_{pair} = 40\mu\text{J}/\text{cm}^2$. The nonequilibrium dynamics reveal that

an infrared pump pulse of sufficiently high fluence affects the ARPES spectra. We observed a time dependent shift of the quasiparticle band and quasiparticle broadening.

3.3 Preparations and Experimental details

We perform Tr-ARPES on optimally doped $\text{Bi}_2\text{Sr}_2\text{CaCu}_2\text{O}_{8+\delta}$ (Bi-2212) single crystals ($T_c = 91$ K), thin film of optimally doped Bi-2212 ($T_c = 72$ K) and thin film of optimally doped $\text{Bi}_2\text{Sr}_{2-x}\text{La}_x\text{CuO}_{6+\delta}$ (Bi-2201) ($T_c = 28$ K). The samples are mounted on a cryogenic manipulator and are cleaved at the base pressure of 6×10^{-11} mbar. Time-resolved measurements are carried out at 250 KHz in a pump-probe scheme: short and intense 40 fs laser pulses at a central energy of 1.55 eV drive the system far from equilibrium whereas the photoelectrons are emitted by time delayed pulses at 6.28 eV. Pump and probe beams are focused almost collinearly on the sample and have a cross correlation with FWHM of about 80 fs [Fau12]. The fluence of the pumping pulses has been carefully measured by imaging the focal point of the laser beams on an external camera.

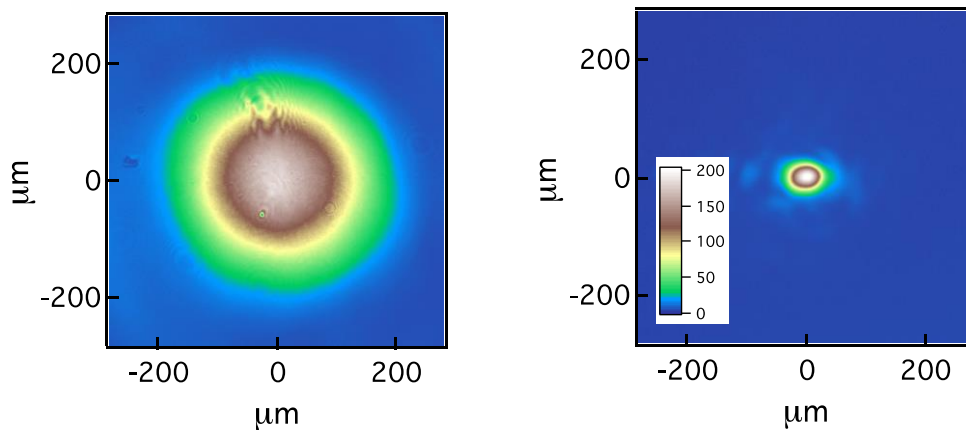


Figure 3.4 The intensity profiles of pump and probe pulses, experimentally determined by a CCD beam profiler. Pump pulse of $\text{FWHM}=266 \mu\text{m}$ and Probe pulse of $\text{FWHM}=42 \mu\text{m}$.

Figure 3.4 shows the intensity profile of the pump and probe beam when the spatial overlap and the pump-probe signal are maximal. We measure the average power just before the entrance of the UHV chamber and we weight the pump profile with the

probe one. By these means, we can precisely estimate the average fluence incident on the probed area of the sample. We set the probe beam polarization along the nodal plane of the crystal in order to maximize the photoelectron signal generated by the quasiparticles. Photoelectron spectra are acquired with an angular resolution better than 0.1° and an energy resolution of 70 meV. The typical probing depth of emitted photoelectrons is few nanometers whereas the optical penetration of the pump beam is roughly 150 nm. As a consequence, our experiment probes a region at the surface of the sample with nearly uniform excitation density. In order to avoid thermal heating, the repetition rate has been reduced to 100 KHz for pumping fluence above $150 \mu\text{J}/\text{cm}^2$. The absence of a photoinduced signal at negative pump-probe delays guaranties that the average heating of the surface is always negligible.

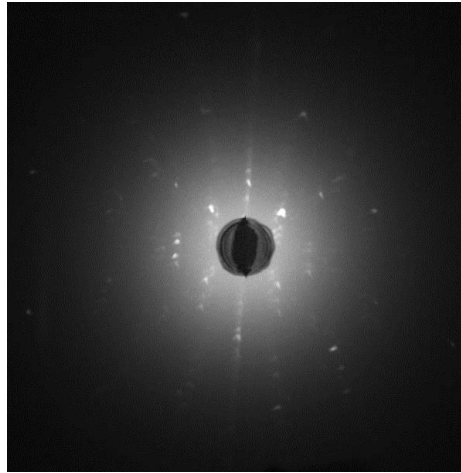


Figure 3.5 The X-ray Laue diffraction pattern of the (001) plane (the *ab*-plane) for the optimal doped Bi-2212 single crystal.

Figure 3.5 shows an example of back-scattering x-ray Laue patterns used for crystal orientation, which is a result, obtained on (001) plane (*ab*-plane) of optimal doped Bi-2212 single crystal and shows clear and uniform diffraction spots with the 4-fold axis asymmetry.

3.4 Quasiparticle dynamics in $\text{Bi}_2\text{Sr}_2\text{CaCu}_2\text{O}_{8+\delta}$

3.4.1 Redistribution of spectral weight in the Quasiparticle peak

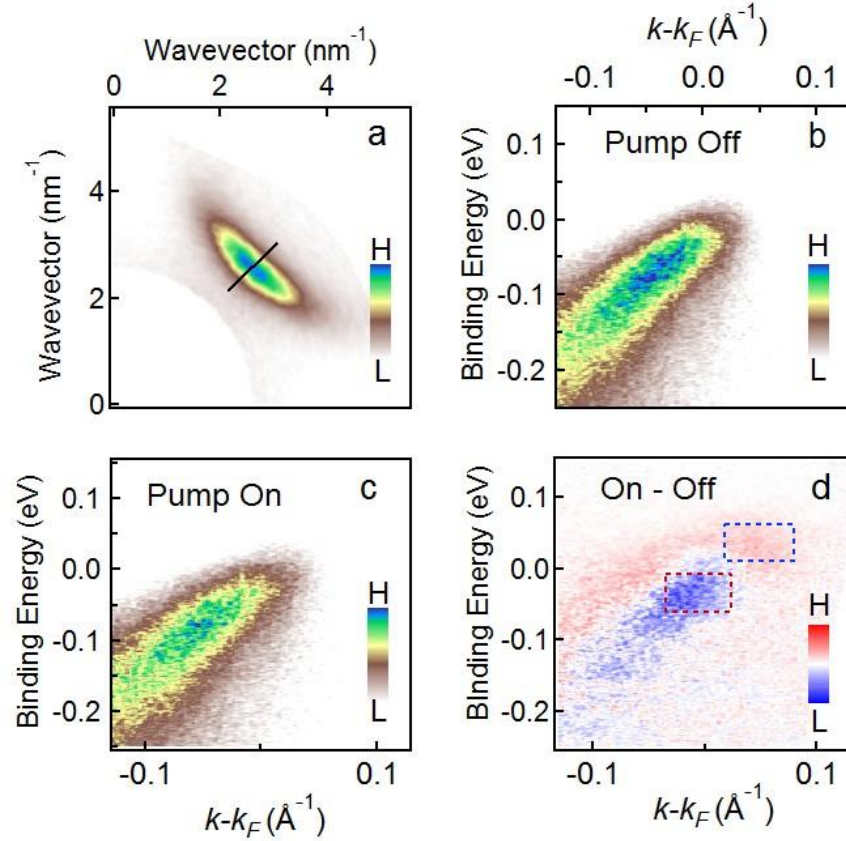


Figure 3.6 The data of this figure have been acquired on optimally doped Bi-2212 ($T_c = 91$ K) at $T = 150$ K. (a) Map of the photoelectron intensity integrated in a small energy interval centered on the Fermi level. The black line visualizes the cut along the nodal direction where we perform tr-ARPES measurements. (b) Photoelectron intensity map showing the quasiparticle dispersion along the nodal direction without the pump pulse. (c) Photoelectron intensity map acquired with pump pulse at delay time of 50 fs. (d) Pump-on minus pump off intensity map at delay time $t = 50$ fs.

Figure 3.6 (b) shows the quasiparticle dispersion of optimally doped Bi-2212 measured at $T = 150$ K in equilibrium condition, i.e without pump irradiation. We show in Fig. 3.6 (c) the photoelectron intensity map acquired at 50 fs after the arrival of a pump-pulse carrying $60 \mu\text{J}/\text{cm}^2$. As shown in figure 3.6 (d), effect of the pump excitation can be enlightened by the subtraction between the photoelectron intensity

map acquired at positive delay and the one acquired without pump pulse. Here two major effects can be resolved: (i) a transfer of spectral weight from below the Fermi level (blue in false colors) to above it (in red) [Sma12] and (ii) a rigid band shift joined to the photoinduced broadening of the quasiparticle peak [Ram14]. Effect (i) can be visible in the energy distribution curves extracted at the Fermi wavevector. The additional shift (ii) generates an area of intensity gain below the Fermi level (red in figure 3.6 (d)). Finally the photoinduced broadening must be extracted from an analysis of the momentum distribution curves. In the following paragraph we will focus on (i), i.e. on the recombination processes that drive the system back to the equilibrium.

3.4.2 Quasiparticle dissipation in the normal phase

Within the duration of the pump pulse, electrons excited above 0.1 eV and holes injected below 0.1 eV have nearly thermalized by means of electron-electron interaction and coupling to spin-fluctuations in proximity of the Fermi level. As a consequence, secondary electron-hole pair excitations are immediately visible in the $[-0.1, 0.1]$ range. In this condition, the thermalization of electrons towards the Fermi level is ruled by electron-electron interaction and it can be strongly enhanced by the emission of paramagnons. As shown from the resonant inelastic X ray scattering (RIXS) data of figure 3.7, the dispersion of paramagnons extends to 250 meV and their density is peaked around 200 meV [Tac11]. Moreover we can infer from the paramagnon linewidth that emission of spin-fluctuations should act on a timescale faster than 20 fs. Recent time resolved optical experiments argued that such process is indeed relevant to the initial relaxation of photoexcited carriers [Dal15]. In any case, the timescale related to paramagnon coupling is too fast in order to be captured by our temporal resolution.

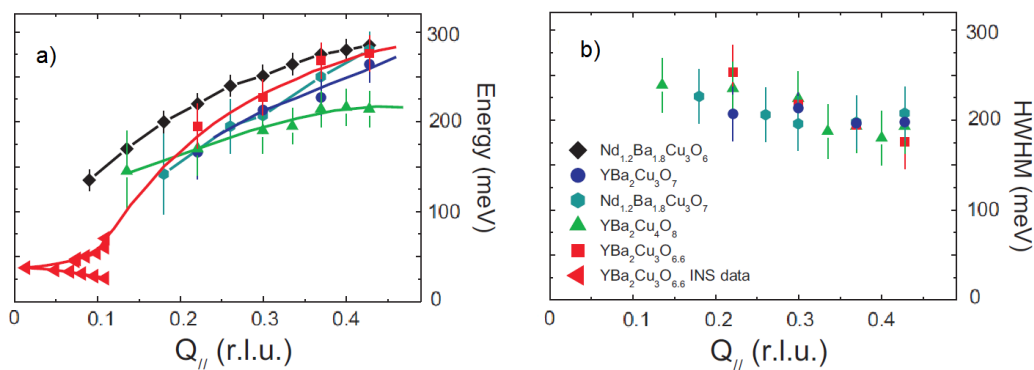


Figure 3.7 (a) Experimental magnon dispersion along 100 direction in antiferromagnetic $\text{Nd}_{1.2}\text{Ba}_{1.8}\text{Cu}_3\text{O}_6$, underdoped $\text{Nd}_{1.2}\text{Ba}_{1.8}\text{Cu}_3\text{O}_7$, $\text{YBa}_2\text{Cu}_3\text{O}_{6.6}$, $\text{YBa}_2\text{Cu}_4\text{O}_8$ and $\text{YBa}_2\text{Cu}_3\text{O}_7$ at $T = 15$ K. Low-frequency INS data recorded along the 100 direction from $(-\pi, -\pi)$ for $\text{YBa}_2\text{Cu}_3\text{O}_{6.6}$ have been added. (b) HWHM of magnetic excitations in $\text{Nd}_{1.2}\text{Ba}_{1.8}\text{Cu}_3\text{O}_7$, $\text{YBa}_2\text{Cu}_3\text{O}_{6.6}$, $\text{YBa}_2\text{Cu}_4\text{O}_8$ and $\text{YBa}_2\text{Cu}_3\text{O}_7$, from Ref. [Dal15].

Instead, the electrons dynamics observed in our experiment is ruled by scattering with lattice modes.

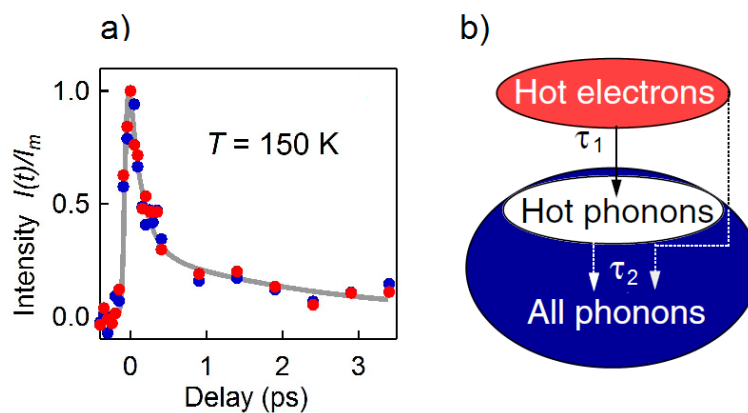


Figure 3.8 (a) Temporal evolution of the photoexcited electrons (red) and holes (blue) acquired with fluence of $60 \mu\text{J}/\text{cm}^2$. The solid line is a bi-exponential fit convoluted with our cross correlation. (b) Sketch of the energy transfer during the relaxation process. Hot electrons generate hot phonons with characteristic time $\tau_1=150$ fs, while hot phonons dissipate their energy on the time scale $\tau_2=2.5$ ps. From Ref. [Per07]

We track the transient dynamics of such excited quasiparticles by integrating the intensity of the differential image in an area just above and just below the Fermi level

(see figure 3.8). Figure 3.8 (a) shows the obtained intensity $I(t)$ of photoexcited electrons (red) and photoexcited holes (blue) normalized to the maximal value I_m . We fit $I(t)/I_m$ by a bi-exponential function $A_1 \exp(-t/\tau_1) + A_2 \exp(-t/\tau_2)$ convoluted with a Gaussian distribution of 80 fs FWHM. In all measured cases the dynamics of photoexcited electrons and photoexcited holes are identical within the errors bars. The relaxation takes place on two distinct timescales: a faster one with a decay time $\tau_1 = 150$ fs and a slower one with $\tau_2 = 2.5$ ps [Per07].

Our interpretation of the observed dynamics is sketched in the diagram of figure 3.8 (b). Ballistic transport of hot electrons out of the surface [Kno98] is neglected because of the quasi-two-dimensional layered structure of Bi-2212. For the phonons we consider two subsets: (i) a limited number of modes, which interact more strongly with the electrons, and (ii) a complementary subset of nearly noninteracting modes. First the electrons transfer energy to the phonons that are more strongly coupled and have higher quantum energy. In the case of BSCCO, these modes are likely the copper-oxygen stretching and buckling modes with typical energy of 40-60 meV. The electronic energy dissipation related to this relaxation channel gives rise to the decay time of 150 fs. Because of their small specific heat, this small subset of the total phonons acquires an effective temperature T_p larger than the lattice temperature T_l . Already after 300 fs, the hot electrons and hot optical phonons reach a common temperature and their dynamics become similar. The electronic cooling can still proceed due to a residual scattering with the cold acoustic modes. Moreover, we expect the hot phonons to dissipate their energy by means of anharmonic decay. The relaxation by anharmonic cooling and scattering with cold phonons takes place with time constant 2.5 ps. After few picoseconds, the sample surface is in local equilibrium while heat diffusion from the surface to the bulk leads to the recovery a uniform temperature within several nanoseconds. In our analysis the parameter A_1 can be viewed as the fraction of electronic energy density dissipated in hot optical phonons whereas $A_2 = 1 - A_1$ is the energy resting in the electrons once the scattering with optical phonons reached detailed balance conditions.

3.4.3 Quasiparticles relaxation at different temperatures across the superconducting phase transition

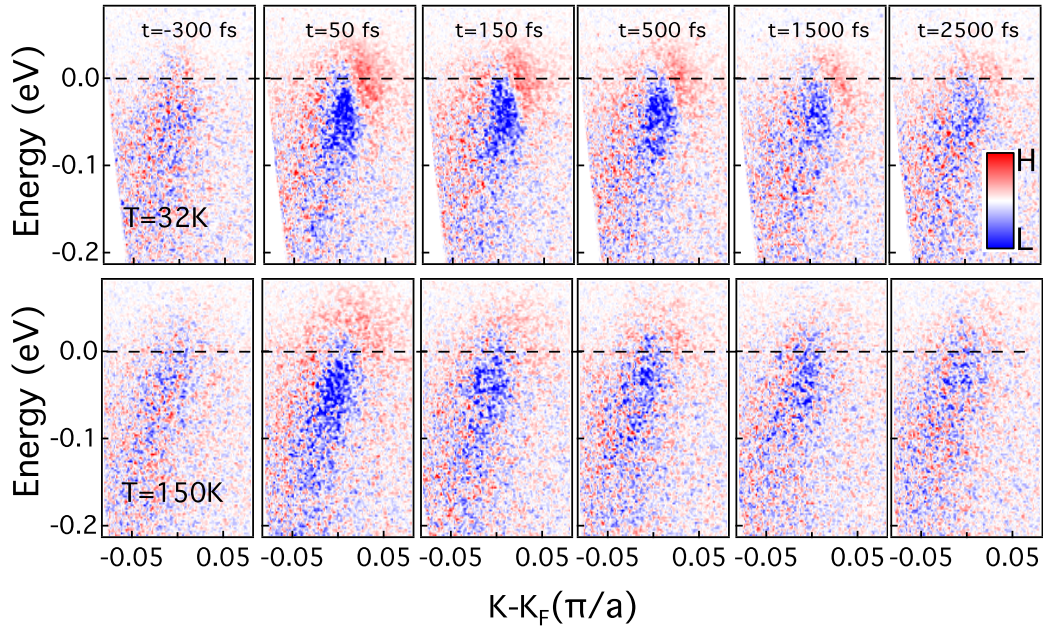


Figure 3.9 Pump-induced photoemission intensity difference as a function of momentum and energy in a red-white-blue color representation at indicated decay time for various temperatures. The red indicates intensity gain and blue indicates intensity loss, reflecting optical excitation of non-thermal electron-hole pairs.

In order to get more insights into the temperature dependent evolution of the nodal quasiparticles distribution, in figure 3.9, we show the intensity difference maps measured at $60\mu\text{J}/\text{cm}^2$ for different pump probe delays t and sample temperature T . Data are shown with identical red-white-blue color. Immediately after the excitation (~ 50 fs), the spectra exhibit a strong reduction of the hole-excitations, along with a marked increase of the electron excitations. Comparing intensity different maps for different temperature, we can see that the maximal transfer of spectral weight is reached at very short probe-pump for each temperature. So the maximum in the nonequilibrium quasiparticles population is reached within the duration of the pump pulse [Zha16]. It is evident from figure 3.9 that the cooling of excited quasiparticles is much faster in the normal phase ($T=150$ K) than in the superconducting one ($T=32$ K). In order to follow the dynamics across the phase transition, the pump probe signal $I(t)$ has been obtained by integrating the photoexcited electrons in the dashed square

above the Fermi level. Similarly to figure 3.8, we verified for each temperature that very similar dynamics is obtained by integrating the hole signal below the Fermi level.

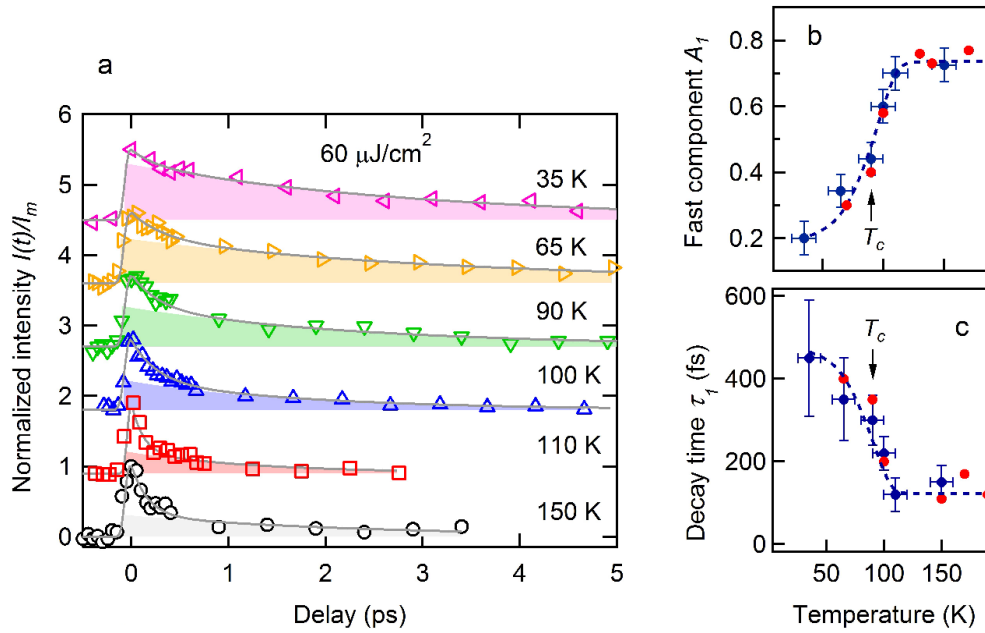


Figure 3.10 (a) The temperature dependence of the quasi-particles dynamics obtained with pumping fluence $60 \mu\text{J}/\text{cm}^2$ on optimally doped Bi-2212 sample ($T_c=91\text{K}$). Solid lines are bi-exponential fits $f(t) = A_1 \exp(-t/\tau_1) + A_2 \exp(-t/\tau_2) + B$. The underneath colored areas stand for the slow component $A_2 \exp(-t/\tau_2)$. The curves have been shifted by an arbitrary offset for better clarity. (b-c) Relative weight of the faster component A_1 and fast decay time τ_1 as a function of temperature. Blue and red marks in panel are two different cleaves while the dashed line is guide to the eye.

Figure 3.10 (a) shows the extracted temporal evolution of the normalized signal $I(t)/I_m$. The bi-exponential fit of $I(t)/I_m$ and the slow component $A_2 \exp(-t/\tau_2)$ are shown by solid line and colored areas, respectively. We observed that the slow decay time does not depend on temperature and it is constant in a confidence interval $\tau_2 = 2.5 \pm 0.5 \text{ ps}$. Notice in figure 3.10 (b) that the weight of the fast component is nearly constant above T_c whereas it drops when T is below the critical temperature. At $T = 35 \text{ K}$ the weight A_1 has almost vanished so that nodal quasiparticles are no longer able to efficiently scatter with optical phonons. This behavior correlates to a weaker dissipation rate. Despite the large error bars, the τ_1 parameter in figure 3.10 (c) is clearly increasing when the system is cooled below the

critical temperature. The trends reported in figure 3.10 (b, c) have been consistently observed on three different cleaves of Bi-2212.

When changing temperature, the maximal intensity I_m scatters randomly around the average value with error bars of 30% as shown in figure 3.11. We ascribe these uncertainties to the movement of sample position during the cooling process. It has not possible to identify any reproducible trend of I_m for $35\text{K} < T < 150\text{K}$ [Zha13]. Anyway, the relative small variations of the maximal pump-probe signal suggest that the initial energy density of excited quasiparticles depends weakly on the sample temperature.

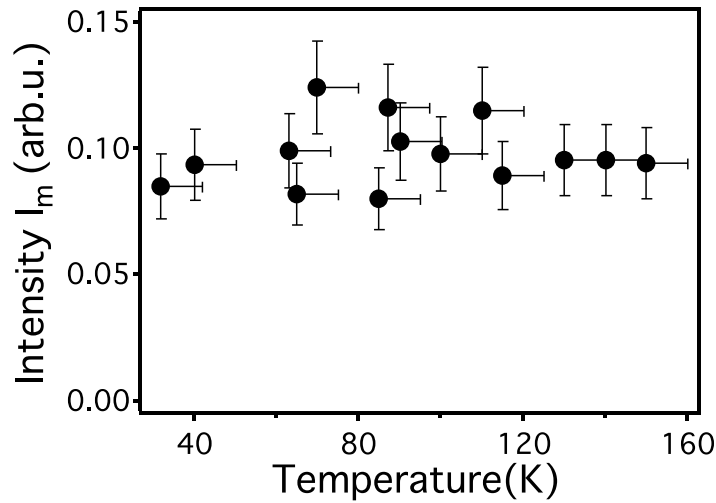


Figure 3.11 Maximal value of the photoinduced signal I_m as a function of temperature.

The data of fig. 3.10 indicate that a remnant Cooper pairing inhibit phonon scattering channels even if the photoexcitation fluence is of $60 \mu\text{J}/\text{cm}^2$. On the other hand, this pump fluence is considerably larger than the minimal value necessary for the complete destruction of superfluid stiffness. As reported in section 3.1, Time resolved THz spectroscopy measurements on optimally doped Bi-2212 [Kai05] have shown that supercurrents are completely suppressed when pumping the sample with 800 nm and an energy density of $F_{phase} = 12 \mu\text{J}/\text{cm}^2$. The time resolved THz experiments [Kai05, Car04, Bey11, Ave01] also indicate that long-range superconductivity is rapidly destroyed and recovers on the picosecond timescale. By a direct comparison with time resolved THz data [Bey11], we can identify a temporal window larger than

1 ps when the material does not hold superfluid density although quasiparticles do not display a strongly inelastic scattering. Note that the experiments Kaindl *et al.* have been performed on thin films and with a different setup. Therefore the actual comparison of the fluence with our measurements is somehow hazardous. Anyway, the present data indicate the intriguing possibility of a fluence regime where Cooper pairs exist but are not phase coherent.

3.4.4 Comparison of quasiparticles relaxation between Bi-2212 and Bi-2201

Another question is if the reduction of quasiparticles dissipation persists to fluences higher than F_{phase} because of the presence of an antinodal pseudo-gap observed by ARPES [Kon11][Vis10]. Recent measurements have showed that the pseudogap arises from the interplay of two distinct mechanisms: the preformed pairing and a competing charge ordering. In optimally doped Bi-2212, the depression of electronic state due to the former may cover a region of 30 K above T_c whereas to the latter can extend up to 200 K. The data in figure 3.10 (b) show a clear reduction of dissipation rate below $1.3 T_c \cong 120$ K, namely at the temperature where the amplitude fluctuation of the superconducting order parameter builds-up. This finding suggests that quasiparticle scattering is especially sensitive to the pairing but less affected by the presence of the competing pseudogap.

In order to confirm this scenario, we decided to investigate optimally doped $\text{Bi}_2\text{Sr}_{2-x}\text{La}_x\text{CuO}_{6+\delta}$ (Bi-2201). The single layer Bi-2201 has $T_c=28\text{K}$ but develops an antinodal pseudo-gap already below 120K [He11][Kon00]. Angle Resolved photoemission measurements compare well with transient optical Kerr rotation, thereby suggesting that the pseudogap is a bulk property of the system. The data acquired by Hashimoto *et al.* (see figure 3.12) show the evolution of the spectral function as a function of temperature. They ascribe the depression of electronic density below 120 K to the presence of a charge order origination from the favorable nesting conditions of the Fermi surface.

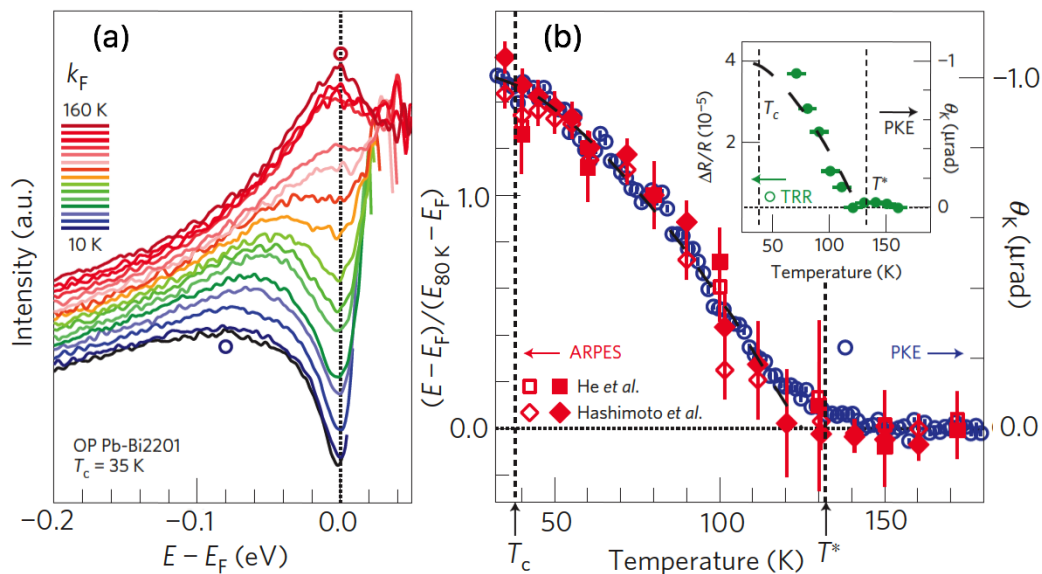


Figure 3.12 (a) Temperature dependence of the ARPES spectra at the Fermi wavevector acquired in the antinodal region of the spectrum. Blue and red circles indicate the intensity maxima of the spectra at 10 K and 160 K, respectively. (b) Temperature dependence of the pseudogap measured by ARPES, in comparison with the Kerr rotation angle measured by the transient optical spectroscopy. From Ref. [Has14]

We have performed time resolved ARPES measurements of Bi2201 along the nodal direction at 35 K and with photoexcitation fluence of $60 \mu\text{J}/\text{cm}^2$. Figure 3.13 shows the differential intensity maps at several pump probe delays. As in the previous case, we obtain the quasiparticle dynamics by integrating the photoelectron signal in an energy window from E_F up to $E_F + 60$ meV. The normalized $I(t)/I_m$ is compared in figure 3.14, to the same quantity measured on the bilayer Bi-2212. Notice that the fast component A_1 is clearly visible in Bi-2201 whereas it is nearly absent Bi-2212. This comparative analysis indicates that quasiparticle dissipation drops because of superconducting correlation (in Bi-2212) but not in relation to a charge ordering (in Bi-2201).

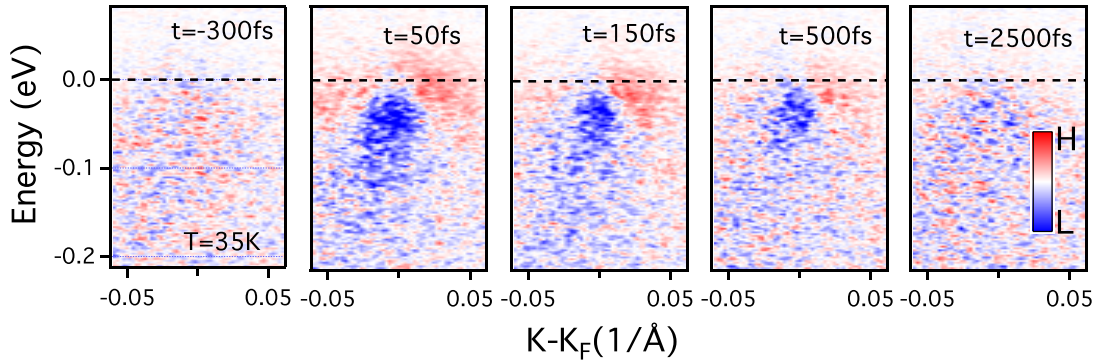


Figure 3.13 Pump-induced photoemission intensity difference acquired in Bi-2201 as a function of momentum and energy in a red-white-blue color representation at indicated decay time for $T=35\text{K}$ with a pump fluence of $60 \mu\text{J}/\text{cm}^2$.

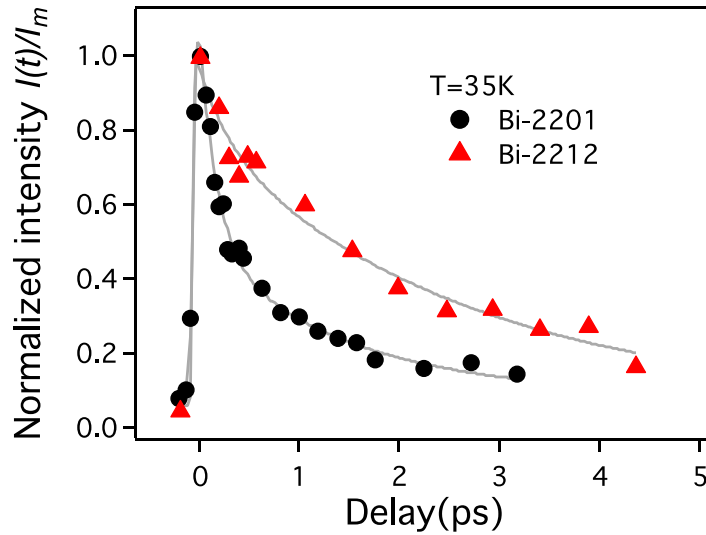


Figure 3.14 Dynamics of photoexcited quasiparticles in Bi-2201 ($T_c = 28 \text{ K}$) (circles) and Bi-2212 ($T_c = 28 \text{ K}$) (Triangles) acquired with a pump fluence of $60 \mu\text{J}/\text{cm}^2$ at a base temperature $T=35\text{K}$. The Solid lines are biexponential fits. The fast component A_1 is small only in the superconducting sample Bi-2212.

3.4.5 Quasiparticles relaxation at different photoexcitation densities

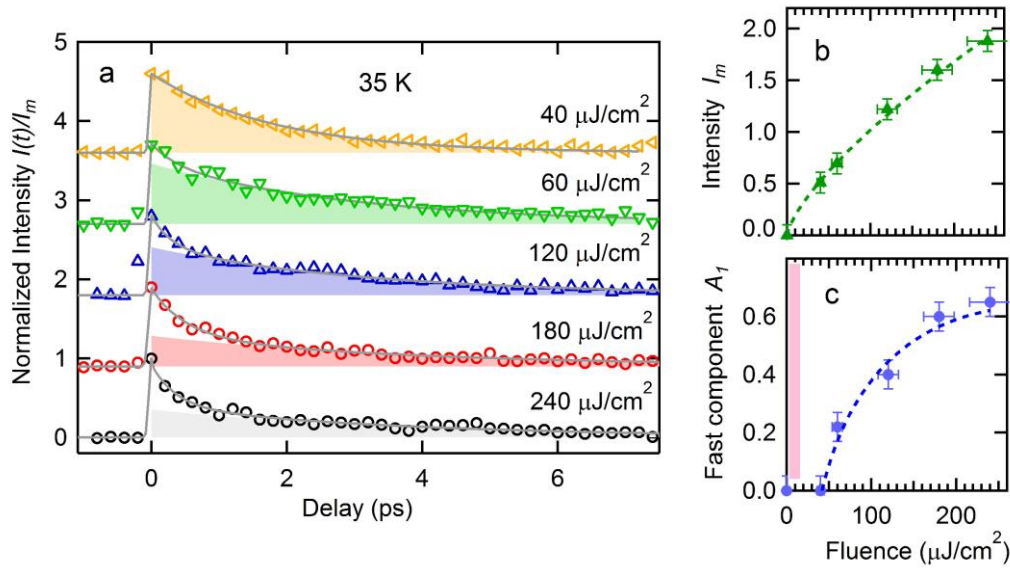


Figure 3.15 (a) The pump fluence dependence of the photoexcited quasi-particles dynamics obtained at 35K on optimally doped Bi-2212 sample ($T_c=91\text{K}$). Solid lines are bi-exponential fits while the underneath colored areas stand for the slow component. The curves have been shifted by an arbitrary offset for better clarity. (b) Maximal value of the photoinduced signal I_m and relative weight of the fast component A_1 as a function of pump fluence. The dashed line is a guide to the eye. (c) Relative weight of the fast component A_1 as a function of pump fluence. The dashed line is a guide to the eye and the filled area is the fluence range where supercurrents monitored by time resolved THz are not totally destroyed by the optical pump pulse.

Next, we set the temperature of the bilayer Bi-2212 to 35 K and we perform temporal scans increasing the pump fluence from 40 up to 240 $\mu\text{J}/\text{cm}^2$. Figure 3.15(a) shows the normalized $I(t)/I_m$ and the bi-exponential fits. In agreement with previous results [Zha13], we show in figure 3.15 (b) that I_m has nearly a linear dependence on fluence. As shown by figure 3.15 (b), the fast scattering component A_1 is not detectable for pump fluence of $F_{pair} = 40\mu\text{J}/\text{cm}^2$ and grows up non-linearly at higher photoexcitation densities. An indication of this threshold has been already reported by R.Cortés *et al.* [Cor11], who have shown that the fast quasiparticle relaxation develops for pumping fluences in the range 30 – 130 $\mu\text{J}/\text{cm}^2$. Our data are also in agreement with the onset of the rapid dissipation channel observed at 70 $\mu\text{J}/\text{cm}^2$, in

transient reflectivity experiments [Gia09]. By comparing the curve in figure 3.15 (b) with the THz measurements of M. A. Carnahan [Car04], we could identify a fluence regime between $F_{\text{phase}} = 12 \pm 3 \mu\text{J}/\text{cm}^2$ and $F_{\text{pair}} = 40 \pm 5 \mu\text{J}/\text{cm}^2$ when the phase coherence is lost but the fast dissipation channel is blocked. In the following we discuss this possible existence of such fluence window and its implications to the physics of cuprates. It is reasonable that an electron pairing over a distance larger than the mean free path scale l would inhibit the quasiparticles scattering. Therefore, the quasiparticle relaxation can be an effective probe of superconducting correlations with short range, namely of the presence of Cooper pairs (even incoherent ones). We will confirm the presence of pairing up to $40 \pm 5 \mu\text{J}/\text{cm}^2$ in the following chapter, where we will see that F_{pair} coincides with a full collapse of the superconducting gap. The possibility that $F_{\text{pair}} > F_{\text{phase}}$ is quite natural in high temperature superconductors. Indeed even in equilibrium condition incoherent pairs can be detected few tens of kelvin above the superconducting transition temperature. Nonetheless, out of equilibrium the underlying physical phenomena will be more complex. Not much is known about the excited state generated upon irradiation with 1.5 eV. Clearly, the primary photoexcited electrons trigger a cascade of secondary processes that dephase and break Cooper pairs. It may happen that long wavelength amplitude fluctuations are much slower than short wavelengths ones. Such long wavelength fluctuations can be very effective in breaking superconductivity in equilibrium whereas they could be still "frozen" in the transient state. Therefore, the photoexcited state at fluence $F_{\text{phase}} < F < F_{\text{pair}}$ could be dominated by short-range amplitude fluctuations and related phase fluctuations. On the long timescale we may expect the formation of vortex-antivortex pairs [Li_13] whereas a coarsening phenomenon characterizes the early delays. Indeed, as noticed by Giannetti *et al.* [Gia09], the coalescence dynamics of transient reflectivity suggests the tendency of phase separation between the normal and superconducting phase. In this context, it is important to recall that a model leading to non-equilibrium first order phase transition has been discussed in the steady state by C. S. Owen and D. J. Scalapino [Owe72]. Similar conclusions may concern also photoinduced phase transitions of conventional superconductors [Mat12], Charge Density Waves (CDW) materials [Lee12, Hub14] or magnetic ordering [Li_13]. Hopefully, the theoretical advances in non-equilibrium condensates [Szy06] and dynamical phase transitions [Can14] may provide enlightening predictions in the

near future. Moreover, the combined time resolved ARPES and time resolved THz measurements on a same sample and in the same experimental conditions would be mandatory to assess the correct size of the $[F_{\text{phase}}, F_{\text{pair}}]$ region.

Next, we intend to briefly discuss the dynamics of quasiparticles in the high fluence regime. Figure 3.15 shows that the relaxation of hot electrons becomes qualitatively different when pumping the sample with pulses more intense than F_{pair} . We report in figure 3.16 (a), a delay scan of $I(t)/I_m$ acquired with smaller temporal steps, pump fluence of $240 \mu\text{J}/\text{cm}^2$ and temperature of $T = 35 \text{ K}$. By fitting the data, we find a fast decay time $\tau_1 = 500 \text{ fs}$, therefore consistent with the low temperature limit of figure 3.10 (c). The slower timescale $\tau_2 = 2.5 \text{ ps}$ does not depend appreciably on the pump fluence. These results are consistent with the data first reported by Cortes *et al.* [Cor11] and Ref. [Pio15]. In order to explain the double exponential relaxation, Smallwood *et al.* proposed that a dynamical gap opening during the quasiparticle relaxation process effect recovery rate of photoexcited quasiparticles [Sma16]. This conjecture is plausible and can qualitatively fit to our results. In this case, the reforming pairing not only hinders quasiparticle dissipation but also act as a heat bath for nodal QPs. The energy released by Cooper Pairs formation can be transferred effectively to QPs, drastically reducing their cooling time. The model proposed by Smallwood *et al.* captures this physics but it is presumably oversimplified. In particular, the rate equations in Ref. [Sma16] predict that QPs follow an evolution similar to the one of the normal phase until the effective temperature of the electrons is above a threshold value. In contrast, the comparison between Fig. 3.16 (b) and 3.16 (a) indicate that the initial cooling of QPs is much faster if $T > T_c$ than if $T < T_c$ and the sample is strongly photoexcited. This finding defies any description of the observed dynamics in terms of simple effective parameters and reveals an inherent complexity of the photoexcited state. Possibly advanced many-body description of the non-equilibrium state can be helpful to shed light on this issue [Ram16].

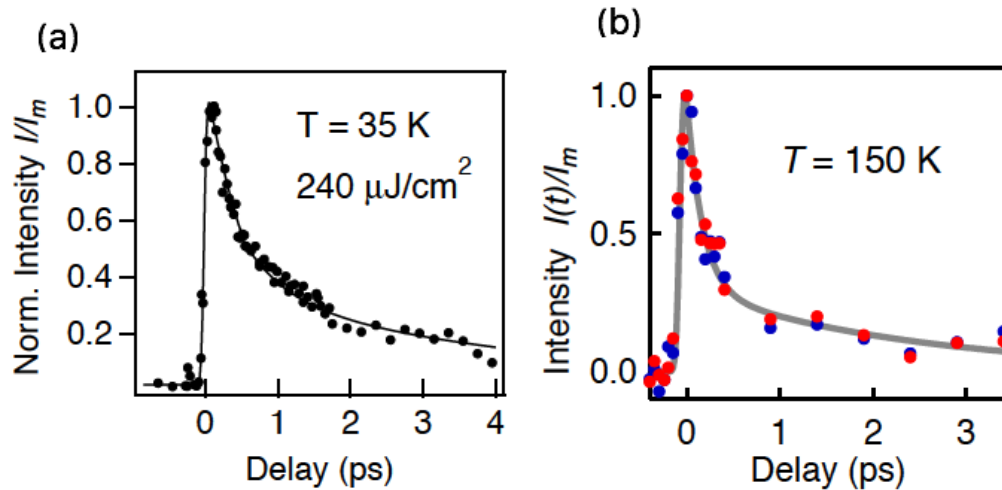


Figure 3.16 Dynamics of photoexcited quasiparticles acquired on optimally doped Bi-2212 ($T_c = 91$ K) in (a) at $T = 35$ K and pumping fluence $240 \mu\text{J}/\text{cm}^2$, and in (b) at $T = 150$ K and pumping fluence $60 \mu\text{J}/\text{cm}^2$ in (b).

3.5 Pump-induced band shift and broadening in $\text{Bi}_2\text{Sr}_2\text{CaCu}_2\text{O}_{8+\delta}$ at high fluence

3.5.1 Experimental reports of transient shifts and quasiparticles broadening

As stated in section 3.4, the photoexcitation induce other effects besides an excited distribution of quasiparticles. Just after photoexcitation, the electronic dispersion display quite drastic changes. These effects have been investigated by several authors.

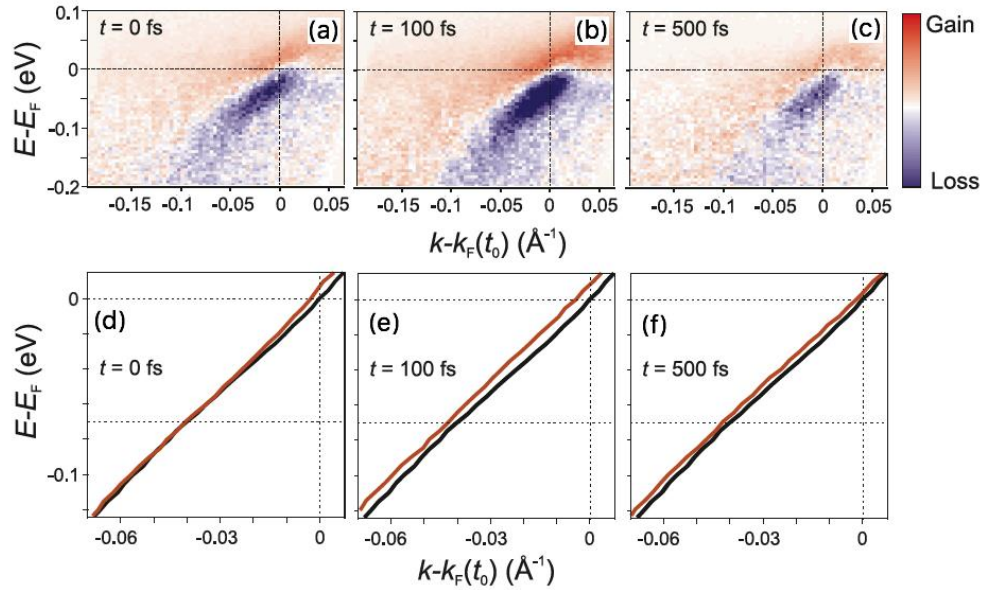


Figure 3.17 (a)–(c) Laser-pump-induced photoemission intensity difference $I(t) - I(t_0)$ as a function of momentum and energy in a blue-white-red false color representation at indicated delay times. (d)–(f) show the respective dispersions $E(k)$ determined from MDC maxima in red. In black, the dispersion before optical excitation at t_0 is shown for comparison. Dotted lines through E_F , k_F , and $E - E_F = -70$ meV are guides to the eye. From Ref. [Ram14]

We show in figure 3.17, the time- and angle-resolved photoemission on an optimally doped $\text{Bi}_2\text{Sr}_2\text{CaCu}_2\text{O}_{8+\delta}$ cuprate performed by Rameau *et al.* [Ram14]. As show in figure (a-h), they reported a time-dependent rigid shift in the electronic band towards negative k including a change in k_F that they ascribe to an effective photodoping due to particle-hole asymmetry. Rameau *et al.* analyzed the changes at different time delays and estimated the corresponding changes in hole doping δx by modeling the Fermi surface of cuprates following the Yang-Rice-Zhang ansatz [Yan06]. They found the maximum shift in k_F and δx occurs at a finite time delay of 50–100 fs, indicating that secondary electronic excitations, to which initial excitations decay [Nes98], induce the k_F change. A similar quasiparticle dispersion shift can be also found in the work of ref [Mil15]. However the Miller *et al.* dismiss the original idea of the photodoping whereas they interpret the band shift as a uniform change in the energy of all photoemitted electrons due to the pump induced change in the potential energy barrier at the surface of the sample. Moreover they arguably assume that a photoinduced change of chemical potential can also contribute to an overall band shift.

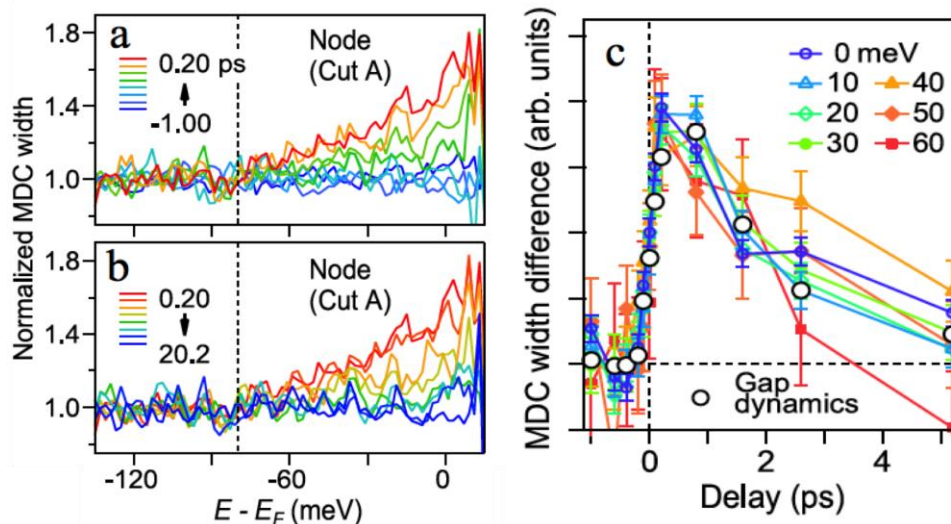


Figure 3.18 (a) and (b) Spectra of MDC width of the nodal cut normalized to those before pumping. Vertical dashed lines indicate the energy above which pump-induced variations become pronounced. (c) Pump-induced variations in the MDC width at various energies. The curves are normalized to the area around 0 ps. The line profile representing the gap dynamics is also overlaid. From Ref. [Ish15]

Afterwards, Ishida *et al.* reported in a recent work that photoexcitation also reduces the coherence of the quasiparticles [Ish15]. As shown in figure 3.18 (a) and (b), the width of Momentum Distribution Curves (MDCs) acquired along the nodal direction increases upon optical pumping. This effect is strongest for MDCs extracted at binding energy lower than the one of the kink energy. A detailed analysis of the transient changes of the nodal MDC width at energies > -70 meV [see figure 3.18 (c)], revealed that the width broadening matches well with the dynamics of the near nodal gap. This process indicates the crossover from cold quasiparticles dressed with virtual boson to hotter quasiparticles that can emit and absorb collective modes.

3.5.2 Photoinduced changes of time resolved ARPES maps

In the following we are going to analyze these effects in detail.

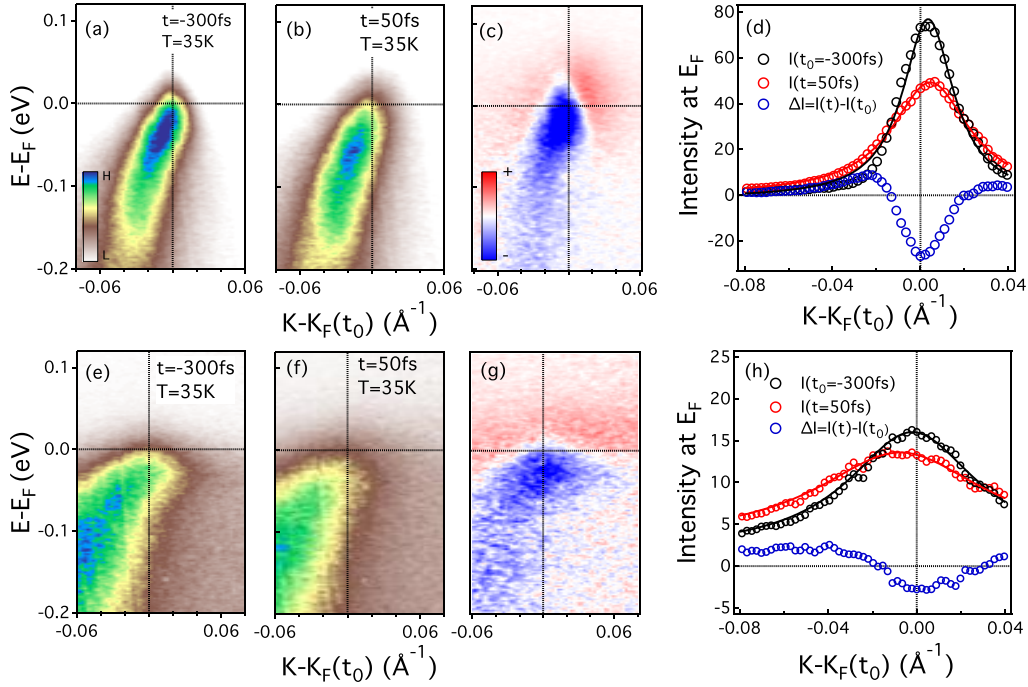


Figure 3.19 ARPES energy momentum dispersions before and after pumping for nodal ($\phi = 45^\circ$) and off-nodal ($\phi = 60^\circ$) cut of k-space. The incident pump fluence was $35 \mu\text{J}/\text{cm}^2$. (a) Equilibrium ($t = -300$ fs) (b) transient ($t = 50$ fs) energy momentum maps for the nodal state. Data are shown with identical color scales. (c) Subtraction between (a) and (b), blue indicates intensity loss and red intensity gained. (d) The momentum-dependent intensity at E_F integrated within $\pm 10 \text{ meV}$ before and during optical excitation as well as the respective differences. Solid black lines are Lorentzian fits. (e-h) same as (a to d) but for a gapped (off-nodal) momentum cut.

Figure 3.19 show the observed photoelectron intensity maps along the nodal direction (a)-(d) and off-nodal direction (e)-(f) at 35K with $35 \mu\text{J}/\text{cm}^2$. Thanks to the pronounced intensity changes in a panel (a)-(b) and (e)-(f), two important effects can be observed: a rigid shift in the electron band and a photoinduced broadening of the quasiparticle peak. The spectral weight redistribution driven by the pump pulse excitation is depicted in panel (c) and (g), where intensity difference color maps show that spectral depletion occurs predominantly in the energy of the coherent quasiparticles at energies between 70 meV kink and E_F . Since the quasiparticle dispersion provides a relation between binding energy and wavevector, it is formally equivalent to describe the rigid shift as a photoinduced change of peak energy ΔE or as a change of MDC first momentum $\hbar\Delta k = \Delta p = \Delta E/v_F$. Here v_F is the band

velocity of the quasiparticle and it has a value of $1.5 \text{ eV} \cdot \text{\AA}$ in the nodal direction of Bi-2212. Practically, the rigid shift if is best visualized by extracting Momentum Distribution Curves (MDC) and estimating the photoinduced change Δk on the curves. Figure 3.19 (d) and (f) show the intensity at E_F acquired along the nodal direction before and just after pumping. The data indicate the occurrence of a shift Δk roughly 2 pm^{-1} and comes together with a photoinduced broadening of the momentum distribution. As shown by figure 3.10 (e) and (f), the effect is qualitatively similar also in the case of a quasiparticle dispersing out of nodal directions. Nonetheless, in the latter case, further complications due to spectral weight redistribution within the superconducting gap may affect the measurement.

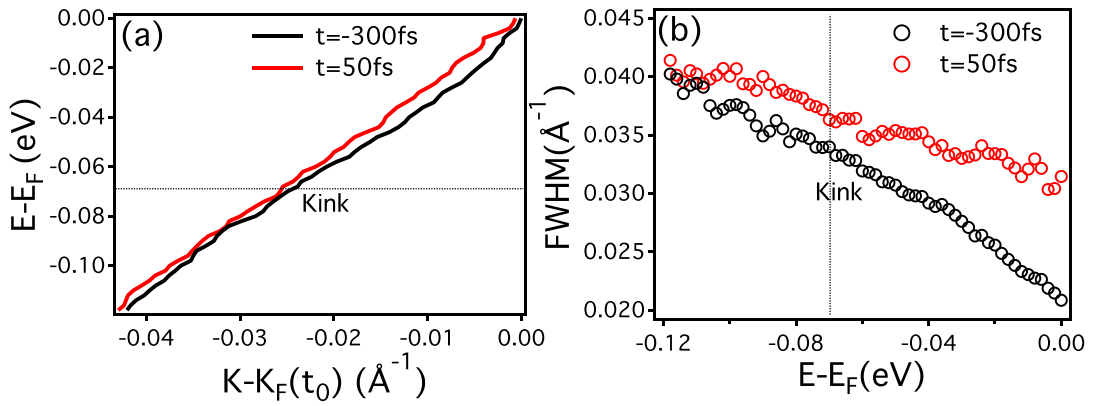


Figure 3.20 (a) Energy momentum dispersions $E(k)$ determined from MDC maxima for $35 \mu\text{J}/\text{cm}^2$ fluence at $T=35\text{K}$, before $t = -300 \text{ fs}$ (in black) and during optical excitation and $t = 50 \text{ fs}$ (in red) at nodal ($\phi = 40^\circ$). The MDC widths as a function of binding energy are shown in panel (b) for $t = -300 \text{ fs}$ (black circles) and $t = 50 \text{ fs}$ (red circles).

In order to highlight the subtle changes in the nodal cut, we fit MDCs at different delays. Figure 3.20 (a), provides the MDC peak positions while figure 3.20 (b) shows the respective MDC widths. Black lines are obtained from the equilibrium state while the red bands are obtained from the transient state (with pump on) at positive time delay. In the equilibrium state before pump excitation (black solid), we can see the dispersion in vicinity of the Fermi level deviates from the linear dispersion predicted by band structure. This effect is due to the coupling of the quasiparticle to collective modes and develops a 'kink' around $E - E_F = -70 \text{ meV}$. Within this energy distance

from the Fermi level, the QP acquires a higher coherence and result in sharper momentum distribution curves. Notice in the dispersion extracted at pump-probe delay of -300 fs that the dispersion holds an artificial upturn for binding energies lower than 20 meV. We ascribe this systematic artifact to the combined effect of the Fermi distribution with a finite energy and wavevector resolution. Consistently with the data of figure 3.19, the dispersion displays a clear shift to higher energy upon optical pumping. Figure 3.20(b) shows that the MDC width is larger in the photoexcited state. This effect is larger for $|E-E_F| < 70$ meV, namely in the spectral region where the initial coherence of the quasiparticles is larger.

3.5.3 Pump-induced band shift

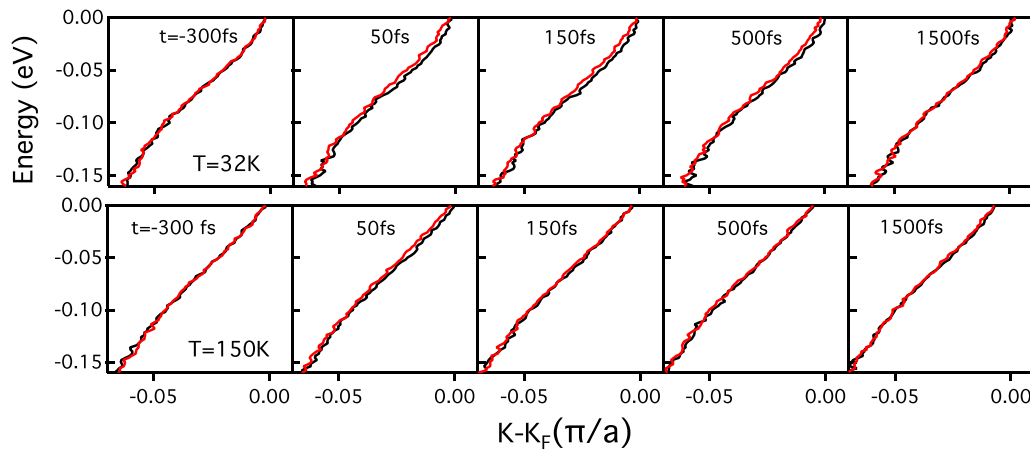


Figure 3.21 Respective dispersion $E(k)$ determined from the Momentum Distribution Curve (MDC) without (black) and with (red) pump excitation. The upper and lower panels correspond to the temperatures below and above T_c .

In figure 3.21, we summarized the temporal evolution and temperature dependence of $E(k)$ dispersions, which is determined by fitting MDCs at different delays. As in figure 3.21, we show the dispersion extracted in equilibrium (pump off) together with the one of the photoexcited state (pump on). The rigid shift reaches the maximal value just after pumping and recovers at later delays. Such recovery rate changes with the temperatures, being faster at higher temperature $T > T_c$ than at low temperature $T < T_c$. As we can see from figure 3.21, the dispersion acquired at 500 fs already coincides with the equilibrium one if the temperature is $T=150$ K, while it has not yet recovered for $T = 32$ K.

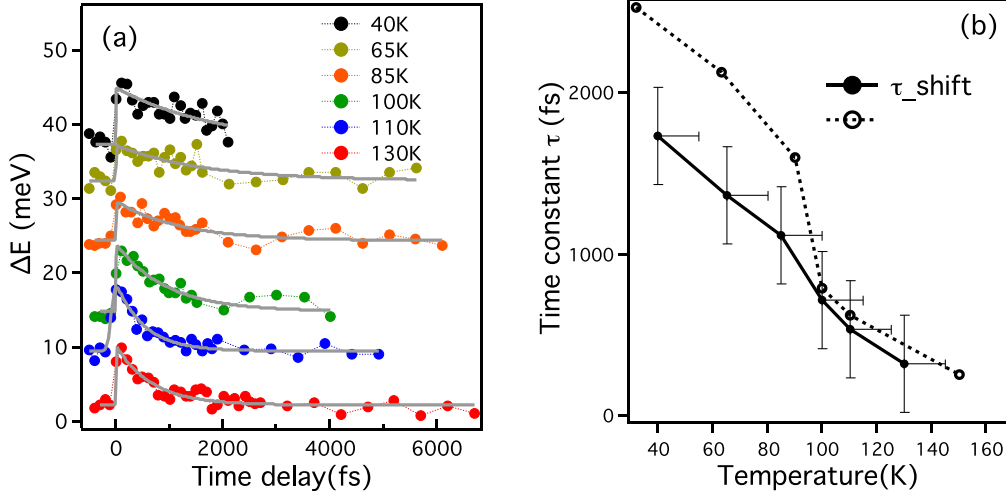


Figure 3.22 (a) Time-dependent pump-induced energy shift integrated over an interval energy window of 120meV below the Fermi level for various temperature. For better clarity, we applied a vertical offset to data acquired at different temperature. (b) The corresponding relaxation time constant τ are shown as a function of temperature (filled circle). The empty circle is the relaxation times obtained from a different cleave of the sample.

In order to investigate the dynamic and temperature dependent of this pump-induced band shift, we integrate the energy shift over an energy range of 120 meV below E_F , which captures the observed difference on the band dispersion between before and after pumping. In figure 3.22 (a), we show the dynamic of the pump-induced band shift for various temperatures. The recovery rate of the band shift τ is obtained by fitting the experimental data with a single exponential fit $\Delta E = A \exp(-t/\tau)$ convoluted with a gaussian. The resulting curves are shown on top of the measured ΔE in figure 3.22 (b). The comparison between figure 3.22 and figure 3.10 indicate that the recovery rate τ of the pump-induced band shift and the cooling dynamics of hot quasiparticles display a similar trend. In contrast to Ref. [Ram14], we do not think that photoexcitation can induce a photodoping of Bi-2212. An obvious reason is that optical excitations are neutrals and cannot change the filling of a metallic system with a single conduction band. Since electrons and holes of Bi-2212 thermalize on the timescale of 100 fs in the single conduction band, the fixed filling should be guaranteed by charge neutrality. In principle, it is still possible that quasiparticles change their dispersion because of hot phonons generation and modified electron-phonon coupling. However, a simpler phenomenon may also play an important role.

Upon photoexcitation, the electrons photoexcited at the surface acquire a large effective temperature T_e whereas the ones in the bulk are at ambient temperature T_l . As a consequence of this temperature gradient, the surface will experience an electromotive potential $\Delta V = -S(T_e - T_l)$, where S is the Seebeck coefficient of the material. Since the conducting carriers of Bi-2212 are hole like, the Seebeck coefficient is positive and the surface acquires a transient negative potential. Such surface potential can shift the electronic spectra by a quantity $\Delta E = -e\Delta V = eS(T_e - T_l)$. According to the reported value $S/T = 0.1 \mu\text{V}/\text{K}^2$, a shift of 10 meV would require hot electrons with an effective temperature of roughly 300 K. This value could be reasonably attained with the pumping fluence of $60 \mu\text{J}/\text{cm}^2$ that has been employed in our experiment. We conclude that the thermoelectric effect may provide an important contribution to the observed energy shift. On the other hand, such effect does not account for the whole set of our experimental data.

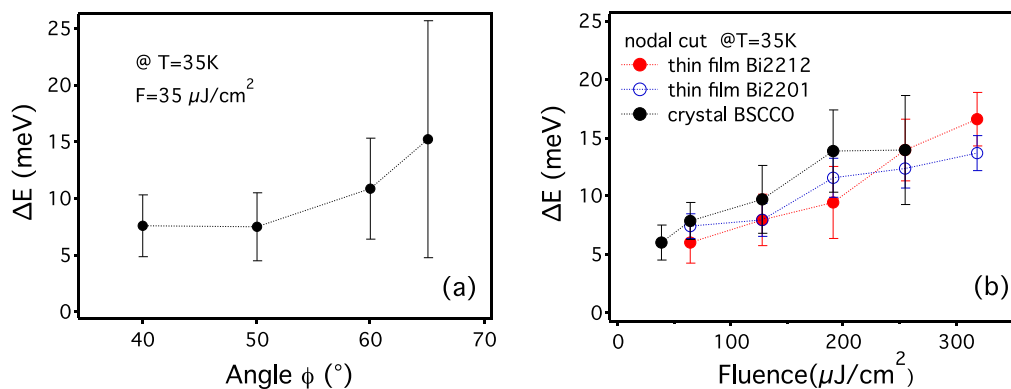


Figure 3.23 (a) Initial energy shift ΔE at pump probe delay of 50 fs acquired at different azimuthal angles. (b) Pump fluence dependence of initial momentum shift ΔE along the nodal direction for different samples.

We show in figure 3.23 (a) the pump-induced energy shift ΔE acquired just after photoexcitation as a function of the azimuthal angle. Apparently ΔE depends on ϕ and increases in the antinodal region of the reciprocal space. Moreover, figure 3.23 (b) the energy shift increase linearly with fluence. Notice that comparable shift magnitude have been clearly observed in all investigated samples: Bi-2212 single crystal, thin film Bi-2212 and film Bi-2201. These data may question the simple interpretation based on thermoelectric effect. The latter should generate a shift that does not depend on azimuth. Moreover the temperature gradient of the electrons

should be smaller in thin films than in the bulk sample. In the specific case, we employed thin films of roughly 100 nm. Since this thickness is comparable to the penetration depth of the pump pulse, the shift observed in thin films should be only 20%-30% smaller than one of bulk samples. Finally due to the large error bars of our measurements, a conclusive statement on this issue is currently not possible and more investigations will be needed.

3.5.4 Pump-induced band broadening

Next we investigate the pump induced broadening of the quasiparticle peak. In figure 3.24 (a), we show the pump-induced changes in the MDC broadening for a nodal cut as a function of binding energy at $T = 40$ K and different delay times. As reported in figure 3.24 (b) such broadening seems almost independent on the azimuthal angle. Note, that measurable variations of the MDC width could be observed only in the energy range between the kink energy -70meV and the chemical potential E_F . These variations are similar to those reported in Ref. [Kam01], and can be easily explained by photoinduced increase of quasiparticle scattering rate. We recall that quasiparticle display high coherence only in proximity of the Fermi level. In such low energy range, the boson polarization coherently dresses the renormalized quasiparticle but does not affect the quasiparticle lifetime. Upon photoexcitation, the electrons acquire a high effective temperature and the quasiparticle lifetime drops suddenly. Accordingly, we show in figure 3.24 (c) that the MDC width increases just after the arriving of the pump pulse, showing a recovery behavior similar to the one of the quasiparticles cooling.

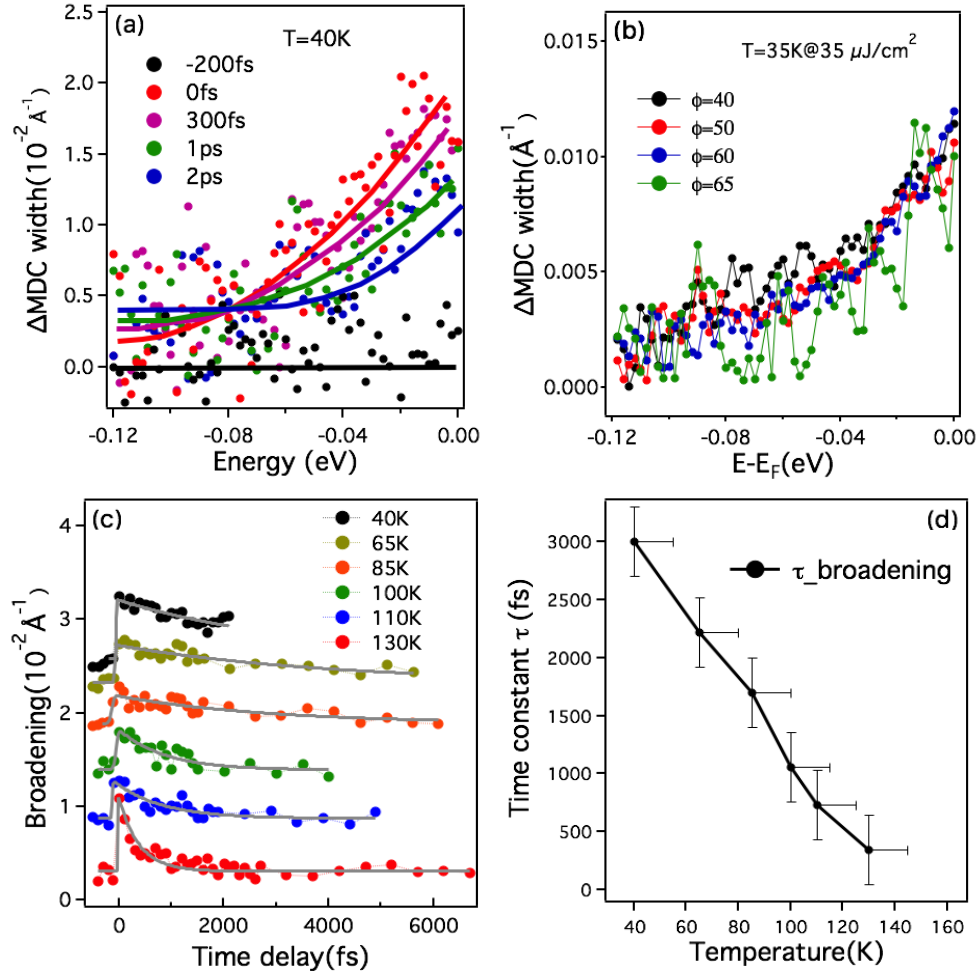


Figure 3.24 Pump-induced spectral broadening. (a) Pump-induced variations in MDC width at different time delays, data are normalized to those before pumping for 40K. (b) Momentum dependence of initial bandwidth shift. (c) Time-dependent pump-induced band broadening integrated over an energy window of $E-E_F > -120$ meV for various temperature. Data at different temperatures have been displayed by vertically offset for better clarity. (d) The corresponding relaxation time constant τ are shown as a function of temperature.

The dynamic of the pump-induced band broadening has been fit by an exponential decay. The corresponding time constant τ is plotted as a function of temperature in figure 3.24 (d). Similarly to the quasiparticle cooling and the band shift, the recovery rate decreases by lowering the temperature below the transition value.

3.6 Conclusions

We report on the study, using Tr-ARPES, of the non-equilibrium physics of optimally doped Bi-2212 and Bi-2201. We show that the relaxation rate due to inelastic scattering of photoexcited nodal quasiparticles depends both on the sample temperature and on the fluence of the pump laser, increasing when temperature is raised above T_c or when the fluence goes over a certain threshold. Interestingly, the experiments show that the drop in scattering rate below T_c subsists even for pump fluence much larger than the ones needed to suppress long range superconductivity. This behavior of the quasiparticle scattering is interpreted in terms of superconducting correlations extending over a length scale comparable to the inelastic mean-free path. Below T_c , for pump fluences where long-range superconductivity has been suppressed, the electrons would then enter a regime without phase coherence but finite pairing amplitude. The data in also show that such pairing amplitude vanishes near T_c , and therefore does not seem to be related to the pseudogap-which persist up to higher temperatures. We also show that an infrared pump pulse of sufficiently high fluence induces a time dependent shift of the quasiparticle band and a time-dependent quasiparticle broadening. Contrary to previous studies that assigned such observations to photo-doping, we interpreting both effects in terms of a transient voltage drop at the sample surface (relative to the bulk) induced, through the thermoelectric (seebeck) effect, but the transient elevated temperature difference between the photoexcited electrons at the surface and the cold electrons in the bulk.

Chapter 4

Time- and momentum-resolved gap dynamics in $\text{Bi}_2\text{Sr}_2\text{CaCu}_2\text{O}_{8+\delta}$

4.1 Introduction

The spectral energy gap is an important signature that defines states of quantum matter: insulator, density waves and superconductors have very different gap structures. The equilibrium gap and pseudogap properties of cuprates have been characterized by the ARPES, which is a powerful tool to characterize spectral gaps. It has been established that the gap [Has14][Kan07] in high transition temperature cuprates is not isotropic but has an anisotropic d-wave structure. Moreover ARPES experiments on underdoped samples revealed that a remnant depletion of spectral density can be observed at the chemical potential, in the antinodal region of reciprocal space. The pseudogap observed in cuprates is a complex phenomenon [Loe96] [Din96] [Nor98] [Mar96], which includes at least three different ‘intertwined orders’: spin and charge density waves [Hay92] [Che93] [Tra94] [Tra95] [Fuj02] [Kiv03] [Tra04] and preformed pairs [Lok01] [Lar05], which appear in different parts of the phase diagram. The nature of this poorly understood phenomenon and its relationship with superconductivity remains a matter of debate. Adding femtosecond time resolution to ARPES provides the way to disclosing physical effects not observed by equilibrium spectroscopies and extracting information related to equilibrium states of matter. In cuprates, the direct observation of the response of the quasiparticles along the d-wave

nodal allows for the investigation of electrons-boson couplings [Per07][Yan15][Zha16] [Ram16][Zha16], self-energy correlations due to the kink bosons [Gra11] [Sma12] [Zha14] [Ish16], photo doping [Ram14], chemical potential [Tri15], and cooper pairs coherence [Pio15]. Studies over a wide k region showed carriers and gap dynamics as a function of pumping fluence and equilibrium temperature [Cor11][Sma12][Sma14].

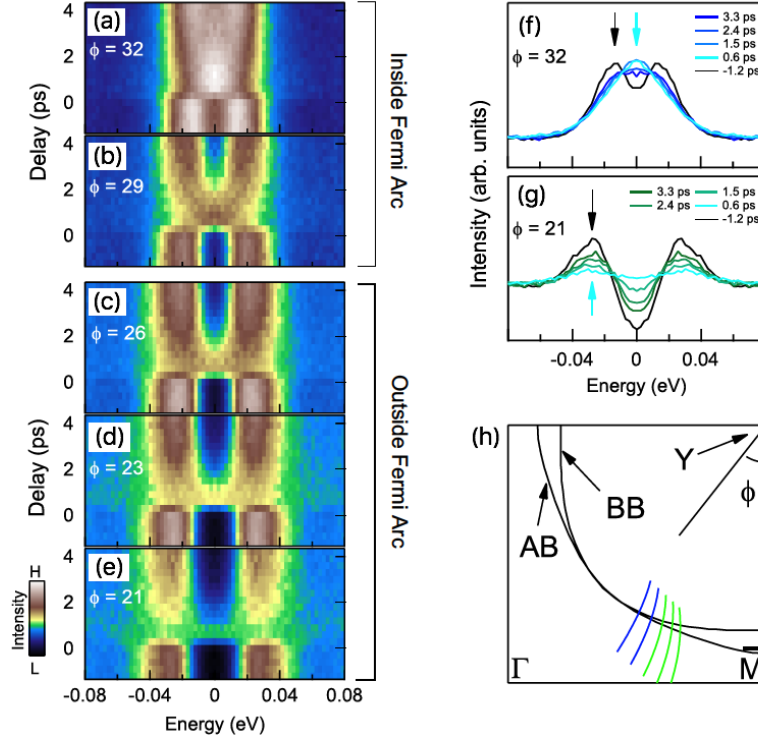


Figure 4.1 Momentum dependence of the transient superconducting gap for a pump fluence of $24 \mu\text{J}/\text{cm}^2$ and $T \ll T_c$, as analyzed using symmetrized energy distribution curves (EDCs). (a)–(e) False-color intensity plots of symmetrized EDC spectral weight versus energy and delay time. (f)–(g) EDCs at selected times for a representative near-nodal (g) and far-off-nodal (h) momentum cut. The black and cyan arrows highlight respective peak positions at $t = -1.2$ ps and $t = 0.6$ ps. Adapted from Ref. [Sma14]

Smallwood *et al.* performed time-resolved ARPES measurements on nearly optimally doped Bi-2212 ($T_c = 91$ K) to measure gap dynamics following the destruction of superconductivity by an ultrafast laser pulse. The author photoexcited the sample with a near-infrared pulse, and probed it with an ultraviolet pulse. The nonequilibrium dynamics reveal that the superconducting gap near to the nodal region shrinks upon photoexcitation and eventually collapses above a critical pumping fluence. According

to the data in figure 4.1(a), the near nodal gap (inside the normal-state Fermi arc) has fully collapsed for a pump fluence beyond $F \approx 15 \mu\text{J}/\text{cm}^2$, with a response time of 300–600 fs (see figure 4.1(f)). They found a significant dependence of such critical fluence value on the direction at which the superconducting gap is observed. Figure 4.1(d), indicates that the off nodal gap (outside the Fermi arc) remains open to at least $24 \mu\text{J}/\text{cm}^2$, with recovery timescales on the order of picoseconds. The authors argued that the response of the off nodal gap is more aptly characterized as filling in rather than closing, due to the competition of superconductivity and pseudogap ordering. However, they could not explore the behavior at higher pumping fluence, when the off nodal gap is expected to completely close.

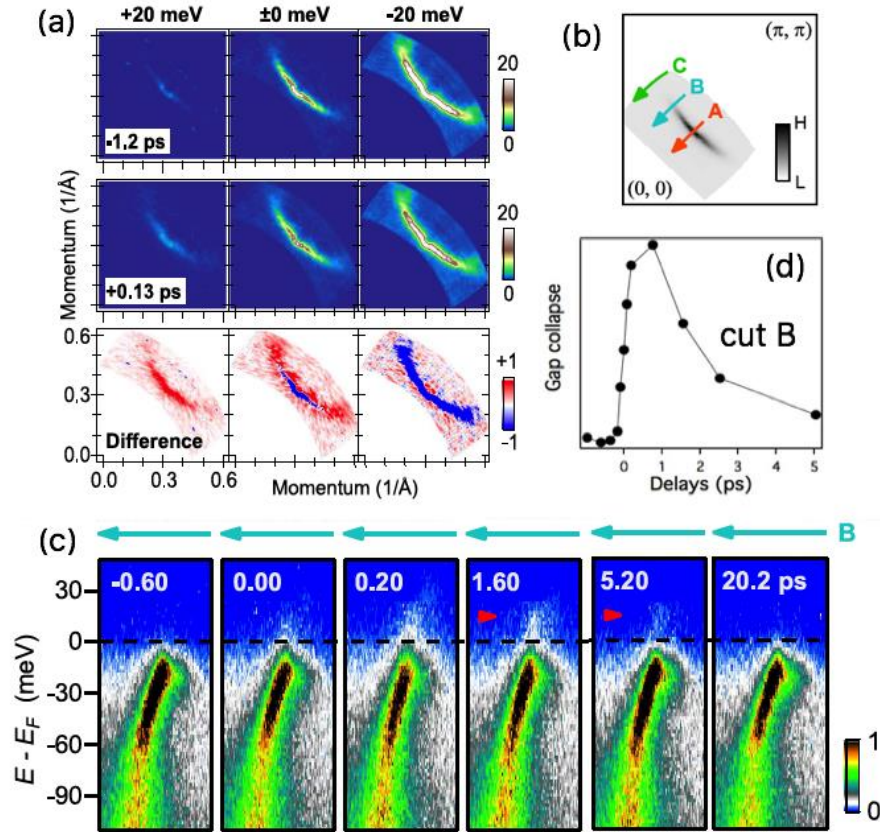


Figure 4.2 Pump induced Fermi arc and Collapse-and-recovery of the superconducting gap of Bi-2212. (a) Spectral weight maps at various energies (integral window of ± 5 meV) recorded at $t = -1.2$ ps (top) and at 0.13 ps (middle) at 10 K. The bottom row shows the maps of difference between those recorded at 0.13 and -1.2 ps. (b) Remnant Fermi surface represented by the spectral weight at $E_F \pm 5$ meV mapped in k -space. (c) TrARPES images recorded at 10 K along cut B. Arrows in the bottom panels indicate the pump-induced population of the superconducting peak in the unoccupied side. (d) Nonequilibrium gap dynamics inside the Fermi arc. Adapted from Ref. [Ish16]

Similar experiments are performed by Ishida *et al.* on slightly under-doped Bi-2212 samples [Ish16]. They reported an ultrafast loss of superconducting gap near the d -wave node and the appearance of light-induced Fermi arcs upon pumping with $14 \mu\text{J}/\text{cm}^2$. In figure 4.2 (a), the underlying FS spectral weight is mapped in k space for various energies. At E_F , the spectral weight is localized around the node before the arrival of pump pulse (top row). The spectral weight distribution at E_F is elongated towards the off node at positive delay time, due to the photoinduced collapse of the superconducting gap (middle row). The evolution of the Fermi arc induced by the

pump pulse is highlighted by a difference image plot (lower row), where it is possible to notice depleted regions of spectral-weight at low energy. The transient spectra images recorded at various delay time are shown in figure 4.2(c). Apparently, the superconducting gap collapses almost instantly and displays a subsequent recovery on the picosecond timescale. The authors interpret the ultrafast loss of the superconducting gap as a filling process (inside the Fermi arc) due to spectral broadening.

Unfortunately, ARPES experiments performed with 6 eV probing photons do not allow to explore the entire Brillouin zone. Therefore the antinodal region is currently out of reach. In this portion of reciprocal space the superconducting phase coherence, cooper pairing and the presence of competing orders display a complex interplay. [Kon15]. Many authors explored the evolution of the pseudogap in equilibrium conditions. Detailed studies as a function of temperature and momentum suggest the existence of three temperature scales $T_c < T_{\text{pairs}} < T^*$. The emerging picture is that pseudogap and pairing gap are two distinct phenomena that compete at low temperature. At the crossover temperature T^* a crossover effect of debated origin leads to gapless Fermi arcs in the nodal region. Pairing already occurs at T_{pairs} well above T_c , but also significantly below T^* . Cooper pairs start to form below T_{pairs} , but their lifetime is too short to guaranty a coherent superconductor. Finally, a finite superfluid density develops below the transition temperature T_c and the d-wave gap is well defined [Reb13][Reb12].

In this chapter, we use time-resolved ARPES to measure dynamics of the near nodal gap by an ultrafast infrared laser pulse in an optimally doped Bi-2212 ($T_c=91\text{K}$) sample. Our data indicates that moderate photoexcitation induces a reduction of the gap size and the partial filling of the gapped region by superconducting fluctuations. Above a critical fluence, the pump pulse results in the full collapse of the gap. Interestingly, the threshold fluence at which the gap melts is comparable to onset where the quasiparticles dissipation starts to display a two component dynamics [Pio15].

4.2 Near nodal gap

Due to the d-wave structure, the superconducting gap of Bi-2212 varies as a function of azimuthal angle. It reaches a maximal value of roughly 40 meV in the antinodal region of the Brillouin zone. As a consequence only experimental protocols that are capable of measuring the spectral function with high-energy resolution can detect the gap. The data reported in chapter 3 have been obtained with the standard setup, which employs probing pulses with duration of 80 fs and spectral bandwidth of 70 meV. Such configuration is convenient to measure electrons dynamics with high temporal accuracy but lacks the energy resolution that is necessary in for a highly resolved spectroscopic measurement. I overcame this problem by adapting the experimental setup to the needs of a high-resolution experiment. Therefore the 6 eV beam has been passed through a dispersing prism and an optical iris. This setup allows for spectral filtering, resulting in pulses having the temporal duration of 600 fs. With such source, the overall energy resolution of the time resolved ARPES setup can be pushed to roughly 15 meV, which is a convenient value to resolve the superconducting gap.

The measurement of the gap required also to solve a second technical issue. Indeed due to the geometry of our setup (horizontal slit and manipulator with no tilt), it has not been possible to acquire off nodal QP dispersion by mounting the sample on a flat sample holder. In order to circumvent this limitation, we mounted the crystal on a sample holder that has been previously cut with tilt angle of 60° with respect to plane of the manipulator. By these means, we could acquire the QP dispersion along directions that cut the Fermi surface almost perpendicularly at azimuthal angle $\phi = 30^\circ$ and $\phi = 23^\circ$.

4.2.1 The near-nodal superconducting gap in the equilibrium state

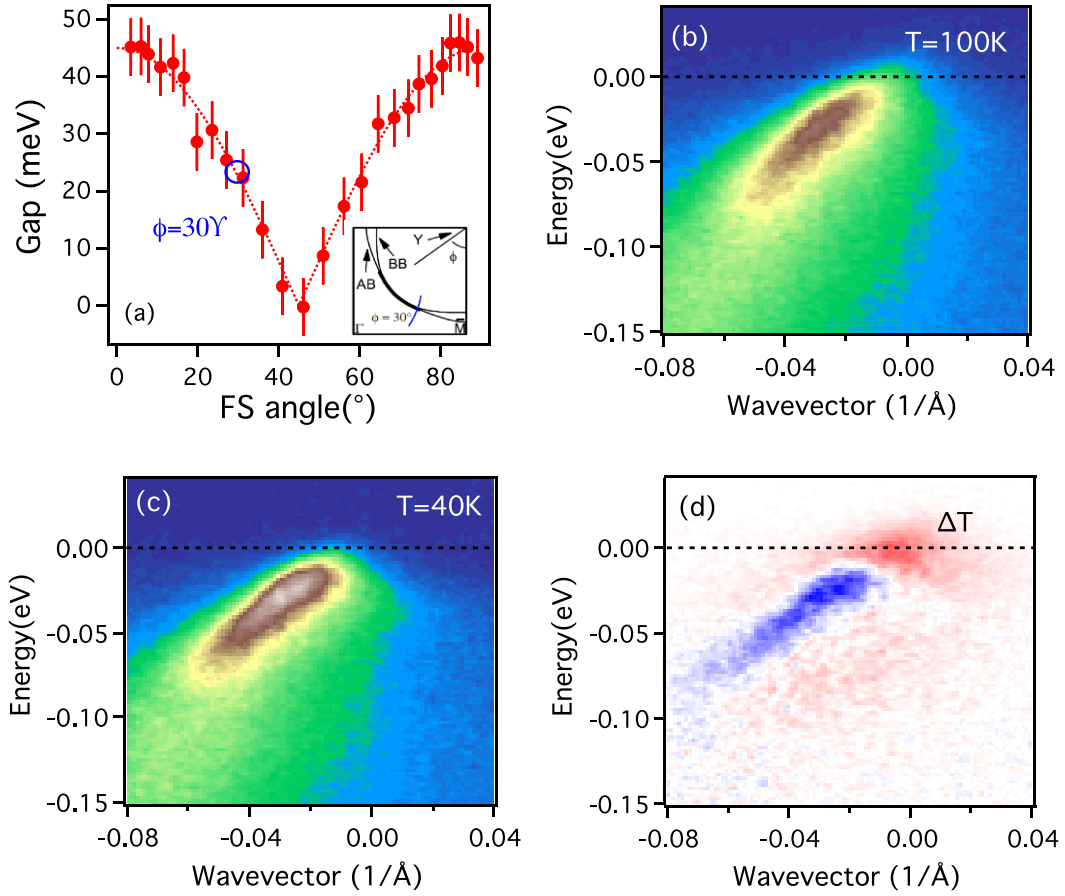


Figure 4.3 (a) Schematic of gap in optimally doped Bi-2212 as a function of the Fermi angle ϕ . The blue circle marks the near nodal cut FS angle $\phi = 30^\circ$. (b) and (c) Near nodal cut obtained by 6eV photoemission at 100K above T_c and at 40K below T_c . (d) Subtraction between (b) and (c), red indicates intensity gained and blue intensity loss.

We begin our discussion with a temperature dependent analysis of the equilibrium electronic band structure around Fermi level with laser-based ARPES, using only the 6 eV beam. ARPES spectra of optimally doped Bi-2212 were acquired by cutting the reciprocal space along the arc shown in figure 4.3(a). The quasiparticle crossing takes place at azimuthal angle $\phi = 30^\circ$ (where ϕ is defined from the Y point relative to $Y - \bar{M}$ as in the panel (a) inset). We show in figure 4.3 (b) the ARPES intensity maps acquired at the equilibrium temperature of 100 K, therefore in the metallic phase. The quasiparticle disperses towards the Fermi level, gaining coherence and intensity when the energy crosses the approximate value of -70 meV. This energy scale is related to a

collective mode coupled to single particles excitations and leads to a dressed Quasi-Particle (QP) near the Fermi level. The development of a superconducting phase induces detectable signatures on the electronic structure. Figure 4.3 (c) shows an intensity map acquired at 40 K, well below the transition temperature T_c . With respect to the previous case, the QP peak gains intensity while a finite gap inhibits the quasiparticle crossing. As shown in figure 4.3 (d), the effect of the thermal fluctuations on superconductivity can be enlightened by the subtraction between photoelectron intensity maps acquired above and below the transition temperature. Such plots visualize the redistribution of spectral weight due the melting of the gap and serves as reference for the photoinduced phase transition. The gradual formation of the superconducting gap is obtained by acquiring intensity maps at several intermediate temperatures.

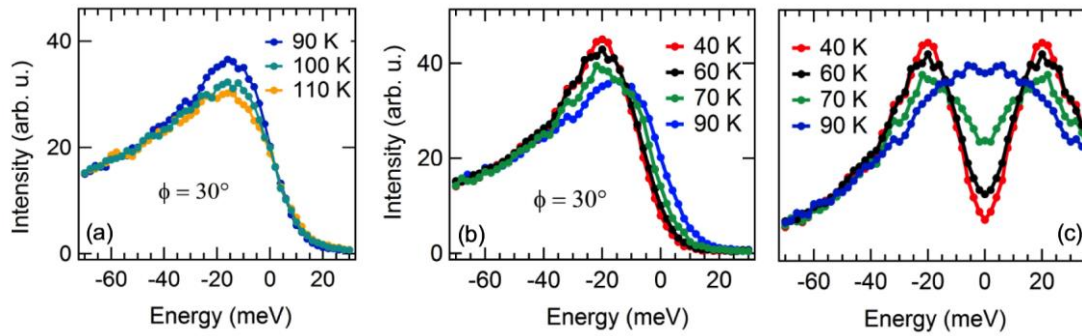


Figure 4.4 Temperature dependence of the near nodal electronic states in optimally doped Bi-2212. (a) and (b) energy momentum distribution curves (EDCs) at k_F for the equilibrium states above and below T_c ($T_c=91\text{K}$). (c) Symmetrized EDCs spectra below T_c .

Figure 4.4 (a) and (b) show the Energy Distribution Curves (EDCs) extracted at the Fermi wavevector for each one of these maps. The EDCs are normalized only by the total acquisition time so that a direct intensity comparison can be made accurately. As shown in figure 4.4(a), the leading edge of the EDCs is stable as long as the temperature is above the critical value. In contrast, figure 4.4 (b) shows that the leading edge moves towards lower energy when the system enters in the superconducting phase. This shift is the hallmark of an electronic gap at the Fermi Level. Following a common procedure in the data treatment, we show in figure 4.4 (c) symmetrized EDCs at different equilibrium temperatures. The distance between peaks

is often considered as phenomenological indicator of gap magnitude and attains the value of 20 meV at 40 K.

We realize that the distance between peaks retains 90% of the maximal value for $T=0.8 T_c$. In contrast to this finding, the mean field model would predict 70% of the maximal gap size. Such discrepancy arises from the important fluctuations of the superconducting order parameters in proximity of the transition temperature. The fluctuating regime is dominated by Cooper pairs with small lifetime and it is characterized by the progressive filling of the near nodal gap. The data of figure 4.4 (c) are consistent with such behavior and with the detailed analysis done in previous ARPES experiments.

4.2.2 The near nodal gap in the photoexcited state at low pump fluence

In figure 4.5 (a) and (b), the equilibrium (before pump excitation) and non-equilibrium (300 fs after pump excitation) ARPES intensity are shown as a function of energy and momentum for an optimally doped sample measured with pump fluence $41\mu\text{J}/\text{cm}^2$ at 35 K, far below T_c , along the near nodal direction $\phi = 30^\circ$. Figure 4.5 (c) shows the difference spectrum between (a) and (b), from which a largest pump-induced intensity changes are observed. The effects of photoexcitation are comparable to the thermal ones that are shown in figure 4.3 (d). Figure 4.5 (d) show the total transfer of spectral weight integrated from images acquired at delay times of 300 fs. Its dependence on pumping fluence displays a saturating behavior at roughly $50\mu\text{J}/\text{cm}^2$.

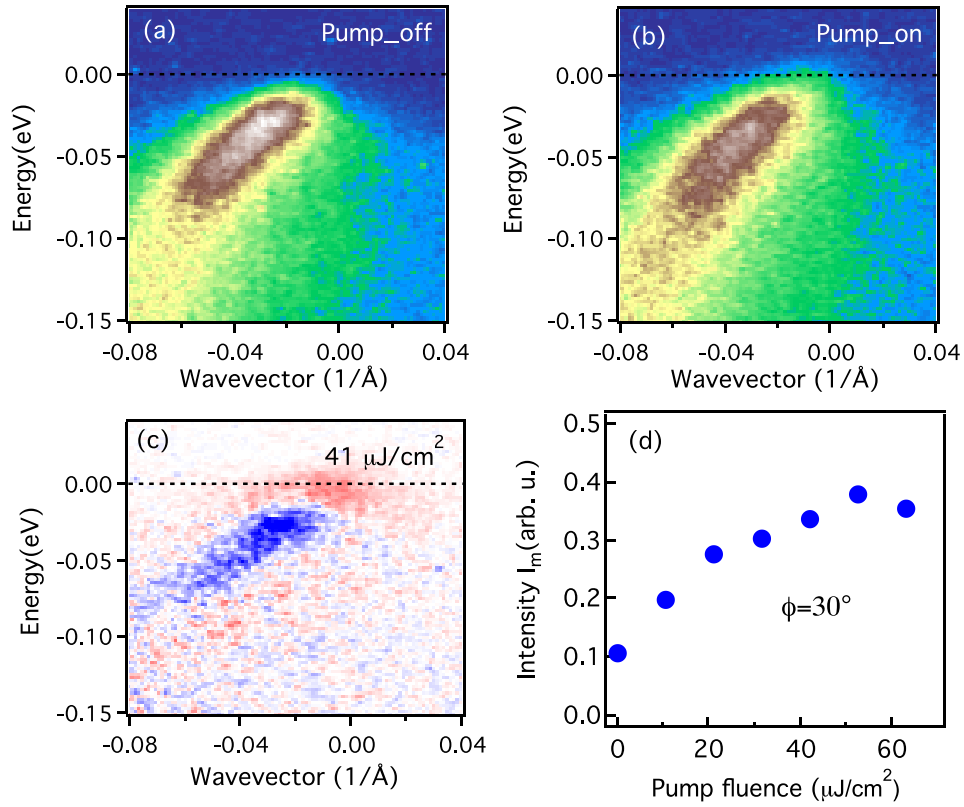


Figure 4.5 (a) Photoelectron intensity map showing the quasiparticle dispersion along the near nodal direction without the pump pulse. (b) Photoelectron intensity map acquired with pump pulse at delay time of 300 fs. (c) Pump-on minus pump-off intensity map at delay time $t=300$ fs. (d) Maximal value of the photoinduced signal I_m as a function of pump fluence.

4.2.3 Pump fluence dependence of the near nodal nonequilibrium gap in the photoexcited state

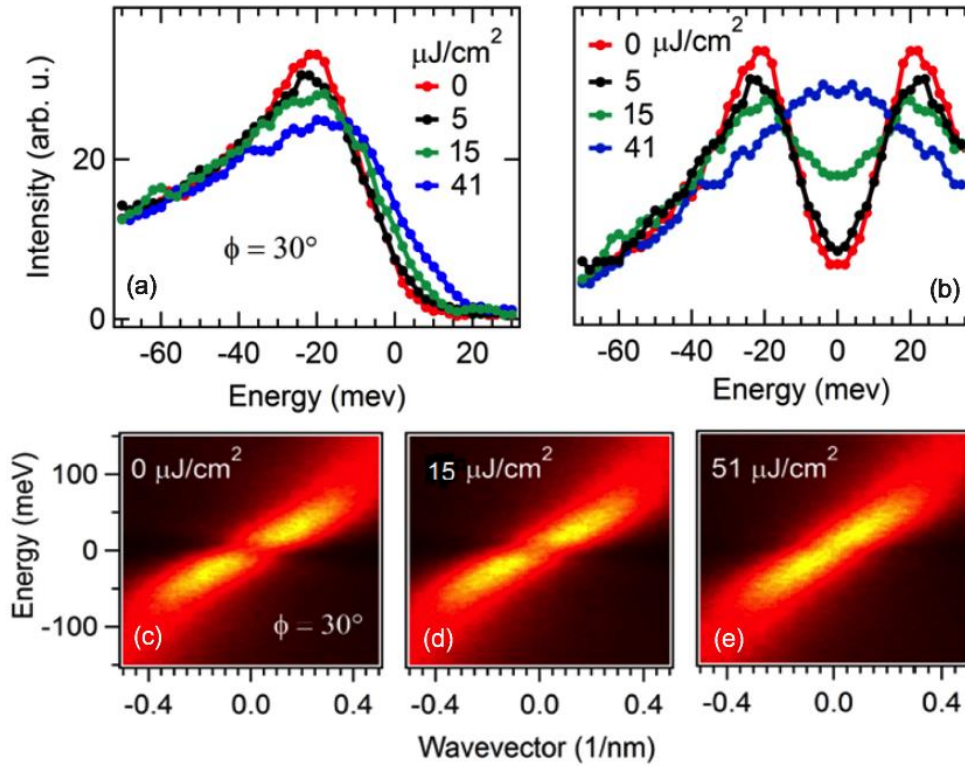


Figure 4.6 Fluence dependence of non-equilibrium gap at the near nodal cut $\phi = 30^\circ$, at $t=300$ fs for $T=35$ K. (a) and (b) EDCs and symmetrized EDCs at k_F . (c) ARPES intensity maps acquired for the maximum pump-probe overlap were symmetrized with (E_F, k_F) .

The complete description of the non-equilibrium case is obtained by acquiring photoelectron intensity maps at intermediate pumping fluences. We stress that photoexcitation also generates a photoinduced band displacement smaller than 3 meV. The origin of such effect has been discussed in chapter 3 in terms of a Seebeck field due to the large gradient of electronic temperature. In the following we always apply this minor correction when evaluating the gap melting. Figure 4.6 (a) shows EDCs extracted at the Fermi wavevector and at increasing excitation fluence. In analogy to thermal fluctuations, the photoexcitation of superconducting phase induces a shift of the leading edge. This one increase progressively with pumping fluence until the electronic gap has completely collapsed. Figure 4.6 (b) shows the symmetrized EDCs curves extracted at maximal pump-probe overlap with varying pump fluence. As we can see from the spectra, a pumping fluence of $F=41 \mu\text{J}/\text{cm}^2$ is large enough in order to close the near nodal gap at $\phi = 30^\circ$. On the other hand only a partial gap melting takes place at in the intermediate fluence regime. This can be also seen in figure 4.6

(c), where the transient ARPES intensity maps symmetrized with respect to (E_F, k_F) are shown for selected pump fluence. Notice in the symmetrized EDCs at pumping fluence of $15 \mu\text{J}/\text{cm}^2$ that the distance between the peaks is slightly smaller than the one of the unperturbed system. This finding suggests that the superconducting gap shrinks while it is progressively filled by fluctuations of the ordering parameter.

4.2.4 The dynamics of the near nodal transient gap at high pump fluence

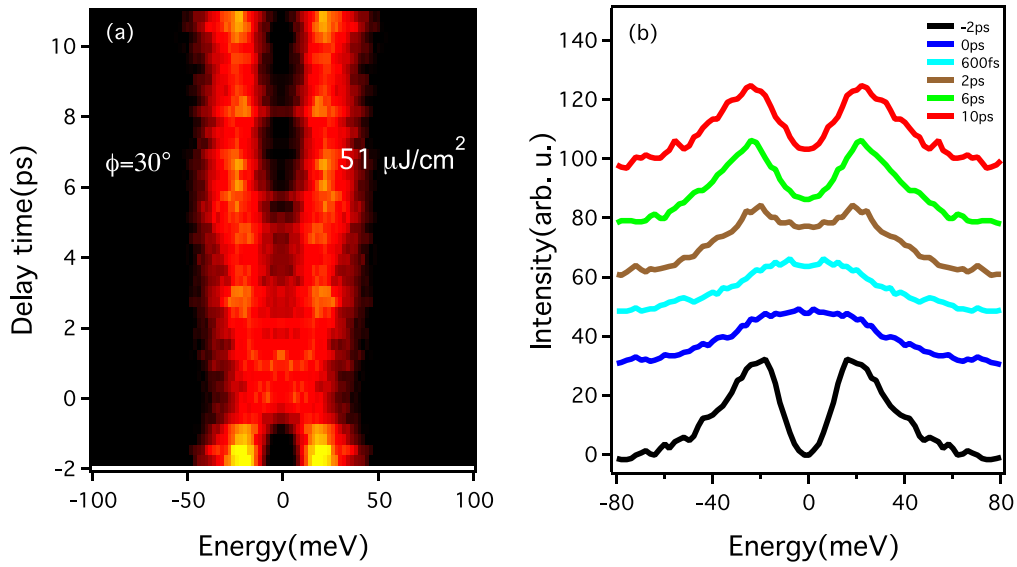


Figure 4.7 Transient superconducting gap dynamics at near nodal cut $\phi = 30^\circ$ for a pump fluence of $51 \mu\text{J}/\text{cm}^2$ and $T=35 \text{ K}$ below T_c analyzed using symmetrized EDCs. Measurement is characterized based on EDCs at the Fermi wave vector (k_F), which are then symmetrized with respect to the Fermi level. (a) False-color intensity plots of symmetrized EDCs spectral weight versus energy and delay time. (b) Symmetrized EDCs extracted at selected times.

We track the transient superconducting dynamic by using symmetrized EDCs. Figure 4.7 (a) plots on a false color scale the spectral weight of symmetrized EDC versus energy and delay time. Before the arriving of the pump pulse, a near nodal gap is observed at Fermi level. The gap shrinks and it is suddenly filled with spectral intensity when we apply the pump pulse. The gap remains filled during the first picosecond and recovers afterwards. Figure 4.7 (b) shows some selected symmetrized EDCs. We find that the near nodal gap collapse results from the close up of the two

symmetrized peaks plus a filling due to intra-gap states. Additionally, the gap magnitude does not fully recover even at 10 ps after the application of the pump pulse.

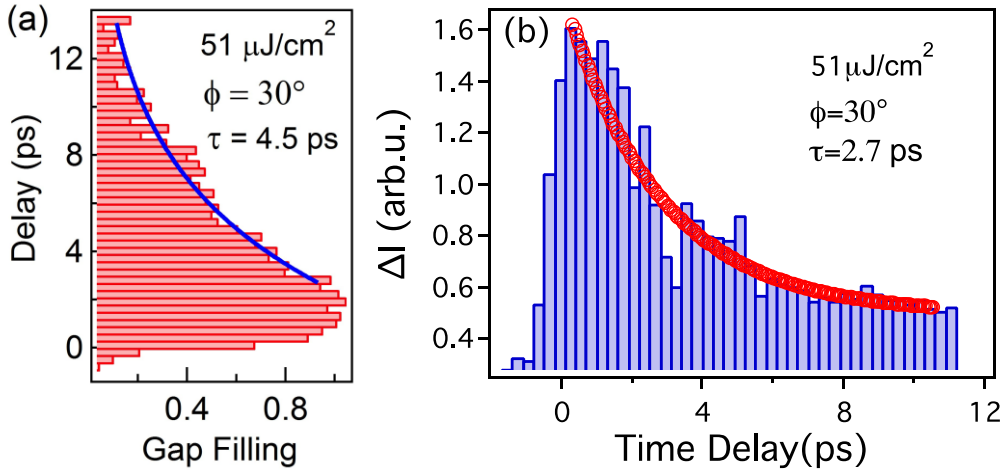


Figure 4.8 (a) Gap recovery dynamics obtained at near nodal cut by integrating the intensity of the energy window 20meV below and above Fermi level in 4.5(a). (b) Nonequilibrium quasiparticles population dynamics obtained by integrated of the intensity change above E_F .

In figure 4.8, we compared the nonequilibrium gap recovery (gap filling) with the quasiparticles dynamic for representative near nodal k-space gap cut $\phi = 30^\circ$. In figure 4.8 (a), the gap filling is acquired by integrating the intensity of the symmetrized EDC maps within $\pm 20\text{meV}$ energy window across the Fermi level. As we mentioned above, superconducting gap collapses as soon as the pump pulse arrives, although the initial recovery is delayed by about 1 ps. The recovery rate can be fitted with a single exponential function with time constant of 4.5 ps and an offset that accounts for a small thermal heating persisting at long timescales. Figure 4.8 (b) shows the temporal evolution of the above E_F spectral change intensity ΔI extracted at the $\phi = 30^\circ$ with pump fluence of $51 \mu\text{J}/\text{cm}^2$. The signal ΔI is defined as the integrated magnitude of intensity change shown in figure 4.5 (c). In contrast to the 1ps-delayed recovery of the non-equilibrium gap, the energy relation of photoexcited quasiparticles (which is partially captured by ΔI) begins just after arrival of the pump pulse. The relaxation rate of such integrated change spectral weight is faster than the characteristic time ruling the recovery of the superconducting gap.

4.3 Off nodal gap

4.3.1 The off nodal dispersion in the photoexcited state at high pump fluence

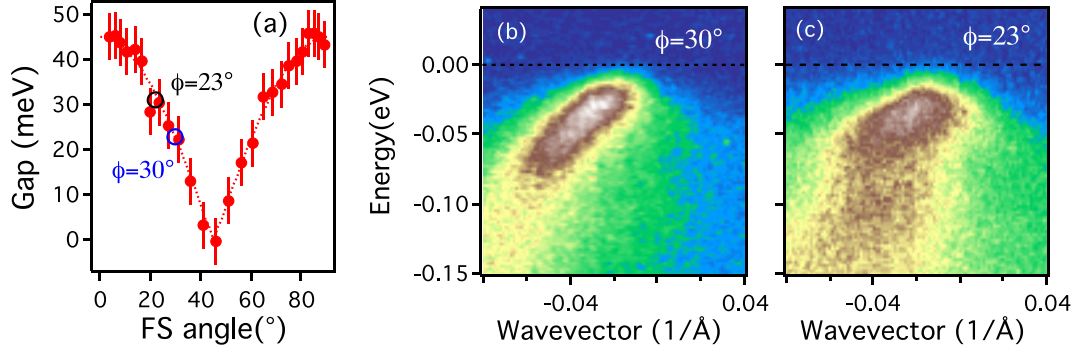


Figure 4.9 (a) Schematic of gap as a function of the Fermi angle ϕ . The blue circle marks the near nodal cut $\phi = 30^\circ$ and the black circle marks the off nodal cut $\phi = 23^\circ$. Equilibrium energy-momentum dispersions without pumping for near nodal cut (a) $\phi = 30^\circ$ and (b) off nodal cut $\phi = 23^\circ$ of k-space.

The expected gap size at $\phi = 23^\circ$ is marked in figure 4.9 (a) by a black circle. Figure 4.9 (c) shows the photoelectron intensity map measured along the off nodal cut at temperature of 35 K and without pump pulse. As a term of comparison, the near nodal spectra acquired in the same condition but at $\phi = 30^\circ$ are shown in figure 4.9 (b). A strong renormalization of the QP velocity takes place for excitation energy above -70 meV. The presence of a 25 meV superconducting gap induces a weak backfolding of the dispersive peaks at the Fermi wavevector. Note that QP dispersion along the antinodal cut displays smaller Fermi velocity than the nodal one. Moreover hints of bilayer splitting lead to two QP peaks that are partially overlapping and are still not resolved. It has been shown by Smallwood *et al.* [Sma14] that such splitting becomes larger and clearer by measuring nearer to the antinodal direction.

4.3.2 Pump fluence dependence of the off nodal nonequilibrium gap in the photoexcited state

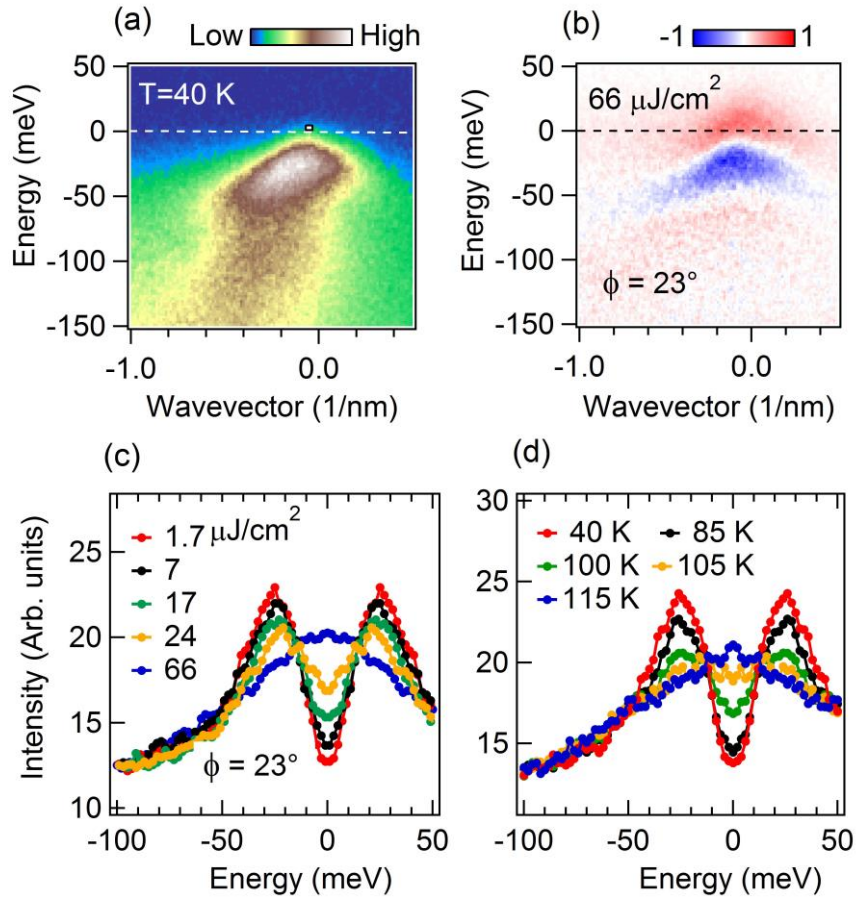


Figure 4.10 The data of this image have been acquired at azimuthal angle $\phi = 23^\circ$. (a) Intensity map in equilibrium at the base temperature of 40 K. (b) Pump-on minus pump-off signal acquired at 40 K with photoexcitation fluence of $66 \mu\text{J}/\text{cm}^2$. (c) Symmetrized EDCs acquired at 40 K and just after photoexcitation with different pumping fluence. (d) Symmetrized EDCs acquired in equilibrium conditions at different sample temperatures.

According to the work of Smallwod *et al.*, the antinodal gap is more robust in the off nodal direction. At azimuthal angle of 21° they observed remnant pairing at the fluence of $23 \mu\text{J}/\text{cm}^2$. We decided to extend the measurements of the off nodal gap to the high fluence regime. Figure 4.10(a) displays a photoelectron intensity map acquired at azimuthal angle $\phi = 23^\circ$ and 40 K. Due to bilayer splitting, the map contains two parallel QP bands that are not spectrally resolved. A strong

renormalization of QP dispersion takes place for excitation energy above -70 meV. The presence of a 25 meV superconducting gap induces the weak backfolding of dispersive peaks at the Fermi wavevector. We show in figure 4.10 (b) the pump-on minus pump-off map acquired just after optical pumping with $66 \mu\text{J}/\text{cm}^2$. The observed contrast visualizes the transfer of spectral weight from the QP peak to the gapped spectral region. Symmetrized EDCs of figure 4.10(c) display the photoinduced filling of the gap at different pumping fluence. Any signature of pairing is lost at high photoexcitation density. We show in figure 4.10 (d) that a similar spectral evolution takes place in equilibrium by increasing the sample temperature. The presence of a remnant gap above T_c is due to the incipient pairing of the fluctuating condensate away from the nodal direction. Such regime extends up to 115 K and it is expected because of the small spatial extension of Cooper pairs in copper oxides [Rul11, Ber10, Wan05, Per15]. Several ARPES works reported comparable results for different doping levels [Kan07, Kon11, Kon15, Par13].

4.3.3 The dynamics of the off nodal transient gap at high pump fluence

In figure 4.11, we discuss the temporal evolution of the off nodal superconducting gap in response to the photoexcitation, with pump fluence of $66 \mu\text{J}/\text{cm}^2$. Figure 4.11 (a) shows the symmetrized EDC spectral weight, extracted from symmetrized EDCs at Fermi wave vector, versus energy and delay time at $\phi = 23^\circ$. Apparently the off nodal gap shows a faster recovery rate than the near nodal one. In the following, I will analyze this issue in detail.

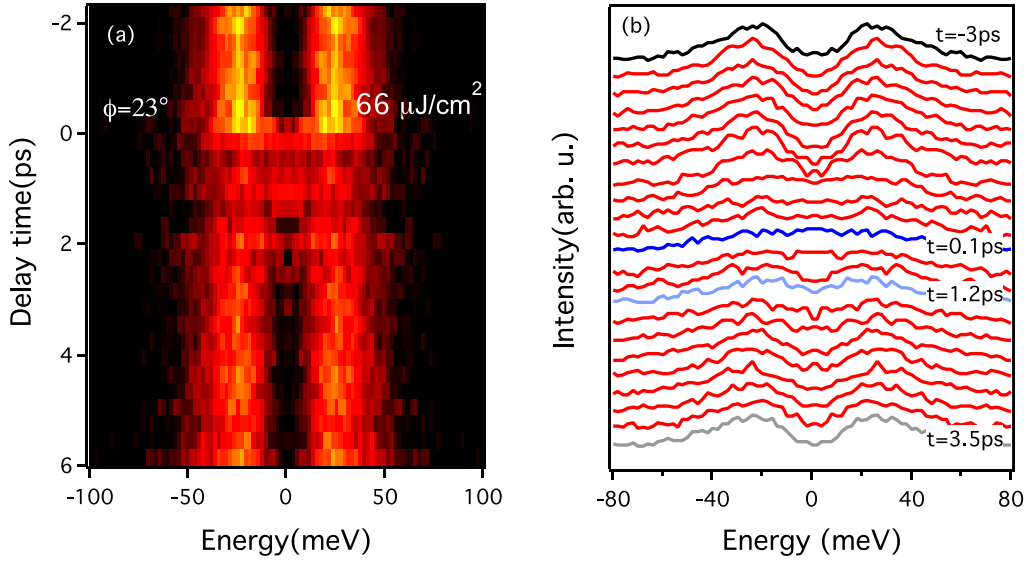


Figure 4.11 Transient superconducting gap dynamics at off nodal cut $\phi = 23^\circ$ for a pump fluence of $66 \mu\text{J}/\text{cm}^2$ and $T=35 \text{ K}$ ($T_c=91 \text{ K}$) analyzed using symmetrized EDCs. (a) False-color intensity plots of symmetrized EDC spectral weight versus energy and delay time. (b) EDCs at selected times for a representative near-nodal momentum cut.

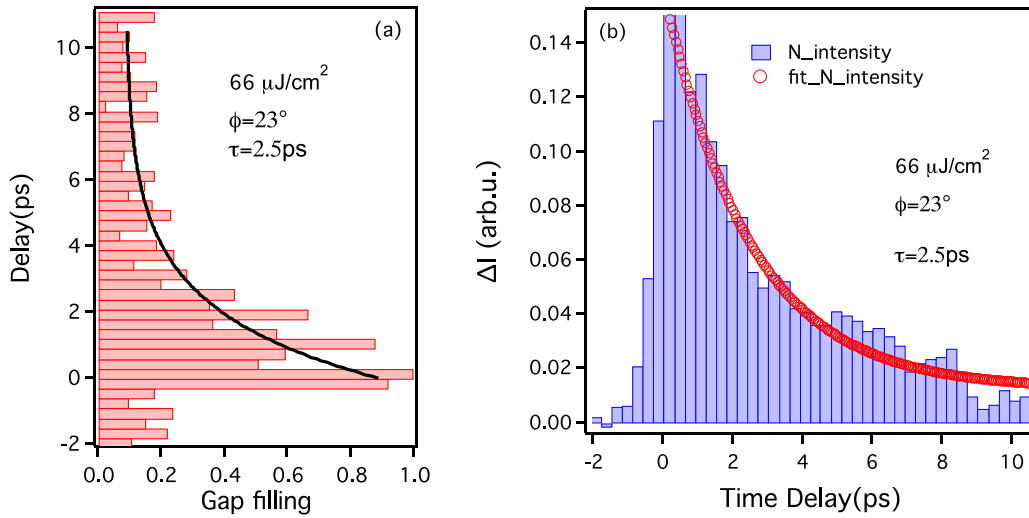


Figure 4.12 (a) Gap recovery dynamics obtained at off nodal cut by integrating the intensity of the energy window 20meV below and above Fermi level in 4.11 (a). (b) Nonequilibrium quasiparticles population dynamics obtained by integrated of the intensity change above E_F .

In Figure 4.12 (a), the off nodal gap filling, which is defined by the normalized integration of the gap intensity of energy window 20 meV below and above Fermi

level in figure 4.12 (a), is showing as a function of delay times. The gap recovery starts just after the arrival of the pump pulse. By fitting the gap evolution with an exponential function we extract a characteristic timescale of 2.5 ps. This value is twice smaller than the superconducting recovery time observed near to the node. However, such difference may be related to a continuous wave heating that we have observed during these measurements. Finally, figure 4.12 (b) shows the evolution of integrated photoemission intensity above the Fermi level. The nonequilibrium quasiparticles populations build up almost instantly and display a cooling rate that is similar to the gap recovery.

4.4 Momentum and pump fluence dependence of the nonequilibrium gap in the photoexcitation state

We show in figure 4.13 the filling factor of the superconducting gap as a function of pump fluence, acquired for azimuthal angles $\phi = 30^\circ$ and $\phi = 23^\circ$. No signature of pairing can be detected for pumping fluence larger than $40 \mu\text{J}/\text{cm}^2$. Our data are qualitatively in line with the original report of Smallwood *et al.*, confirming that Cooper pairs do not sustain high photoexcitation densities. Although our photon source does not allow to reach the antinodal region, the weak dependence of threshold fluence on the azimuthal angle should not affect this conclusion. Moreover, measurements along the antinode will face the complications due to the spectral signature of a competing order.

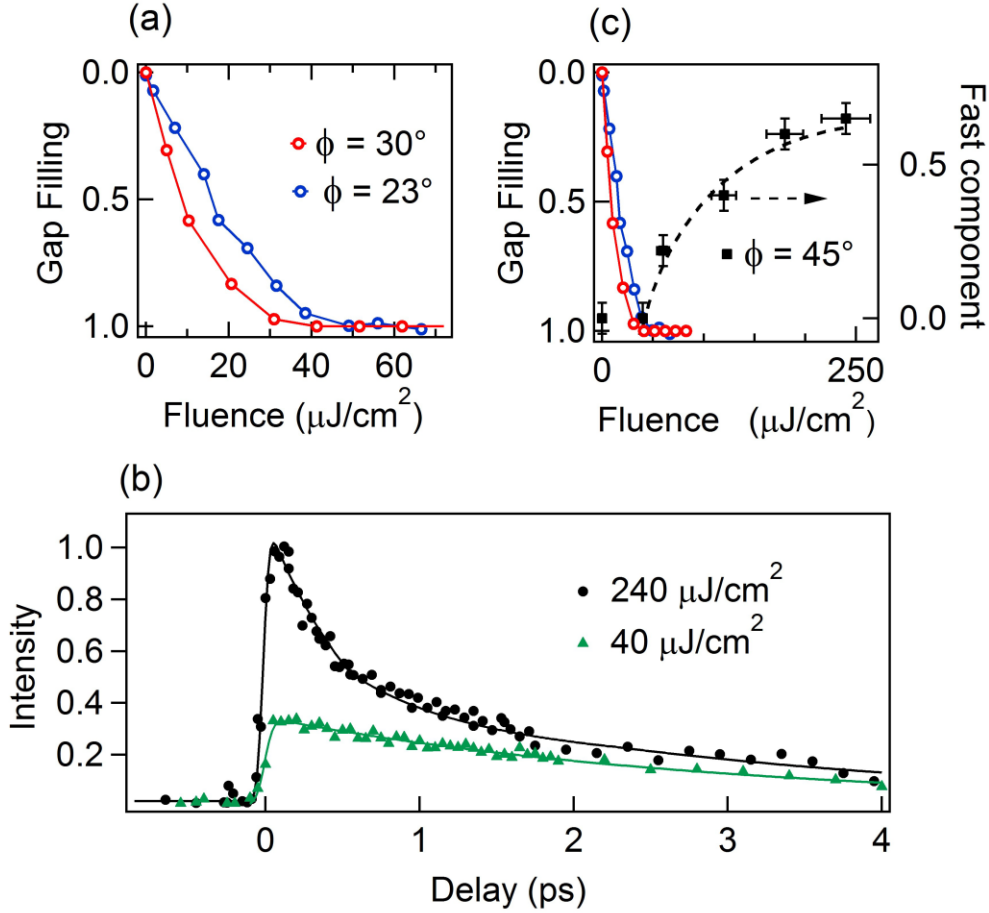


Figure 4.13 (a) Filling factor of superconducting gap at $\phi = 30^\circ$ (red circles) and $\phi = 23^\circ$ (blue circles) extracted just after photoexcitation with a variable pump fluence. (b) Temporal evolution of nodal quasiparticle intensity integrated in an energy window from the Fermi level up to excitation energy of 50 meV. Comparison between the QPs relaxation after photoexcitation with $40 \mu\text{J}/\text{cm}^2$ (green triangle) and $240 \mu\text{J}/\text{cm}^2$ (filled black circles). (c) The filling factor of the gap (open circles) and the fast component of the nodal QPs relaxation (filled dark squares).

As also discussed in chapter 3, we propose the existence of a fluence window between $12 \mu\text{J}/\text{cm}^2$ and $40 \mu\text{J}/\text{cm}^2$ in which optimally doped Bi-2212 does not hold phase coherence but still displays pairing. This hypothesis relies on THz measurements of the superfluid density in photoexcited thin films. However, after a private discussion with Kaindl, we realized that the fluence provided in reference Ref. [Car04] might not coincide with the incident fluence of our measurements. Therefore a conclusive statement on this issue call for future experiments. A reliable comparison between gap

evolution and supercurrent response would indeed require tr-THz and tr-ARPES measurements on the same thin film and possibly with the same setup.

Next we compare the temporal evolution of the gap with the energy relaxation of nodal QPs. In the latter case we employ the setup providing 80 fs probe pulses with 70 meV bandwidth. Figure 4.13 (b) shows the temporal evolution of nodal QPs signal integrated in the energy window [0, 50] meV. After photoexcitation with fluence $40 \mu\text{J}/\text{cm}^2$, the QPs follow a single exponential relaxation with decay constant of 2.5 ps. Upon photoexcitation with $240 \mu\text{J}/\text{cm}^2$, the dynamics display an initial decay with inverse rate of 0.5 ps. At longer delays the cooling time converges to 2.5 ps, independently on photoexcitation intensity. These results are consistent with the data first reported by Cortés *et al.* and have been thoroughly discussed in the previous chapter. Apparently, the relaxation of the energy integrated QPs signal can be correctly reproduced by a double exponential decay. The fast component becomes visible above a threshold fluence and gains weight upon increasing the photoexcitation density. We compare in figure 4.13 (c) the amplitude of the fast QPs delay with the filling factor of the superconducting gap. The fast dissipation rate becomes detectable at the same threshold fluence where the superconducting gap has fully collapsed. Our observations indicate that when the applying pump fluence is not sufficient to completely Cooper pairs, the quasiparticle dynamics evolve smoothly and on the picosecond timescale. Conversely, if the pump fluence is sufficient high to completely destroy the Cooper pairs, two component dynamics emerge, with distinct femtosecond and picosecond timescales. Such connection has been already outlined by Ref. [Sma15], although at fluence values lower than the ones of our work. Moreover, Smallwood *et al.* proposed that dynamical gap opening during the quasiparticle relaxation process effect recovery rate of photoexcited quasiparticles [Sma16]. They interpreted the picosecond decay rate as a counterbalance quasiparticle relaxation at fixed energy, because the quasiparticles at lower energies are steadily lifted by the gap opening on a picosecond timescale. This interesting model is likely capturing the correct physics. On the other hand, we have showed in the previous chapter that it overestimates the initial decay rate of Quasiparticles at high fluence. The fast developing theory of non-equilibrium dynamics in complex systems may soon lead to more precise simulations.

Chapter 5

Angle resolved photoemission spectroscopy study of the $\text{La}_{2-x-y}\text{Nd}_y\text{M}_x\text{CuO}_4$ (M=Sr, Ba; $x=0.12-0.14$; $y=0,0.4$) high temperature superconductor

5.1 Motivation

The nature of the normal-state gap (pseudo-gap) and its relationship with superconductivity are believed to hold the key for understanding the mechanism of high- T_c superconductivity. In cuprates, the pseudo-gap opens well above the superconducting critical temperature at moderate doping. Many previous experiments suggest that the pseudo gap is distinct from superconducting gap and that the pseudo-gap is a single gap of d-wave. A large body of experimental evidence now suggests that at least, in a small region of the underdoped phase diagram, there is a broken-symmetry state that is distinct from homogeneous superconductivity. In the "214 family", the low temperature phase is accompanied by the ordering of charge and spin in a stripe form, where a fraction of carries forms a charge modulation coexistent with spin modulation in a configuration which is referred to as stripes [Tra95, Zaa89]. Charge-modulations have been proposed as a possible origin of the broken-symmetry state, either in the "stripes" [Kiv03], or in the Charge-Density-Wave [Tor13] form. In the region of the phase diagram where these charge-modulations are static, scattering

experiments have suggested that they competes with superconductivity [Cha12, Com14, Net14], although a possible different role of the fluctuating stripes is still debated [Kiv03]. We can pin the fluctuating "stripes" in $La_{2-x}Sr_xCuO_{4+d}$ (LSCO) at $x=1/8$ doping to static ones, by replacing Sr with Ba in $La_{2-x}Ba_xCuO_{4+d}$ (LBCO), or with partial substitution of Nd on the La site in $La_{2-x-y}Nd_ySr_xCuO_{4+d}$ (LNSCO). Then, in a narrow doping region around $x=1/8$, the charge ordering in LBCO or LNSCO is static and suppresses superconductivity [Axe89]. While, in LSCO, the impact of the density modulation is mitigated, causing only a slight depression in T_c in the vicinity of $x=1/8$ [Bil11].

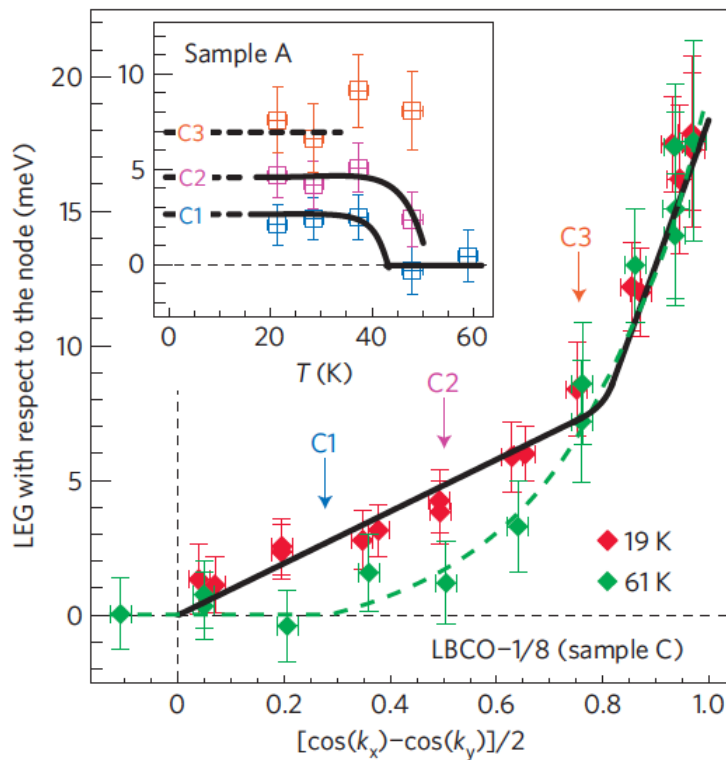


Figure 5.1 The leading edge gap (LEG) function of LBCO-1/8 ($T_c=4\text{ K}$) at $T=19\pm 2\text{ K}$ is compared with the one at $T=61\pm 2\text{ K}$. Inset: Detailed temperature dependence in the nodal gap region of at three selected momentum positions, C1–C3, as indicated by arrows of different colours. Note that C3 is close to the crossover position of the two gap components. From Ref. [He 09]

The nature of the pseudo-gap on LBCO close to 1/8 doping has been investigated by He *et al.* [He09]. They found the ground state pseudogap has a pronounced deviation from the simple d-wave form. As shown in figure 5.1, the pseudo-gap contains two

distinct components: a d-wave component within an extended region around the node and the other abruptly enhanced close to the antinode. Although, the author propose that a possible precursor-pairing energy scale around the node and another of different but unknown origin near the antinode. Actually, if we take a close look at the temperature dependence of the pseudo-gap, we can see that the near nodal gap (C1) survives at the stripes states and persist up to around 45 K, which is close to the LTT-LTO transition temperature, indicating a possible link between the pseudo-gap and stripe modulations.

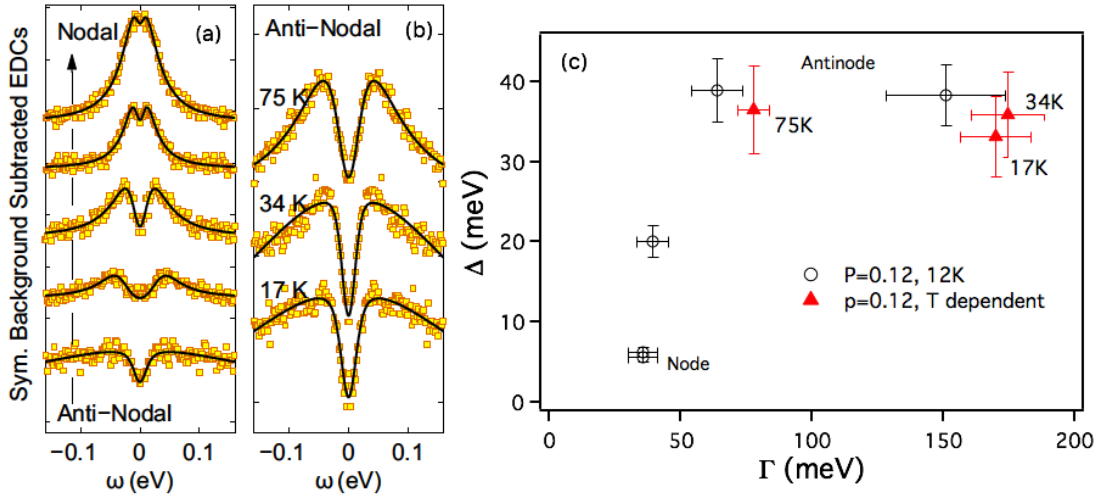


Figure 5.2 (a) Momentum dependence of symmetrized energy-distribution curves (EDCs) taken at k_F moving from antinodal (bottom) to nodal (top) region for LNSCO ($x= 0.12$). (b) Temperature dependence of antinodal symmetrized EDCs recorded on LNSCO ($x= 0.12$) (c) Normal-state gap Δ vs the scattering rate Γ extracted by fitting. From Ref. [Mat15]

The link between the anti-nodal pseudo-gap and the charge modulations (CDW/stripe phase) is explored by C. Matt and co-workers with an ARPES study of the charge stripe ordered system $La_{1.6-x}Nd_{0.4}Sr_xCuO_4$ (Nd-LSCO) at 1/8 doping [Mat15]. As shown in figure 5.2, the spectra and pseudogap are characterized with two parameters (the gap Δ and scattering rate Γ) by fitting the symmetrized EDCs. The sudden quasiparticle decoherence (much smaller ratios of Δ/Γ) effect is extracted from the antinodal line shape. The observed different scattering rate in the LTT charge stripe phase and LTO phase in the anti-nodal region is identified as the signatures of the influence of charge stripes order. Although the gaps size of antinodal-gap seems

temperature independent, a pseudo-gap with 5meV is clear at the nodal and increasing as a d-wave when approach to the antinode.

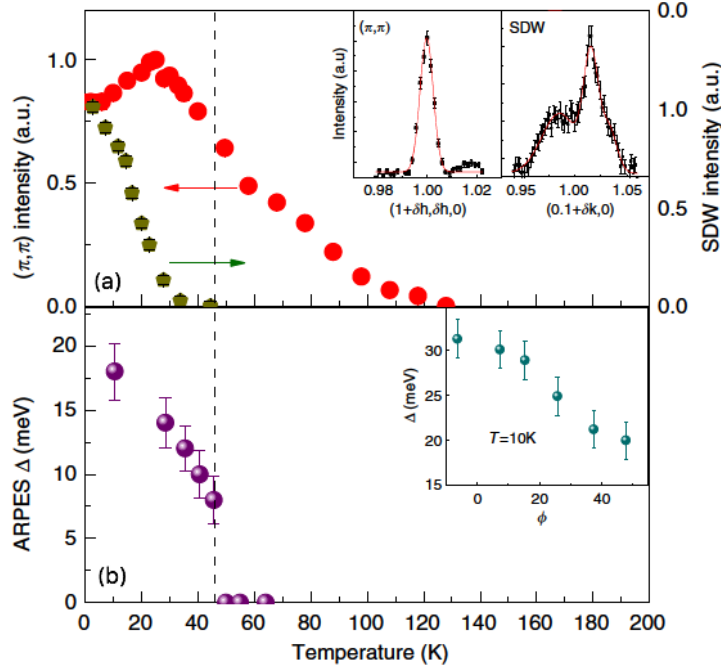


Figure 5.3 (a) Commensurate and incommensurate neutron diffraction intensity. The SDW inset shows the incommensurate peaks. The (π, π) inset shows the commensurate peak. (c) ARPES nodal gap Δ at k_F , versus temperature. The inset shows the angular dependence of the gap $\Delta(\phi)$. From Ref. [Dra14]

More recently, the nature of the pseudo-gap close to the node has been investigated in "214" system LSCO, but without charge modulation pinning and for low doping [Dra14]. The authors show a link between SDW and the nodal gap (possibly a Mott-gap), which appears close to the nodal directions, by a direct comparison of T_{SDW} (the onset temperature of the incommensurate magnetic order determined from the elastic neutron scattering measurements) and T_{Gap} (the onset temperature of nodal gap obtained with ARPES). As shown in figure 5.3, the nodal gap opens well below the commensurate ordering at 140 K, and near to the incommensurate SDW ordering temperature of 30 K.

Additionally, a recently time-resolved ARPES study shows that the ultrafast loss of superconducting gap near the d-wave node, or light-induced Fermi arcs, is accompanied by spectral broadenings and weight redistributions occurring within the

kink binding energy [Ish16]. The undressing of quasi-particles from the kink bosons is supposed to be the underlying mechanism of the spectral broadening that induces the Fermi arc. Actually, in 214 cuprates, the role of charge/spin modulations ("stripes") on the interaction that give rise to the "kink" in the electronic bands as seen by ARPES is still unclear. However, after the seminal work of Lanzara [Lan01] as have already discussed in Chapter 1, little work has been done to test the hypothesis of a link with phonon modes as was suggested in the introduction. Graff and co-worker [Gra08] shown in (Bi2201) that the wave-vector connecting FS sheet parallel to the anti-nodal direction show a kink at about 60 meV only for those wave-vector that show a softening to a similar energy of the Cu-O bond stretching mode. A similar results has been shown later by Park and co-workers [Par14], confirming the same behaviour in "214" systems. However, little has been done so far in "214" system, in particular close to the 1/8 doping and with pinning centre (Ba, Nd) for the charge modulation.

In this chapter, we will report Angle Resolved PhotoEmission Spectroscopy (ARPES) results for the $La_{2-x}Sr_xCuO_{4+\delta}$ ($x=1/8, y=0$, LSCO), $La_{2-x-y}Nd_ySr_xCuO_{4+\delta}$ ($x=1/8, y=0.4$, LNSCO) and $La_{2-x}Ba_xCuO_{4+\delta}$ ($x=0.14$, LBCO) grown in the same condition, in order to study the nature of the pseudo-gap and its relationship with the superconductivity, the possible link between the spin/charge modulations and the kink in the stripes cuprate superconductors.

5.2 Preparations and Measurements

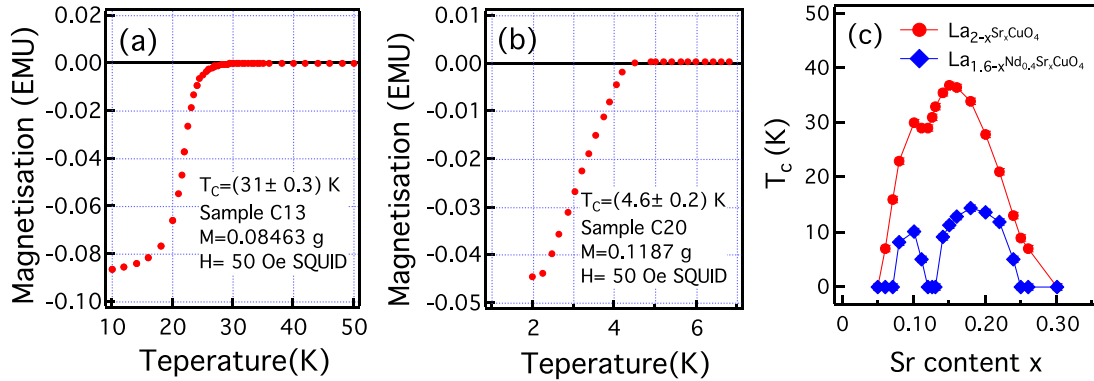


Figure 5.4 The magnetization measurements of $La_{1.48}Sr_{0.12}CuO_4$ (sample_C13) (a) and $La_{1.48}Nd_{0.4}Sr_{0.12}CuO_4$ (sample_C20) (b) crystals grown the by floating zone technique. Temperature dependence of the magnetization under a field of 50 Oe for the zero field cooled (ZFC) condition. (c) Plots of T_c as a function of Sr composition x for $La_{2-x}Sr_xCuO_{4+\delta}$ and $La_{2-x-y}Nd_ySr_xCuO_{4+\delta}$ measured on power ceramics precursor of these crystals.

High quality single crystal of nearly 1/8 doped $La_{1.88}Sr_{0.12}CuO_4$, $La_{1.48}Nd_{0.4}Sr_{0.12}CuO_4$ and $La_{1.86}Ba_{0.14}CuO_4$ were grown from the melt in an image furnace by the traveling solvent floating zone (TSFZ) method under a pressure of 3 bar oxygen at the ICMMO, Orsay, as in Ref. [Das08]. Superconducting properties and crystalline orientation were determined at ICMMO. For the LBCO, the $T_c = 18.1$ K with $\Delta T_c = 7$ K defined as the temperature range from 90% to 10% of the maximum Meissner signal was measured at ICMMO after growth. It is consistent with microprobe results indicating a content of $x = 0.14 \pm 0.01$ as reported elsewhere [Axe89]. While for the LSCO and LNSCO, the T_c for the particular crystal sections I cut and oriented for the ARPES experiment were measured and determined from the susceptibility measurement by SQUID magnetometer at MPBT, UPMC. The structural characterizations are made using 3-axes spectrometer at LLB, Saclay, in particular to measure the LTO-LTT transition temperature and the stripe pinning one. As in figure 5.4 (a) and 5.4 (b) where the ZFC curves for two sample cleaves are shown, the onset temperature of the superconducting transition (T_c) are 31K for LSCO and 4.6 K for LNSCO, respectively. In figure 5.4 (c), we also show the characterized T_c as a function of Sr concentrations (x) for the LSCO and LNSCO power ceramics, which is consistent with the previous

results on single crystals. The phase diagram of LSCO exhibits a sharp drop in superconducting transition temperature, T_c close to 0K, when doped $\sim 1/8$ holes per cu site ($x=1/8$), while having almost equally strong superconducting phase, with maximum $T_c \sim 30K$ at both higher and lower dopings.

5.2.1 ARPES Data Treatment:

As described in the previous chapter 2, the ARPES measurements were performed on CASSIOPEE-B-ARPES beamline (Synchrotron SOLEIL, France), which has the necessary energy and momentum resolution as well as the necessary photon energy and temperature ranges, allowing a fast and systematic exploration of the experimental phase space.

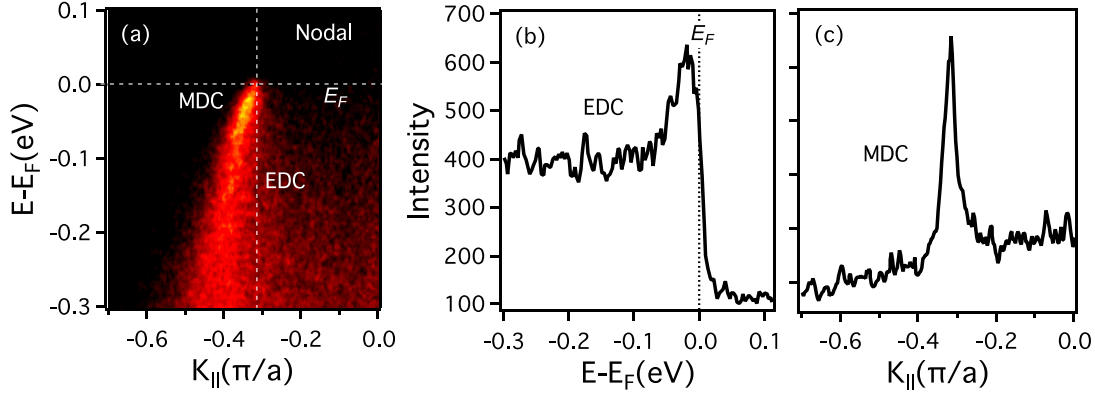


Figure 5.5 (a) ARPES intensity map of 1/8-doped LSCO as a function of binding energy along the Γ -M direction (nodal direction) measured at 55 K. (b) Energy Distribution Curve (EDC) of spectral intensity at K_F integrated with in $\pm 0.01\text{\AA}$. (c) The Momentum Distribution Curve (MDC) of the spectral intensity at E_F integrated with in $\pm 5 meV$.

Energy and Momentum Dispersive Curves: The photoelectron intensities $I(E_{kin}, \varphi, \theta)$ are acquired as a function of kinetic energy E_{kin} and emission angle φ along a particular direction given by θ , and represented with a 2D color map as an example in figure 5.5 (a). In this chapter, most of the data analyses are based on the energy distribution curves (EDCs) and momentum distribution curves (MDCs) extracted by slicing the 2D images, as shown in figure 5.5 (a). Since “214” systems are known to have poor spectral weight at E_F , a metallic reference spectrum is measured. For our

ARPES studied the sample holder frame was used as reference. It is a copper block in electrical contact with the sample. So the Fermi level is determined by fitting the Fermi edge measured on the sample holder at each temperature. Essentially, EDCs correspond to ARPES intensity as a function of energy (with momentum or angle fixed), and MDCs correspond to ARPES intensity as a function momentum (with energy fixed), as depicted in figure 5.5 (b) and 5.5 (c). The position of the peak in an EDC denotes the (ω, k) location of the electron state, including all many-body renormalization effects. The width corresponds to the energy uncertainty of that state and is related to the scattering rate, or lifetime, of that quasiparticle, convoluted with resolution as explained in previous chapter. In principle EDC analysis is more direct than MDC analysis because no conversion with velocities is required. However, the inelastic photoemission background, Fermi distribution, and electron self-energy change strongly with energy, which all complicate the EDC line shape. The MDCs, on the other hand, are relatively unaffected by these terms because in general they have a very weak (if any) momentum dependence on the scale of a single ARPES spectrum. Therefore, MDCs are typically closer to the lorentzian line-shape expected from the electron Green's function, which makes peak fitting easier and more reliable.

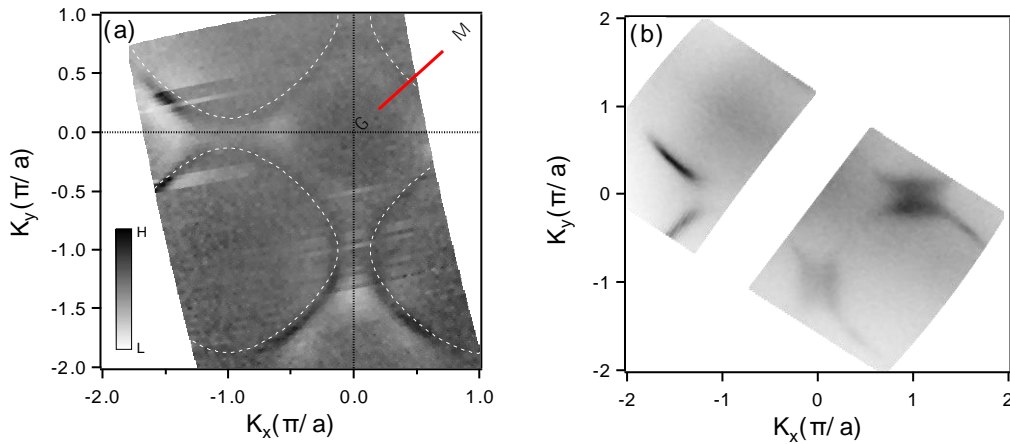


Figure 5.6 (a) The Fermi surface of $\text{La}_{1.88}\text{Sr}_{0.12}\text{CuO}_4$ (LSCO) with a large momentum coverage measured at a photon energy of $\omega = 55$ eV at $T=5$ K below T_c . (b) The same as (a) but at $T=55$ K above T_c . The dashed curves represent the tight binding Fermi surface results from a global fit to the data as guide to the eye.

Fermi surface: Mapping the Fermi surface (FS) is of great value for understanding of correlated and electronic properties of curates because often electrons near the Fermi

level are coupled to other lower energy excitations. FS maps of the LSCO, LNSCO and LBCO have been investigated in this thesis and the obtained results are discussed in this chapter. Experimentally, the Fermi surface is represented by the intensity maxima of the energy momentum space map taken at the Fermi level. Figure 5.6 (a) shows an example of FS map of LSCO reconstructed from experimental ARPES data measured at 5 K with a photon energy of $\omega=55\text{eV}$, which represents the integrated photoelectron intensity of spectra over a small energy window $E = E_F \pm 10 \text{ meV}$, normalized using the intensity well above E_F .

The images and the data analysis have been performed using procedures for the Igor © commercial data analysis software [Igor] already developed by the CASSIOPEE beamline staff for data extraction, and by V. Brouet for angle conversion [Bro14]. In this chapter, we wrote procedures for the EDC and MDC data analysis of the bands according to a standard protocol as follows: the EDCs of intensity are integrated over a small interval of 0.02 \AA around K_F and the MDCs are integrated over a small interval of 10 meV around E_F . The EDCs are used in the process of determining the Fermi-level and the experimental resolution from raw data. The MDC analysis are used for tracking band dispersion and extracting the real part of the self-energy function Σ' . However, extracting the imaginary part of the self-energy function Σ'' is more complicated through MDC analysis since it requires the knowledge of the non-interacting (bare) velocity that is not measured experimentally.

5.3 Results of the study

5.3.1 The LSCO results at the critical doping $x = 0.12$

LSCO has one of the simplest crystal structure among cuprates with single CuO_2 layers and its hole concentration is rather accurately determined by the Sr concentration x for a given oxygen content. It covers the whole range of the phase diagram with doping, from antiferromagnetic charge transfer insulator to metal. On the other hand, LSCO is complicate in that as it undergoes a structural distortion from the high-temperature tetragonal (HTT) phase to the low temperature orthorhombic (LTO) phase in the superconducting compositions and even has an inherent instability towards the low-temperature tetragonal (LTT) phase.

We start the discussion of the experimental data with the FS map plotted in figure 5.6, which represents a well-defined FS of LSCO for the compound $x=0.12$ obtained at $T=5$ K in the superconducting states 5.6 (a) and $T=55$ K in the normal states 5.6 (b). The Brillouin zone guidelines shown in figures of this work are drawn by ignoring the finite k_z dispersion in the system, as this is indiscernible within the experimental accuracy for the photon energies used. The FS is consistent with the observation in early studies and the underdoped sample ($x=1/8$) displays a hole-like FS with large pocket centered at M (π, π) as in the other hole-doped cuprates. Similar to the Ref. [He_11], I also do not see the shadow bands previously reported in $1/8$ doping, which potentially represent additional ingredients in the band structure that goes beyond the single-band picture. Indeed, it was previously reported that the shadow band intensity could be even enhanced at $x = 1/8$ compared with both its lower and higher doping sides. My data roughly corresponds to what expected from single electron bands calculations in the tight binding approximation (white, dashed line in figure 5.6 (a)). Besides, from my data, it is difficult to tell a significant difference between the FS obtained at 5K below T_c and 55K above T_c . Although my finding suggests that the (π, π) shadow band might not be directly connected with the stripe order as previously suggested [Cha08], it does not preclude the connection of the stripe order with the mysterious normal-state properties of underdoped cuprates. The band structure reconstruction due to the fluctuating stripe order necessarily produces shadow bands at momentum locations that are determined by, among others, the incommensurate ordering wave vectors. However, because of the short-range and fluctuating nature of the order, these shadow bands could lack intrinsic spectral weight and appear poorly defined in momentum space, and thus are hard to detect [Kiv03, Voj09]. In figure 5.5(a), we show the normal state ($T>T_c$) energy momentum distribution maps taken in the nodal direction of the momentum space. The corresponding EDC and MDC are shown in figure 5.5 (b) and 5.5 (c). In EDC, we can clearly see the sharp quasi-particle peak along the nodal direction and gapless feature near Fermi level indicate as E_F in figure 5.5(b). By fitting the MDCs (see figure 5.5(c)) using a Lorentzian function and plotting the positions of the MDCs maxima as function of binding energy, the dispersion can be extracted, as shown in figure 5.7 (a).

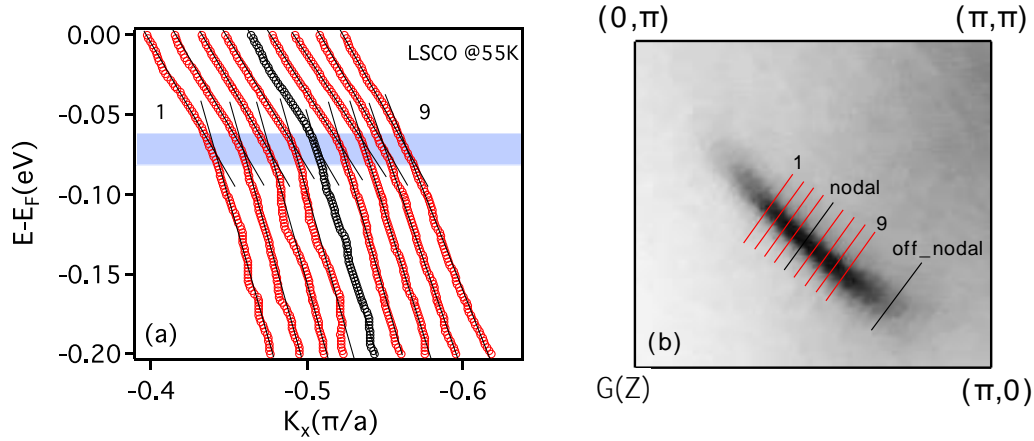


Figure 5.7 (a) Energy-momentum dispersions cuts near the nodal region for LSCO at 55K. (b) Location of the dispersion cuts along the Fermi surface.

In figure 5.7, we show several ARPES cuts in the reciprocal space (panel (b), red segments, numbered), collected at 55 K in a normal state, with fine step of the polar angle. We extracted the electron dispersions by fitting the MDCs and the corresponding electronic bands are plotted as a function of $k - k_F$. Data on the dispersion were recorded with enough resolution so that one can easily identify a clear deviation from a linear trend, resulting in an apparent kink. The black straight lines on the dispersion indicate the approximate linear dispersion, extrapolated from the data before and after the kink. We can approximately determine the kink position, in energy and wave-vector, by the intersection of the two linear dispersions. One can see the kink structure locates around 70 meV and does not change too much as the momentum cut goes from the nodal direction (cut 5) toward the off-nodal region at the end of the Fermi arc (cut 1 and cut 9).

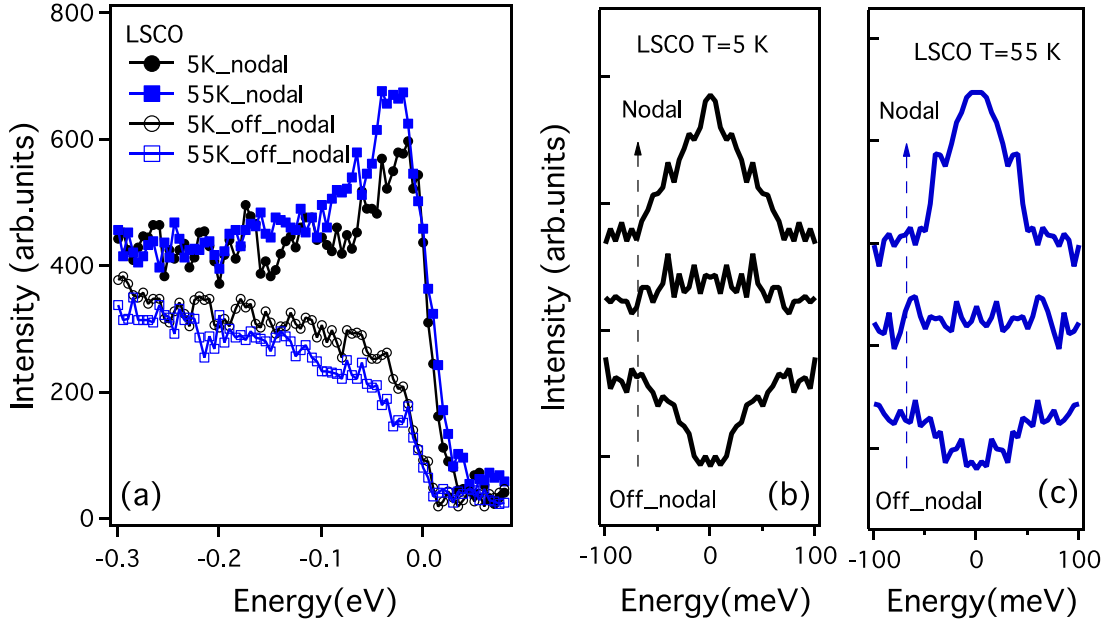


Figure 5.8 Superconducting gap and Pseudo-gap measured by ARPES. (a) Comparison of EDCs at K_F along the nodal with off-nodal direction below and above T_c for $\text{La}_{1.48}\text{Sr}_{0.12}\text{CuO}_4$. (b) and (c) The E_F -symmetrized EDCs from the nodal to off-nodal region obtained at $T=5$ K and $T=55$ K, respectively.

In figure 5.8, we compare the spectral line shapes of the nodal and off-nodal cut (depicted in figure 5.7(b)) on LSCO samples in the superconducting states and in the normal states. In panel (a), the EDCs along the nodal and off nodal were taken both below and above T_c ($T_c=31$ K). We can see a discernible quasi-particle peak in the superconducting state as well as in the normal state in the nodal region. In the off-nodal region, in contrast, the spectral weight near E_F is suppressed both below and above T_c , indicating a pseudo-gap behavior. There is no measurable spectral weight difference between data below and above T_c . In order to estimate the size of the energy gap at each K_F , we symmetrized the ARPES spectrum with respect to E_F to eliminate the effect from the Fermi-Dirac function [Nor98], and the E_F -symmetrized EDCs are shown in panel (b) and (c). We can observe that, for the LSCO ($x=1/8$) sample, the superconducting gap is opening when we move from the nodal to the off-nodal region at $T=5$ K. While for the case of $T=55$ K, in the normal state, we still see an almost comparable gap at the off-nodal region, suggesting of a pseudo-gap opening. The spectra evolution with temperature shown in figure 5.8 (c) demonstrates that the off-nodal pseudo-gap persist deep into the LTO phase. Our observation is consistent

with the report of Ref. [Yos16], which also show that this off-nodal pseudo-gap is sensitive to the doping level and exist at a small range of 1/8 doping.

5.3.2 The LNSCO results at the critical doping $x = 0.12$

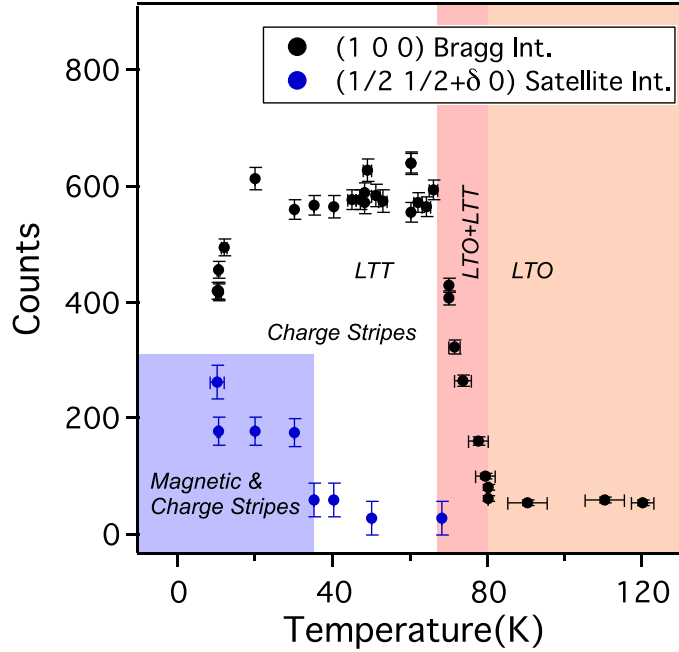


Figure 5.9 Phase diagram of $\text{La}_{1.48}\text{Nd}_{0.4}\text{Sr}_{0.12}\text{CuO}_4$ determined by neutron scattering data: the temperature dependence of the superlattice peak intensities. Blue filled circles: magnetic superlattice peak at the $(1/2, 1/2+\delta, 0)$, $\delta \sim x \sim 0.111$; Black filled circles: $(1,0,0)$ structural peak allowed only in the LTT phase.

In figure 5.9, I show my neutron scattering data on the LNSCO sample. We observe the intensity of the Bragg reflection $(1\ 0\ 0)$, which is forbidden in the Low Temperature Orthorhombic (LTO) state but allowed in the Low Temperature Tetragonal (LTT) one, set in at $\sim 80\text{K}$ and saturate at $\sim 70\text{K}$. At this temperature, the charge modulations (stripes) are known to set in [Tra95]. Below 35K , we observe an additional intensity on the satellite of the magnetic Bragg reflection at $(1/2, 1/2+\delta, 0)$ which is associated to scattering from the magnetic stripes. Therefore, we can identify four different phases on this LNSCO samples with three temperature transitions, namely superconducting states below $T_c \sim 4.6\text{K}$, magnetic stripes states below $T_{\text{magnetic stripes}} \sim 35\text{K}$, LTT phase below $T_{\text{LTO_LTT}} \sim 70\text{-}80\text{K}$ and LTO phase above. As CASSPIOPEE cryostat is limited to 5K , we could not go below than T_c

(~ 4.6 K). In this thesis, we performed our ARPES measurements of the LNSCO sample at three different temperatures ($T=9$ K, 55 K and 90 K), to investigate the magnetic stripes phase, charge only stripes phase, and the normal phase.

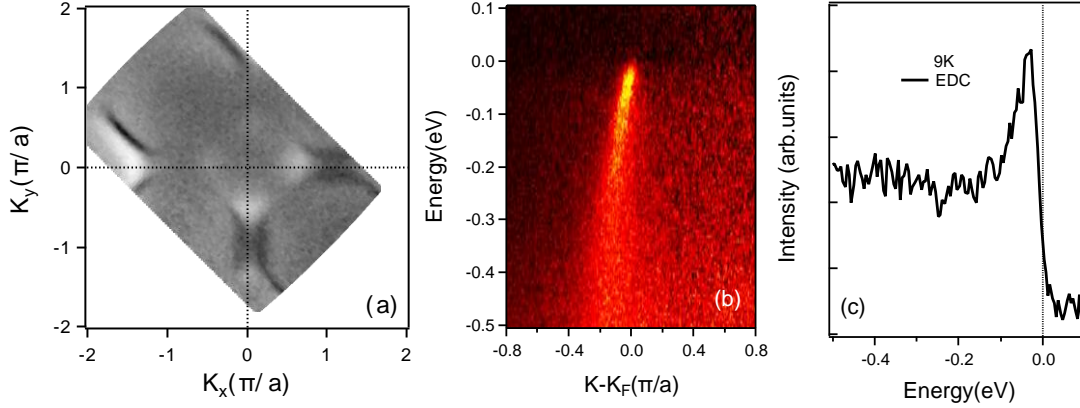


Figure 5.10 (a) Experimentally obtained FS of $La_{1.48}Nd_{0.4}Sr_{0.12}CuO_4$ at 9 K. Spectral weight integrated within ± 10 meV of the Fermi level, as a function of k_x and k_y . (b) Energy momentum distribution map of 1/8-doped LNSCO taken with 55eV along the nodal direction. (c) EDC of spectral intensity at k_F integrated with in ± 0.01 Å.

Figure 5.10 shows the Fermi surface of the 1/8-doped LNSCO at 9 K. The FS clearly displays four hole-like pockets corresponding to the CuO_2 planes. The nodal cut spectrum is shown in panel (b), where the dispersive features are clearly visible. And in panel (c) we can see the EDC obtained at k_F , where the sharp QP peak is clearly distinguishable.

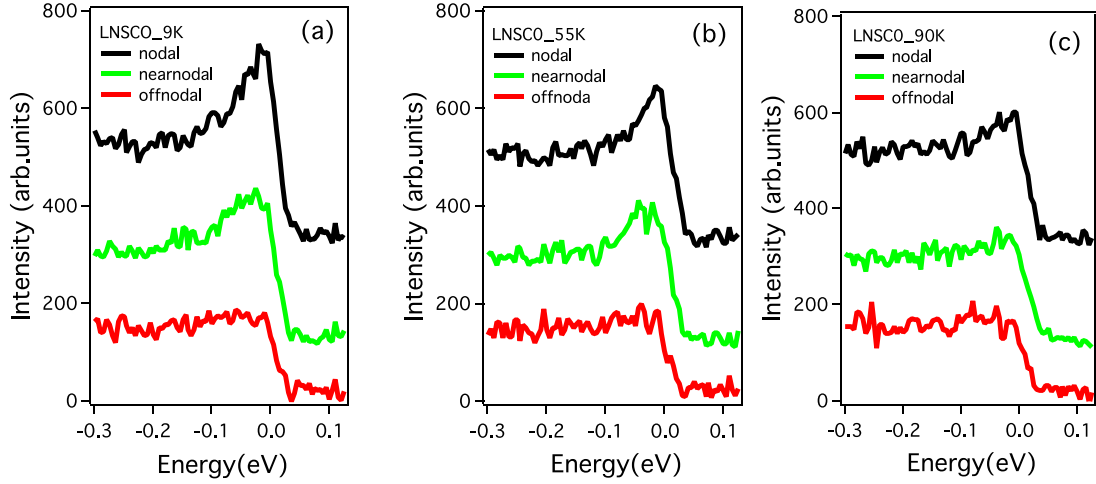


Figure 5.11 Temperature and momentum dependences of EDCs. The nodal, near- and off-nodal EDCs acquired at 9K (a), 55K (b) and 90K (c).

In figure 5.11, we show EDCs for several positions of the ARPES cuts in the reciprocal space, from nodal region to off-nodal region, for different temperatures on 1/8-doped LNSCO samples. In these data, the EDC shows a fairly weak QP peak with high background level at the off nodal direction, at all of the three temperatures measured. When moving towards the nodal point, the QP peak intensity evolves and gets sharp, especially for the low temperature case. This evolution of the QP peak as function of k-momentum is consistent with general observations: the spectral weight has a maximum near the node and drops off rapidly when approaching the antinode where it is suppressed and finally vanishes, resulting in a broad line-shape with a weak shoulder near E_F . On the other hand, the nodal QP peak seems to be suppressed and broadened as the temperature increase. We can see a sharp peak of the nodal quasi-particle at 9 K in magnetic-stripe phase (below $T_{\text{magnetic stripes}}$), a clear one in the charge only stripes phase at 55 K ($T_{\text{magnetic stripes}} < T < T_{\text{LTO-LTT}}$) and weak remnant still be observed at 90 K above the $T_{\text{LTO-LTT}}$ in the normal phase. This shows that the nodal quasi-particles are still present, in the stripe ordered states, and even in the normal state. However, if we move away from the node, the nearnodal quasiparticle peak show a strong temperature dependent and the peak is almost vanish at $T=90$ K in the LTT phase. While the quasi-particle peak disappears in the off-nodal region, at all temperatures.

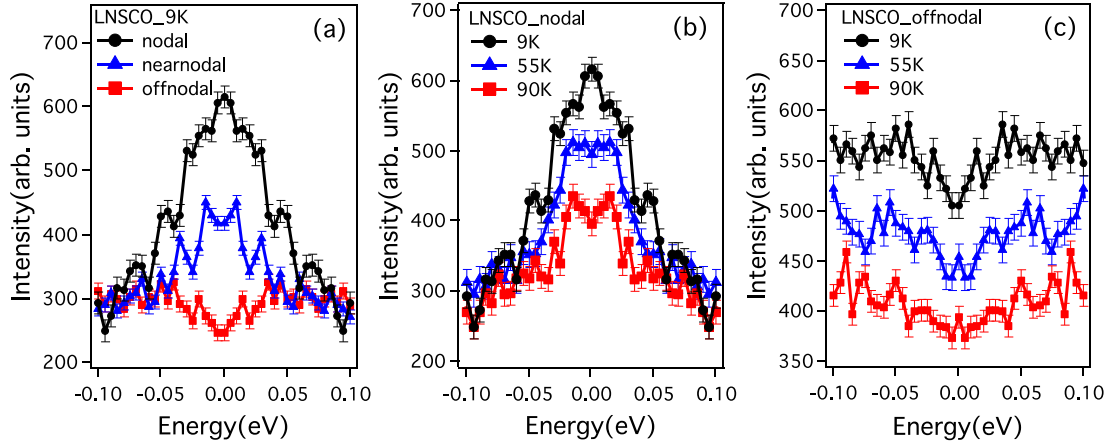


Figure 5.12 Symmetrized EDCs to estimate the gap size. (a) Pseudo-gap observed at off-nodal direction at 9 K. (b) Nodal pseudo-gap opens at 90 K. (c) Off-nodal pseudo-gap remains open even at $T = 90$ K.

Despite the evolution of the low-energy spectral weight along the FS, the QP peak maintains a distinct structure in momentum space, which gives the possibility to determine the peak position. For example, as shown in figure 5.11(a), at 9 K, we easily see that the peak position tends to move towards higher binding energy indicating an opening of the pseudo-gap with a maximum at the off-node. The raw symmetrized EDCs of LNSCO are shown in figure 5.12. In the left panel, for $T=9$ K, we can see the opening of the pseudo-gap as the momentum cut goes from the nodal direction toward the off-nodal region at the end of the Fermi arc. If we follow the temperature evolution of the two momentum cuts along the nodal and off-nodal direction, as shown in the middle and right panel, interesting results are observed. As showing in figure 5.12 (b), we can see that, at the nodal direction, a gap opens above 55 K and can persist up to 90 K. This suggests that the pseudo-gap can exist in nodal region, and similar results were reported on the other under-doped cuprates [He09] [Zho15]. One possible interpretation of our observation is that the pseudo-gap can exist in the nodal region when the superconductivity is suppressed owing to the loss of phase coherence, as claimed by He *et al.* [He09]. The other possibility is that the nodal gap is induced by the incommensurate diagonal spin density modulation as reported in Ref. [Zho15]. In the off-nodal region, the gap evolution in temperature is not as clear using the approximate EDCs symmetrized analysis as in ref [Mat15] and [Yos16]. But, we can still determine that the off-nodal pseudo-gap can persists up to

90 K in the LTO states. As previous reports show that static stripes appear only in the LTT phase and disappear in the LTO phase [Chr07, Tra95, Tra96], the off-nodal pseudo-gap seems not directly related to the spin and charge long-range order observed by neutron diffraction experiment. Recent reports suggest that the antinodal pseudo-gap is likely due to ordering rather than pairing as the near nodal pseudo-gap [Reb14]. To confirm that a gap really exist in the nodal direction above T_{LTO_LTT} , and close entering the magnetic stripe phase, need data set with higher statistics.

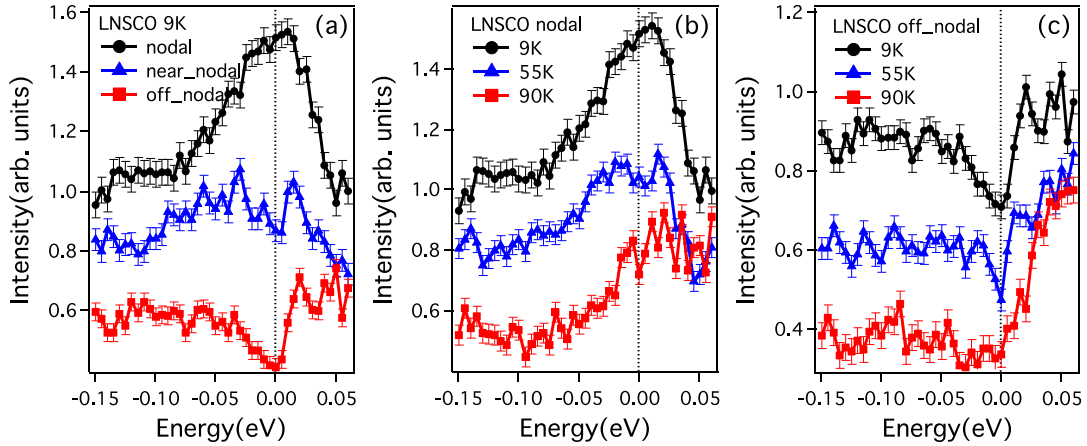


Figure 5.13 Temperature evolution of EDCs divided by the energy-resolution convoluted Fermi function at different temperatures.

To help our analysis, we have applied another approximate method, which is commonly used in the ARPES SC gap studies. Instead of symmetryzation, the raw spectra are divided by the energy-resolution convoluted Fermi function at the measurement temperature (FD-division) to remove the effect of the Fermi cutoff. Despite its complexities (getting the right Fermi function), it has advantages over the symmetric assumption. The momentum and temperature evolutions of gap obtained with the FD-division analysis are shown in figure 5.13, which is consistent with the result analyzed by symmetryzation method. At low temperature $T=9$ K in figure 5.13(a), the peak is at E_F on the nodal direction, indicating that a gapless excitations appear on the Fermi arc when the temperature is slightly higher than T_c . However, when we move out of the nodal cut, the peaks are visible below E_F , a pseudo-gap appearing at the near- and off-nodal direction at 9 K. In figure 5.13(b) and (c), the contrast of the temperature dependence of the nodal and off nodal gap analysed with

the FD-division method is shown. Due to the low flux of the incident photons during this measurement, we didn't obtain a statistic good enough to extract the effective gap size. But, we can see the spectra at the nodal direction is sensitive to the temperature, a finite nodal pseudo-gap is observed above 55K and it seems persist up to 90 K as shown in figure 5.13 (b). This observation of nodal pseudo-gap is quite similar to the Ref. [Mat15], where the authors also show a clear pseudo-gap of 5meV at nodal region. While as shown in figure 5.13(c), at the off nodal direction close to the end of arc, the pseudo-gap is not sensitive to temperature and appears at all temperatures.

Razzoli *et al.* [Raz13] studied the gap function of under-doped LSCO by ARPES using the symmetryzation and Fermi Function Divided method in EDCs at K_F , and observed a diagonal gap below as well as above $T_c=20$ K and finally it disappears at about 80K. Moreover, Kondo *et al.* [Kon15] also report that the nodal gap was observed at optimal ($T_c=92$ K) Bi-2212 samples, and such nodal gap can persist up to above T_c around 135 K. On the other hand, on the antiferromagnetic LSCO samples, Drachuck *et al.* [Dra14] found that the nodal gap opens at the onset temperature of spin density wave (SDW) ordering at 30 K. According to these results, we could conclude that our observation suggests that the low energy electronic excitation spectra of LNSCO are gapped along the entire underlying Fermi surface above 55 K, although the interpretation of such gap is not yet clear.

5.3.3 The LBCO results at doping $x = 0.14$

5.3.3.1 Temperature and angle resolved dependence of the pseudo-gap

$La_{2-x}Ba_xCuO_{4+\delta}$ [Mic85] is the first cuprate HTS discovered, but no single crystal was available until the early 2000's. The LBCO samples ($T_c=18$ K) I studied in this thesis are cleaved from a bulk crystal prepared by TSFZ method. The LTO-LTT transition in this sample was measured by observing the splitting of the (3 1 0) Bragg reflection as temperature is raised at $T_{LTT} = 34.0 \pm 2.5$ K [Shu07].

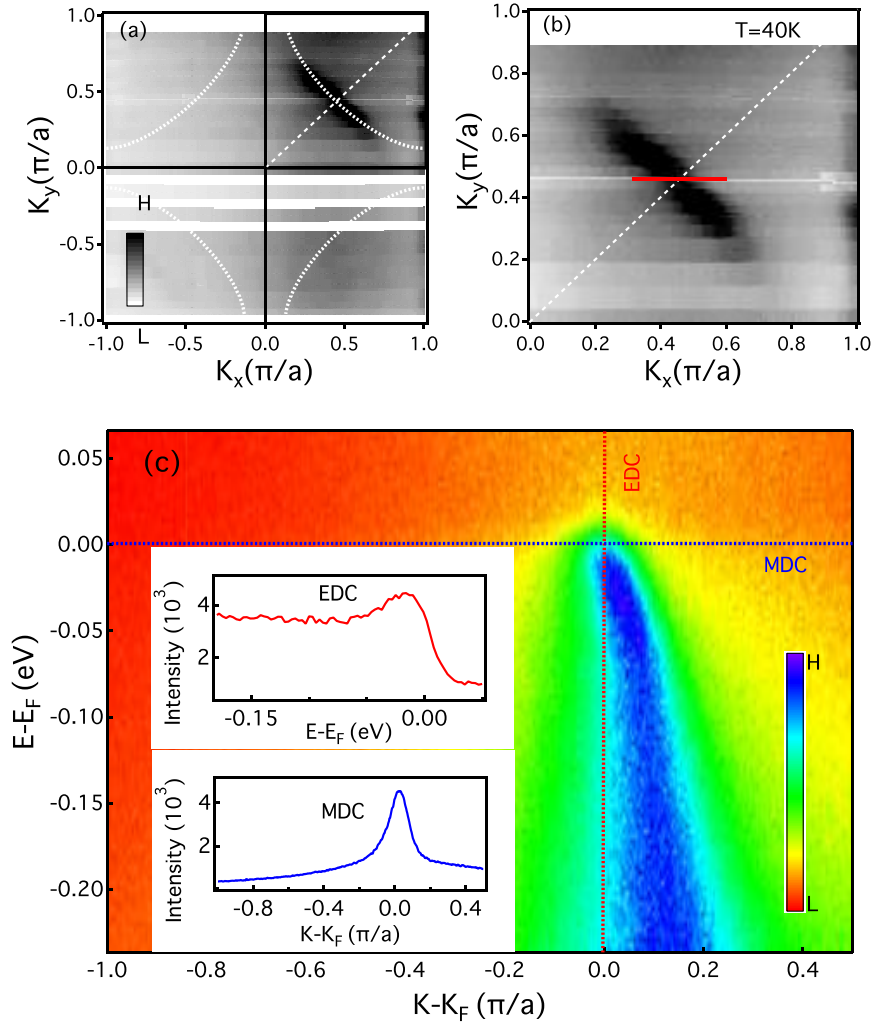


Figure 5.14 Angle-resolved photoemission spectra and the Fermi surface of our $La_{2-x}Ba_xCuO_{4+\delta}$ ($x \sim 0.14$). The data in the picture were taken with photon energy $h\nu=55$ eV at $T=40$ K. (a) Fermi surface map having a large momentum coverage. The dashed curves represent the tight binding Fermi surface results from a global fit to the data as guide to the eye. (b) The fine quadrant FS map of the first BZ depicted as the black box in (a). (c) Photoemission intensity from LBCO sample as a function of binding energy along the momentum line indicates in (b). Inset upper panel: EDC of spectral intensity at K_F integrated with in $\pm 0.01\text{\AA}$. Inset lower panel: the MDC of the spectral intensity at E_F integrated with in ± 5 meV.

The overall shape of the FS collected on LBCO at 40 K is shown in figure 5.14(a), while figure 5.14 (b) shows the data collected with fine steps of the polar angle. The measurement is in agreement with the results of Ref. [He09], and roughly corresponds to what expected from single electron bands calculations in the tight binding

approximation (white, dashed line in figure 5.14 (a)). Figure 5.14 (c) plots a typical cut of ARPES intensity as a function of energy and momentum along the nodal direction; the position of the momentum cut is labeled in figure 5.14 (b). In its insert, we show the EDC and MDC of spectral intensity. I extracted the electron dispersion by fitting the distribution of the quasi-particle over constant binding energy (MDC) to a sum of two pseudo-Voigt functions, one simulating the background and the second the signal.

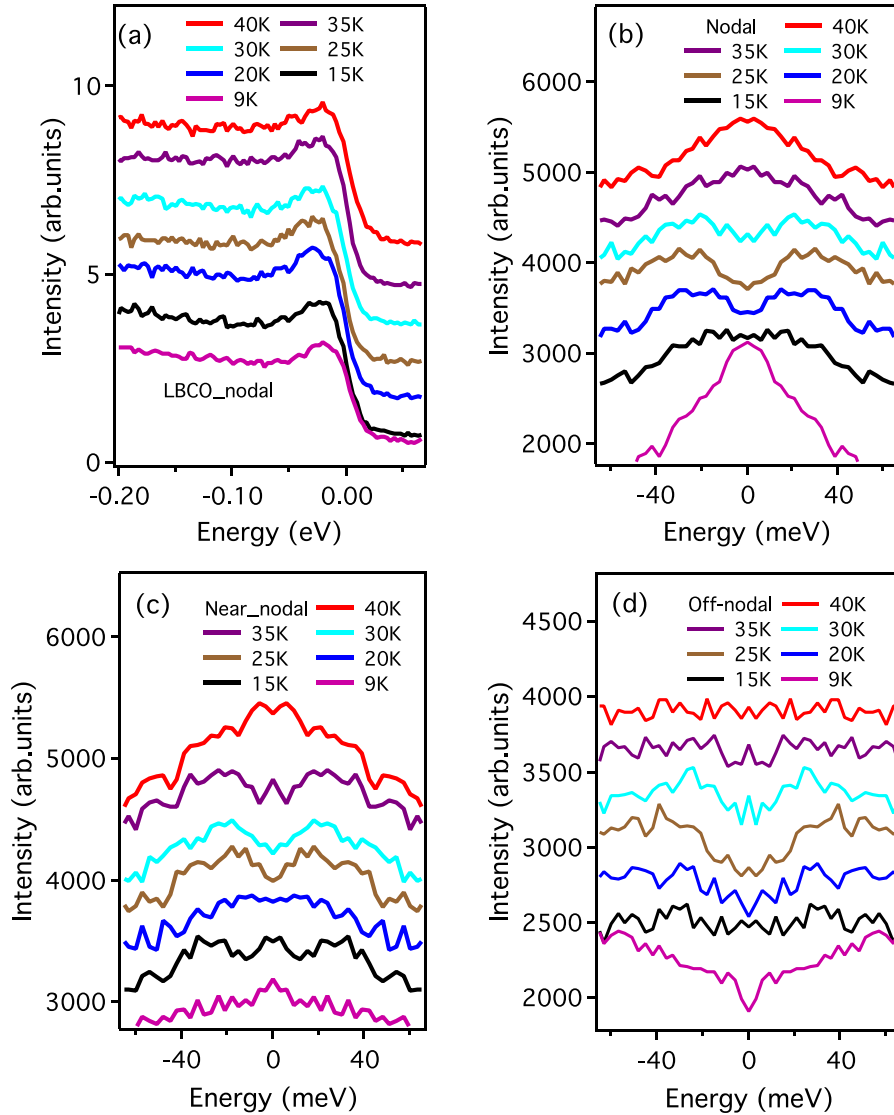


Figure 5.15 (a) Energy distribution curves of LBCO acquired at nodal direction with different temperature (15K-40K). (b)-(d) Symmetrized EDCs obtained at nodal, near-nodal and off-nodal direction as function of the temperature.

The same gap analysis previously described for the LNSCO experiment, was performed to study the gap of LBCO samples. In figure 5.15 (a) and (b), the EDCs along the nodal direction and the raw symmetrized EDCs are shown as a function of temperature, respectively. As we can see from figure 5.15 (a), the quasi-particles peak is not as sharp as the one I measured in LNSCO samples. We do not see much difference in the intensity when the temperature changes from the low temperature (superconducting state) to the higher temperatures (normal state). But, on a very close look at the intensity by FD-division analysis, the amplitude of quasi-particle peak is

slightly stronger in the superconducting states than that the one in the normal states (see Figure 5.17 (b)). On the other hand, as shown in figure 5.15 (b), the raw symmetrized EDCs demonstrate the existence of the nodal gap structures and their variations with temperature.

The detailed temperature evolutions and the momentum cut dependence are shown in figure 5.15 (b-d), where I plotted the raw symmetrization EDCs as a function of temperature for the nodal in (b), near nodal in (c) and off-nodal cuts in (d). As shown in figure 5.15 (b), a single peak feature can be observed at the SC states at $T=9$ K and 15K, showing gapless nodal at temperature just below $T_c=18$ K. When the temperature is increased to 20K, we can clearly see that two peaks, instead of one observed at the Fermi energy and lower temperature, appears at below and above Fermi energy and a pseudo gap opens. This pseudo gap persists up to 35-40 K where it finally closes. A similar trend was found for the near-nodal and off-nodal region as shown in figure 5.15 (c) and (d). Our observation indicate that we can see a gap opening at the nodal region in the 1/8 doped LBCO ($T_c=18$ K) and the temperature dependence indicates the pseudo-gap opens at temperature slightly above T_c and closes at around 40 K which is close to the LTO-LTT transition temperature $T_{LTT}=34.0\pm 2.5$ K.

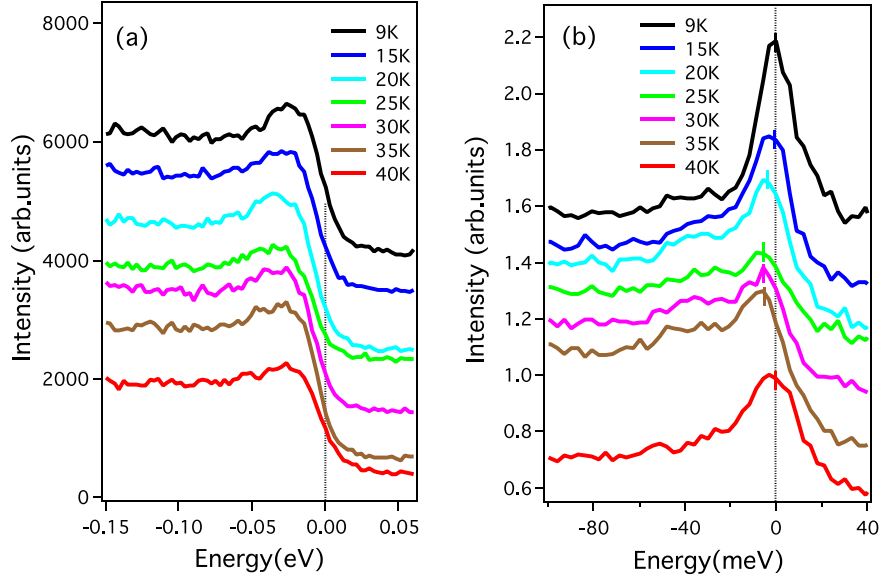


Figure 5.16 The EDCs at k_F on the nodal direction for LBCO. (a) The EDCs were obtained at row ARPES data and (b) raw ARPES data divided by the energy-resolution convoluted Fermi function for all measured temperatures.

To clarify the anomalous gap feature above T_c , here we investigate the Fermi-divided EDCs along the nodal cuts as a function of selected temperature. In figure 5.16 (a) and (b), we plot the EDCs at the k_F obtained from the raw data and from the FD-division analysis as a function of temperature, respectively. A general observation in cuprates is that when T_c is crossed by decreasing the temperature, EDC peaks near the k_F along an off-nodal cut sharpen. This behavior was also observed in our ARPES spectra for LBCO ($x=0.14$) along the nodal cut. In figure 5.16 (b), the EDC peak width at 9 K (below T_c) is considerably smaller than when the spectrum is measured above T_c , which indicates the change in the peak width is associated with the superconducting transition. At the same time, in the superconducting states, a single peak feature is observed, showing a gapless nodal point. But a finite gap opens when the temperature is increased, and the nodal-gap size reaches the maximum around 25 K and disappears at around 40 K, giving a consistency with the result obtained by the symmetrization method. Actually, a similar result was found on 1/8-doped LBCO by He, R. *et al.* [He09], they did show a gap at the nodal region. Our observation on the nodal region at LBCO also shows a gap-like structure even above T_c . This result is actually extremely surprising, considering the widely accepted view that the pseudo-gap is null at the nodal direction as the pseudo-gap should be of the same d-wave

format as the superconducting gap.

5.3.3.2 Angle resolved dependence of the kink and possible scattering kinetics

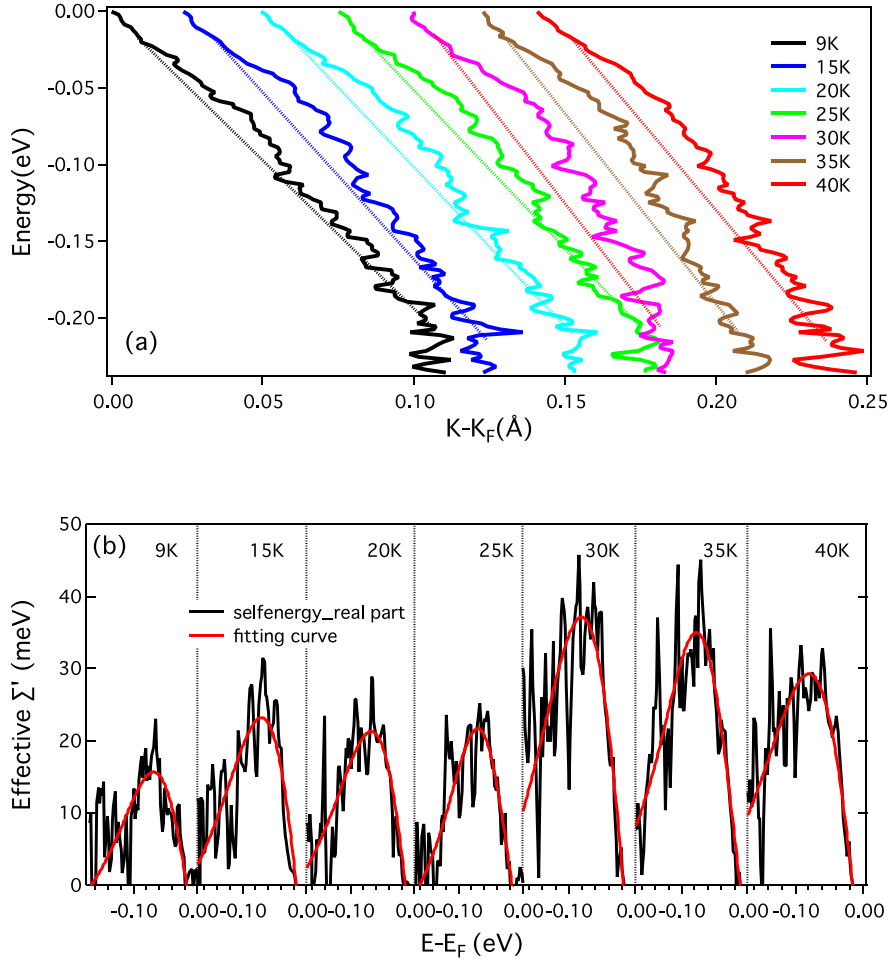


Figure 5.17 (a) The MDC-derived dispersions (energy vs. momentum) for 1/8-doped LBCO at the nodal direction for different temperatures. The dotted lines indicate the linear bare bands. (b) Real part of self-energy, determined from the dispersion deviation from the straight line.

According to the Tr-ARPES results on BSCCO samples [Ish16], the ultrafast loss of superconducting gap is accompanied by spectral broadenings and weight redistribution occurring within the kink binding energy. In order to find out if the pseudo-gap also associated with the kink, we performed self-energy analysis of the ARPES data along the nodal direction, where the signal intensity is strongest and there is no significant matrix element variation. Since our results does not depend on the functional form of the bare band, we show here only the results based on the linear

bare band, but the results were also checked against a quadratic bare band. In this chapter, these effective bare bands are determined by interpolating the data at $E - E_F < 140 \text{ meV}$ and the ones close to E_F . The energy-momentum dispersions derived from the momentum distribution curves (MDCs) along the nodal direction taken with 55 eV photons at different temperature are shown in figure 5.17 (a). Nodal band dispersions follow a straight line from -0.3 eV to -0.15 eV. Clear deviation of the band dispersion away from a straight line near 70meV, corresponds to the kink feature well known from previous studies in 214 cuprates but not yet reported in LBCO.

To precisely establish the kink energy is of fundamental importance in identifying the nature of the bosonic excitation that couple to the electron. To this aim, we deduced the real part of the self-energy $Re\Sigma'$, as shown in figure 5.17 (a), by subtracting featureless linear bare bands (dotted line in figure 5.17 (a)) to the measured dispersions. We estimated the kink energy as the energy giving the peak maximum of the $Re\Sigma'$, which was obtained by fitting the top portion of the $Re\Sigma'$ with a sum of two Cauchy-Lorentz functions, in order to empirically reproduce its asymmetric shape, the peak position is consistent with single Lorentz fitting but the overall spectral weight is better reproduced. Figure 5.17 (b) shows the contribution of bosonic modes below 0.2 eV to the real part of self-energy ($Re\Sigma'$) extracted using the linear bare band connecting MDC peak position at 0.2 and 0 eV binding energy. Our $Re\Sigma'$ therefore includes all the bosonic modes below 200 meV. We can see the peak broaden, or shift to higher binding energy, or the existence of two peaks as reported by He *et al.* in Ref. [He13] where they claim two energy scales exhibit distinct momentum dependence. In our case, it is difficult to distinguish if there exist two energy scale peaks since we didn't have enough statistics. On the other hand, if the filling of the gap with increasing temperature is a generic feature of the cuprates as reported by Reber *et al.* in Ref. [Reb15], we should see a behavior fully consistent with the increase of self-energy with temperature. Here, an apparent strength increased with the temperature can be observed, but the expected changes with various temperatures as we have seen in the gap analysis do not occur. Our results on the LBCO, at least for the nodal direction, don't show the consistent observation with the previous the report.

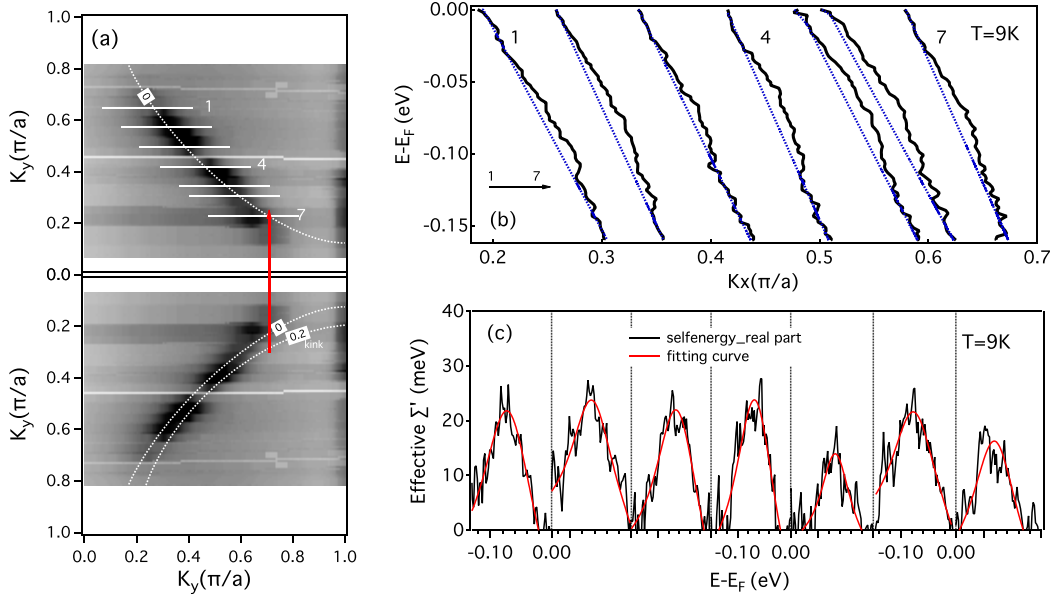


Figure 5.18 (a) The measured FS of LBCO at 9 K with the momentum location of cuts across the Fermi arc region, labeled from 1 to 7. A specular replica is shown in order to visualize the possible scattering vectors connecting different sheets of the Fermi surface parallel to (100). (b) Band dispersions for different cuts obtained by MDC fits of the data in the ARPES map, as given in (a). The dotted lines indicate the linear bare bands. (c) Real part of self-energy, determined from the dispersion deviation from the straight line. The corresponding kink energy can be extracted from the peak position of the $Re\Sigma'$ as a function of momentum cuts.

ARPES measurements in LBCO close to the 1/8 doping have been already published by He and coworkers in Ref. [He09], with a focus on the details of the superconducting and pseudo-gap along the Fermi surface. However, no details were given about the kink position in the electronic bands, and its wave-vectors dependence. In figure 5.18, panel, (a), we show Fermi arc at $T = 9$ K, mirrored across the Zone Boundary, with the position of the measured ARPES cuts, from which we extracted the band dispersion, shown below. We also represent a possible exchanged q vector connecting the tip of the Fermi arcs along the (0 1 0) direction to the surface at the average energy of the kink. As shown in figure 5.18 (b), the energy-momentum dispersion curve shows an abrupt slope change near 70 meV. The kink structure does not change too much as the momentum goes from the nodal direction (cut 4) toward the anti-nodal region at the end of Fermi arc. For each dispersion, we obtained the $Re\Sigma'$ determined from the dispersion deviation from the straight line. We can see in

figure 5.18 (c), the energy position of the maximum of $Re\Sigma'$ is almost constant for different cuts, within a few meV range around approximately 70 meV, with a dispersion comparable with the error bar of the measure. The results of the obtained the $Re\Sigma'$ maximum position are present in figure 5.20, which shows the kink energy for each momentum space cut.

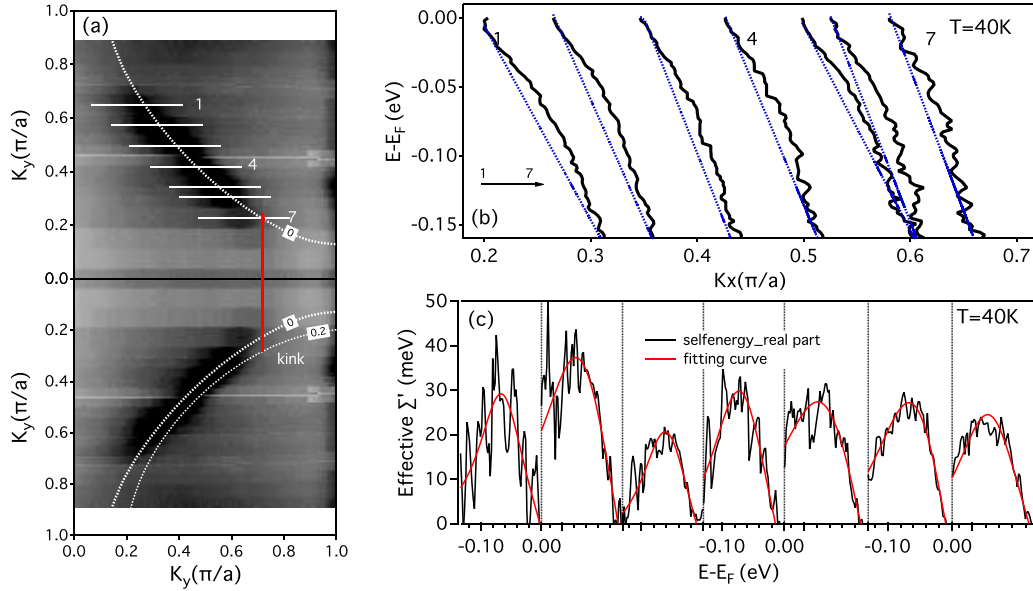


Figure 5.19 (a) The measured Fermi surface of LBCO at 40 K. (b) Band dispersions for different cuts obtained by MDC fits of the data in the ARPES map at 40 K, the precise location of the cut are given in (a). The dotted lines indicate the linear bare bands. (c) Real part of self-energy, determined from the dispersion deviation from the straight line.

The same analysis was done on the data obtained at 40 K, and the results are shown in figure 5.19. As we can see from figure 5.19, compared to the low temperature, the kink structures are still visible at 40 K, with a larger signal to noise on the data that were obtained at the temperature above T_c . At the same time, although there is a larger oscillation and error bar at 40 K (see figure 5.20 (b)) than the ones at 9 K (see figure 5.20 (a)), the kink energy extracted from the band dispersions are almost constant at 70 meV at both 9 K, which is below T_c (panel a) and 40 K, which is above.

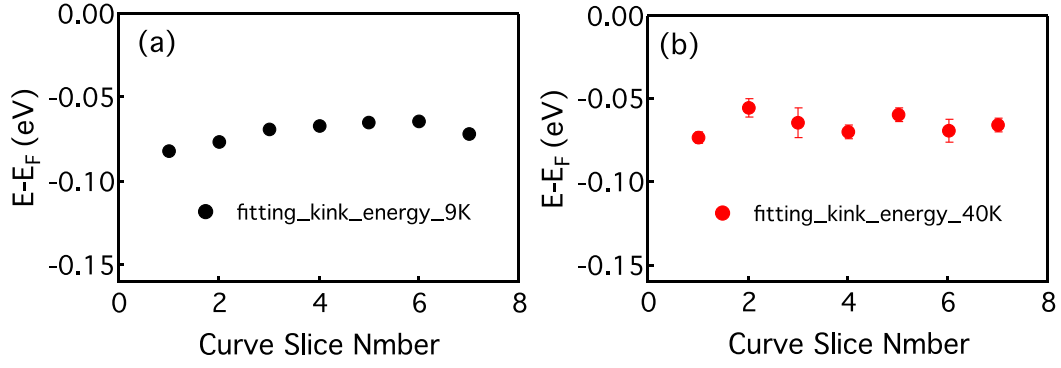


Figure 5.20 Kink energy as a function of momentum cuts of LBCO at 9 K (a) and 40 K (b) obtained by fitting the real part of self-energy.

By extracting the wave-vectors of the kink for each momentum cuts we can derive the exchanged q vector of scattered phonon, assuming a given electron-phonon process. In our analysis we choose a phonon exchanged with a momentum parallel to the antinodal direction. This corresponds to the hypothesis of an electron-phonon scattering process with a Δ_1 phonon modes as in figure 5.21.

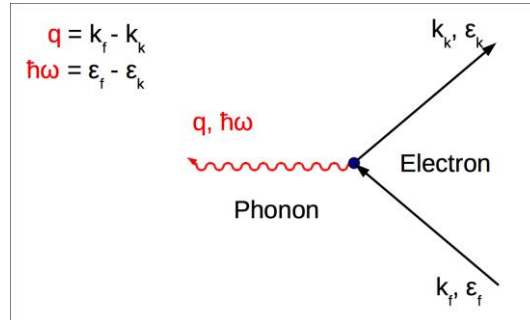


Figure 5.21 Sketch of the kinetics of the electron phonon scattering process.

In this hypothesis the process would scatter an electron propagating with the momentum $\hbar k_k$ on the isoenergetic surface at the energy of the kink maximum ϵ_k , adding to it the momentum of the phonon $\hbar\omega_{ph}$, that is parallel to the anti-nodal direction $(\pi, 0)$ or $(0, \pi)$ in this hypothesis, and energy the $\hbar k_{ph}$ of such phonon, on the condition that only the process ending in a Fermi surface at $(\hbar k_F, \epsilon_F)$ are allowed, as in figure 5.18 panel (a), i.e.

$$\begin{cases} \hbar\omega_{ph} = \epsilon_F - \epsilon_k \\ \hbar q_{ph} = \hbar k_F - \hbar k_k \end{cases}$$

In figure 5.22, we superpose the position of the scattered phonon deduced from the kink in the energy-momentum electronic dispersion curve, with the Δ_1 phonon modes. The wave vector of such phonon, scattered from electrons, is calculated as the difference between the wave-vector of the kink and the one of the nearest Fermi surface sheet connected by a vector parallel to a^* (or b^*). In figure 5.18 (a) such process is represented for the band close of the end of the Fermi arc and a phonon scattering vector parallel to b^* , that it is aligned to k_y in this image. Note that in the phonon dispersion the wave-vector are represented in units of $2\pi/a$, hence a factor 2 with the values of k_F and the wave-vector k_k of the kink deduced from the position of the maximum of $\text{Re}\Sigma'(\omega)$ in the (k_x, k_y) space that is conventionally in unit of π/a .

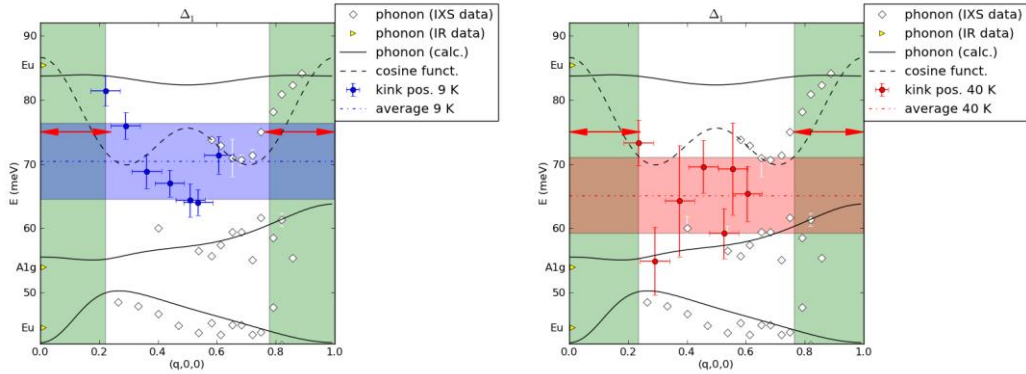


Figure 5.22 The position of the kink, extracted from the analysis of the ARPES data, compared to the phonon dispersion at the same doping (\diamond and continuous lines, from Ref. [Das08], \triangleright from Ref. [Mos90], see text) in the extended Brillouin Zone representation along $(1\ 0\ 0)$. Continuous lines are lattice dynamics calculations, while the dashed black line is an analytic function, roughly following the Cu-O bond stretching dispersion. The green shadowed areas indicate the range of q-vectors that are too short to connect Fermi arcs. The smaller possible scattering vectors connecting the edges of the Fermi arc, and parallel to $(1\ 0\ 0)$, are shown as in figure 5.18(a) by a red arrow. (\bullet) Symbols represent kink positions from the ARPES measurements at 9 K (blue, left panel) and 40 K (red, right panel). Dash-dot lines correspond to the average energy position of the kink at 9 K (blue, left panel) and 40 K (red, right panel).

The error bars of the phonon position extracted from the ARPES data are rather large in comparison to the ones of the phonons from IXS, yet its position match quite well with the dispersion of the Cu-O bond stretching modes, *i.e.* the modes starting with

E_u character at the zone center at about 83 meV, and softening to about 70 meV, roughly corresponding to the kink energy in our data set. Note also that the region of the Fermi arc, where we can observe the kink, allows, in this hypothesis, process with a scattered wave-vector that corresponds to the region where the mode is soft for these Cu-O bond-stretching mode. The energy would match also the Δ_1 mode with character A_{1g} at Γ in the same panel. However, only the Cu-O bond stretching undergoes a marked softening with doping, which is not observed for the A_{1g} one.

5.4 Discussion of the results

Our main result is the temperature dependence of the pseudo-gap near nodal in LBCO, showing an apparent link with the LTT-LTO transition, that seems to supports a link with charge modulation instead of SDW, in contradiction with other works [Dra14]. We show that the gap open below the LTT-LTO transition, suggesting that it originate from charge-modulation symmetry breaking, which appear at the same temperature [Shu07]. Surprisingly, this is the first report, to our knowledge, of such effect, which does not appear in the extensive literature on ARPES in cuprates. In order to confirm this result, we tested a similar compound, LNSCO, which, puzzlingly, seems not to show the same behavior, but the data quality in that case are not as good, so we think further studies are needed to confirm the surprising closure of the near-nodal pseudo-gap when reaching the LTT phase in LBCO. Another interesting possibility could be that here T^* is around 40 K in our sample, and accidentally close to the LTT-LTO transition temperature.

Concerning the kink, we confirm in LBCO the observation of a correspondence between anti-nodal wave-vector connecting the FS sheets and the energy of the kink with the energy dispersion of the Cu-O bond stretching mode in the same system, as already observed for LSCO and Bi2201. Again, we can not reproduce the same results on our LNSCO sample. This is difficult to understand as at this doping and substitution level the effect on the Cu-O bond-stretching mode is maximum [Rez06]. In that case, we do not think our data are particularly hampered by the statistics, putting in question the link between Cu-O bond stretching mode phonons and the kink cited above. We note however that the effect of charge modulation could be complex. Also, model calculation [Rös04] suggests that the apparent strength of this interaction

strongly depends on the property studied, and therefore the effect can be very different for ARPES in comparison to direct phonon anomalies measurements with direct probes as inelastic scattering. In any case, this very interesting result calls for further investigation in this and similar system to confirm it.

The initial plan of this work was to compare the electron-phonon coupling strength λ obtained from the ratio of the velocities of the bare and dressed carriers [Lan01] with the one obtained from the relaxation decay time constant of hot electron after pump excitation [Per07], as described in Chapter 1. However our first attempt of the latter experiment failed because of technical difficulties. But this is still a very interesting perspective that we hope we could perform in the near future. The work of this chapter must then be seen as a preparation background for such investigation.

Chapter 6

Conclusion and Outlook

We perform time-resolved photoelectron spectroscopy measurements of optimally doped $\text{Bi}_2\text{Sr}_2\text{CaCu}_2\text{O}_{8+\delta}$ (Bi-2212) and $\text{Bi}_2\text{Sr}_{2-x}\text{La}_x\text{CuO}_{6+\delta}$ (Bi-2201). The electron dynamics shows that inelastic scattering by nodal quasiparticles decreases when the temperature is lowered below the critical value of the superconducting phase transition. This drop in electronic dissipation is astonishingly robust and survives to photoexcitation densities much larger than the value sustained by long-range superconductivity. The unconventional behavior of quasiparticle scattering is ascribed to superconducting correlations that appear just after photoexcitation and extend on a length scale comparable to the inelastic path. In parallel to the QPs cooling, we analyze the shift and broadening of the quasiparticle peak. We propose that the time dependent shift may be a thermoelectric effect linked to the effective temperature of hot electrons just after photoexcitation.

In a second set of experiments, we employed narrow band probe pulses to resolve fine details on the spectral function as a function of temperature, photoexcitation density and delay time from the pump pulse. Our time resolved ARPES data of $\text{Bi}_2\text{Sr}_2\text{CaCu}_2\text{O}_{8+\delta}$, report a momentum-dependent collapse of the superconducting gap upon photoexcitation. The pairing amplitude becomes more robust when moving off the nodal direction. Interestingly, the QP relaxation develops a faster component at

the threshold fluence F_{pair} where the gap has fully collapsed. On the other hand, the hot electrons relaxation is still affected by the dynamical correlations of an incipient superconducting phase.

The comparison between the F_{pair} and the F_{phase} extracted by tr-THz suggested the existence a fluence regime when the Cooper pairs have survived, but without holding superfluid current. Nonetheless the measurement of F_{pair} and F_{phase} on the same sample and with the same source would be mandatory to draw out solid conclusions.

In chapter 5 we have presented ARPES data of the pseudo-gap near nodal in LBCO, showing an apparent link with the LTT-LTO transition, that seems to supports a link with charge modulation instead of SDW. We show that the gap open below the LTT-LTO transition, suggesting that it originate from charge-modulation symmetry breaking, which appear at the same temperature. There remain many problems to be solved in future to fully elucidate the properties of High-Tc cuprates. In order to understand the paring mechanism of the superconductivity, not only the universal feature of the high-Tc cuprates, but also the origin of the material dependent features such as the small pseudo, the nodal gap at low temperatures are needed to be clarified. The observation that the band structure of LBCO is affected by a renormalization that sets in prior to the 70 meV kink implies that the coupling strength associated with this interaction as derived the real part of the self energy. We were able to correlate this energy scale in the ARPES data to an observed the Cu-O bond stretching mode previously in the literature as well as in our own Neutron measurement. By combining the behavior of the imaginary part of the self energy observed in ARPES with the measured phonon spectrum, we confirm in LBCO the observation of a correspondence between anti-nodal wave-vector connecting the FS sheets and the energy of the kink with the energy dispersion of the Cu-O bond stretching mode in the same system, as already observed for LSCO and Bi2201.

In order to investigate the electron-phonon coupling in such striped superconductor, future Tr-ARPES experiments on the dynamics of the quasiparticles of the LSCO are suggested, where, the electron phonon coupling constant are determined form the electronic temperature decay time-constant τ , and compared to the one extracted from the kink strength.

Bibliography

- [All87] P. B. Allen, Phys. Rev. Lett. 59, 1460 (1987)
- [Arm10] N. P. Armitage, P. Fournier, R. L. Greene, Rev. Mod. Phys. 82, 2421 (2010)
- [Ave01] R. D. Averitt, G. Rodriguez, A. I. Lobad, J. L. W. Siders, S. A. Trugman, and A. J. Taylor, Phys. Rev. B 63, 140502 (2001)
- [Axe89] J. D. Axe, A. H. Moudden, D. Hohlwein, D. E. Cox, K. M. Mohanty, A. R. Moodenbaugh, and Y. Xu, Phys. Rev. Lett. 62, 2751(1989)
- [Ber64] C. N. Berglund and W. E. Spicer, Phys. Rev. 136, A1030 (1964)
- [Ber10] N. Bergeal, J. Lesueur, M. Aprili, G. Faini, J. P. Contour, and B. Leridon, Nature Phys. 6, 296 (2010)
- [Bey11] M. Beyer, D. St'adter, M. Beck, H. Sch'afer, V. V. Kabanov, G. Logvenov, I. Bozovic, G. Koren, and J. Demsar, Phys. Rev. B 83, 214515 (2011)
- [Bil11] L. S. Bilbro, R. Valdés Aguilar, G. Logvenov, O. Pelleg, I. Božović & N. P. Armitage, Nature Physics 7, 298–302 (2011)
- [Bov07] U. Bovensiepen, J. Phys.: Condens. Matter 19, 083201 (2007)
- [Bro14] Brouet, V. LPS igor procedures (2014), private communication
- [Can14] E. Canovi, P. Werner, and M. Eckstein, Phys. Rev. Lett. 113, 265702 (2014)
- [Car04] M. A. Carnahan, R. A. Kaindl, J. Orenstein, D. S. Chemla, S. Oh, and J. N. Eckstein, Physica C 408, 729 (2004)
- [Car09] E. Carpene, E. Mancini, C. Dallera, G. Ghiringhelli, C. Manzoni, G. Cerullo, and S. De Silvestri, Rev. Sci. Instrum. 80, 055101 (2009)
- [Cha08] J. Chang, Y. Sassa, S. Guerrero, M. Mansson, M. Shi, S. Pailhes, A. Bendounan, R. Mottl, T. Claesson, O. Tjernberg, L. Patthey, M. Ido, N. Momono, M. Oda, C. Mudry, J. Mesot, New J. Phys. 10 103016 (2008)
- [Cha12] J. Chang, E. Blackburn, A. T. Holmes, N. B. Christensen, J. Larsen, J. Mesot, Ruixing Liang, D. A. Bonn, W. N. Hardy, A. Watenphul, M. v. Zimmermann, E. M. Forgan and S. M. Hayden, Nature Phys. 8, 871-876 (2012)
- [Che93] C. H. Chen, S. W. Cheong and A. S. Cooper, Phys. Rev. Lett. 71, 2461–2464 (1993)
- [Chr07] N. B. Christensen, H. M. Rønnow, J. Mesot, R. A. Ewings, N. Momono, M. Oda, M. Ido, M. Enderle, D. F. McMorrow, and A. T. Boothroyd, Phys. Rev. Lett. 98, 197003 (2007)

- [Coh72] M. Cohen and P. W. Anderson, Comments on the maximum superconducting transition temperature. In *Superconductivity in d- and f-band Metals* (ed. Douglas, D. H.) 17–27 (American Institute of Physics, 1972)
- [Com14] R. Comin, A. Frano, M. M. Yee, Y. Yoshida, H. Eisaki, E. Schierle, E. Weschke, R. Sutarto, F. He, A. Soumyanarayanan, Yang He, M. Le Tacon, I. S. Elfimov, Jennifer E. Hoffman, G. A. Sawatzky, B. Keimer, A. Damascelli, *Science* 343, 390-392 (2014)
- [Cor11] R. Cortés, L. Rettig, Y. Yoshida, H. Eisaki, M. Wolf, and U. Bovensiepen, *Phys. Rev. Lett.* 107, 097002 (2011)
- [Cor99] J. Corson, R. Mallozzi, J. Orenstein, J.N. Eckstein, and I. Bozovic, *Nature* 398, 221-223 (1999)
- [Cil14] F. Cilento, S. Dal Conte, G. Coslovich, S. Peli, N. Nembrini, S. Mor, F. Banfi, G. Ferrini, H. Eisaki, M. K. Chan, C. J. Dorow, M. J. Veit, M. Greven, D. van der Marel, R. Comin, A. Damascelli, L. Rettig, U. Bovensiepen, M. Capone, C. Giannetti and F. Parmigiani, *Nature Communications* 5, p. 4353. (2014)
- [Dah05] Dahm, T., Hirschfeld, P.J., Scalapino, D.j. and Zhu, L. Nodal quasiparticle lifetime in cuprate superconductors. *Phy.Rev.B* 72,214512(2005)
- [Dam03] A. Damascelli, Z. Hussain, and Z. X. Shen, *Rev. Mod. Phys.* 75, 473 (2003)
- [Dal15] S. Dal Conte, L. Vidmar, D. Golez, M. Mierzejewski, G. Soavi, S. Peli, F. Banfi, G. Ferrini, R. Comin, B. M. Ludbrook, L. Chauviere, N. D. Zhigadlo, H. Eisaki, M. Greven, S. Lupi, A. Damascelli, D. Brida, M. Capone, J. Bonca, G. Cerullo, and C. Giannetti, *Nat. Phys.* 11, 421 (2015)
- [Das08] M. D’Astuto, G. Dhalenne, J. Graf, M. Hoesch, P. Giura, M. Krisch, P. Berthet, A. Lanzara, and Abhay Shukla *Phys. Rev. B* 78, 140511(R) (2008)
- [Dem99] J. Demsar, B. Podobnik, V. V. Kabanov, Th. Wolf, and D. Mihailovic, *Phys. Rev. Lett.* 82, 4918 (1999)
- [Dem03] J. Demsar, R. D. Averitt, A. J. Taylor, V.V. Kabanov, W. N. Kang, H. J. Kim, E. M. Choi, and S. I. Lee, *Phys. Rev. Lett.* 91, 267002 (2003)
- [Din96] H. Ding, T. Yokoya, J. C. Campuzano, T. Takahashi, M. Randeria, M. R. Norman, T. Mochiku, K. Kadowaki and J. Giapintzakis, *Nature* 382, 51 (1996)
- [Dra14] G. Drachuck, E. Razzoli, G. Bazalitski, A. Kanigel, C. Niedermayer, M. Shi and A. Keren, *Nature communication*, 5, 3390 (2014)
- [Fuj02] M. Fujita, H. Goka, K. Yamada, and M. Matsuda, *Phys. Rev. Lett.* 88, 167008 (2002)

- [Fau12] J. Faure, J. Mauchain, E. Papalazarou, W. Yan, J. Pinon, M. Marsi, and L. Perfetti, *Rev. Sci. Instrum.* 83, 043109 (2012)
- [Fan45] H. Y. Fan, *Phys. Rev.* 68, 43 (1945)
- [Fei74] P. J. Feibelman and D. E. Eastman *Phys. Rev. B* 10, 4932 (1974) [Fuj84] J. G. Fujimoto, J. M. Liu, E. P. Ippen and N. Bloembergen, *Phys. Rev. Lett.* 53,1837 (1984)
- [Fre09] J. K. Freericks, H. R. Krishnamurthy and T. Pruschke, *Phys. Rev. Lett.* 102, 136401 (2009)
- [Fuj02] M. Fujita, H. Goka, K. Yamada and M. Matsuda, *Phys. Rev. Lett.* 88, 167008 (2002)
- [Ghi12] G. Ghiringhelli, M. Le Tacon, M. Minola, S. Blanco-Canosa, C. Mazzoli, N. B. Brookes, G. M. De Luca, A. Frano, D. G. Hawthorn, F. He, T. Loew, M. Moretti Sala, D. C. Peets, M. Salluzzo, E. Schierle, R. Sutarto, G. A. Sawatzky, E. Weschke, B. Keimer and L. Braicovich, *Science* 337, 821-825 (2012)
- [Gia16] C. Giannetti, M. Capone, D. Fausti, M. Fabrizio, F. Parmigiani, and D. Mihailovic, <http://dx.doi.org/10.1080/00018732.2016.1194044>
- [Gia09] C. Giannetti, G. Coslovich, F. Cilento, G. Ferrini, H. Eisaki, N. Kaneko, M. Greven, and F. Parmigiani, *Phys. Rev. B* 79, 224502 (2009)
- [Gra11] J. Graf, C. Jozwiak, C. L. Smallwood, H. Eisaki, R. A. Kaindl, D.-H. Lee, and A. Lanzara, *Nat. Phys.* 7, 805 (2011)
- [Gra08] J. Graf, M. d’Astuto, C. Jozwiak, D. R. Garcia, N. L. Saini, M. Krisch, K. Ikeuchi, A. Q. R. Baron, H. Eisaki, and A. Lanzara, *Phys. Rev. Lett.* 100, 227002 (2008)
- [Hai88] R. Haight, J. A. Silberman and M. I. Lillie, *Rev. Sci. Instrum.* 59, 1941 (1988)
- [Has15] M. Hashimoto, E. A. Nowadnick, R. H. He, I. M. Vishik, B. Moritz, Y. He, K. Tanaka, R. G. Moore, D. Lu, Y. Yoshida, M. Ishikado, T. Sasagawa, K. Fujita, S. Ishida, S. Uchida, H. Eisaki, Z. Hussain, T. P. Devereaux and Z. X. Shen, *Nature Materials* 14, 37-42 (2015)
- [Hay92] S. M. Hayden, G. H. Lander, J. Zarestky, P. J. Brown, C. Stassis, P. Metcalf, and J. M. Honig, *Phys. Rev. Lett.* 68, 1061–1064 (1992)
- [He09] R. H. He, K. Tanaka, S. K. Mo, T. Sasagawa, M. Fujita, T. Adachi, N. Mannella, K. Yamada, Y. Koike, Z. Hussain and Z. X. Shen, *Nature Phys.* 5, 119-123 (2009)
- [He11] R. H. He, M. Hashimoto, H. Karapetyan, J. D. Koralek, J. P. Hinton, J. P. Testaud, V. Nathan, Y. Yoshida, Hong Yao, K. Tanaka, W. Meevasana, R. G. Moore,

- D. H. Lu, S.-K. Mo, M. Ishikado, H. Eisaki, Z. Hussain, T. P. Devereaux, S. A. Kivelson, J. Orenstein, A. Kapitulnik, and Z.-X. Shen, *Science* 331, 1579 (2011)
- [He13] J. He, W. Zhang, J. M. Bok, D. Mou, L. Zhao, Y. Peng, S. He, G. Liu, X. Dong, J. Zhang, J. S. Wen, Z. J. Xu, G. D. Gu, X. Wang, Q. Peng, Z. Wang, S. Zhang, F. Yang, C. Chen, Z. Xu, H. Y. Choi, C. M. Varma, and X. J. Zhou, *Phys. Rev. Lett.* 111,107005 (2013)
- [Hüf95] S.Hfer, *Photoelectron Spectroscopy principles and applications*, Springer Series in Solid-state Sciences Volume 82, 5 (1995)
- [Hüf03] S. Hüfner *Photoelectron spectroscopy: principles and applications* Berlin: Springer (2003)
- [Hub14] T. Huber, S. O. Mariager, A. Ferrer, H. Schäfer, J.A. Johnson, S. Grübel, A. Lübcke, L. Huber, T. Kubacka, C. Dornes, C. Laulhe, S. Ravy, G. Ingold, P. Beaud, J. Demsar, and S. L. Johnson, *Phys. Rev. Lett.* 113, 026401 (2014)
- [Igor] Data plot and fit obtained using Igor Pro (Wavemetrics, Lake Oswego, OR, USA)
- [Ish16] Y. Ishida, T. Saitoh, T. Mochiku, T. Nakane, K. Hirata and S. Shin, *Scientific Reports* 6, 18747 (2016)
- [Kai05] R. A. Kaindl, M. A. Carnahan, D. S. Chemla, S. Oh, and J. N. Eckstein, *Phys. Rev. B* 72, 060510 (2005)
- [Kam04] A. Kaminski, S. Rosenkranz, H. M. Fretwell, J. Mesot, M. Randeria, J. C. Campuzano, M. R. Norman, Z. Z. Li, H. Raffy, T. Sato, T. Takahashi and K. Kadowaki, *Phys. Rev. B* 69, 212509 (2004)
- [Kam06] Y. Kamihara, H. Hiramatsu, M. Hirano, R. Kawamura, H. Yanagi, T. Kamiya and H. Hosono, *J. Am. Chem. Soc.* 128 (31): 10012–10013 (2006)
- [Kan07] A. Kanigel, U. Chatterjee, M. Randeria, M. R. Norman, S. Souma, M. Shi, Z. Z. Li, H. Raffy, and J. C. Campuzano *Phys. Rev. Lett.* 99, 157001 (2007)
- [Kir10] P. S. Kirchmann, L. Perfetti, M. Wolf, and U. Bovensiepen, in *Dynamics at Solid State Surfaces and Interfaces*, edited by U. Bovensiepen, H. Petek, and M. Wolf (Wiley, New York, 2010), Vol. 1, Chap. 20, 475 (2010)
- [Kiv03] S. A. Kivelson, I. P. Bindloss, E. Fradkin, V. Oganessian, J. M. Tranquada, A. Kapitulnik, and C. Howald, *Rev. Mod. Phys.* 75 1201 (2003)
- [Kno98] E. Knoesel, A. Hotzel, and M. Wolf, *Phys. Rev. B* 57, 12812 (1998).
- [Kon00] Z. Konstantinovic, Z. Z. Li and H. Raffy, *Physica C* 341, 859 (2000)
- [Kon11] T. Kondo, Y. Hamaya, A. D. Palczewski, T. Takeuchi, J. S. Wen, Z. J. Xu, G.

- Gu, J. Schmalian and A. Kaminski, *Nature Phys.* 7, 2125 (2011)
- [Kon15] T. Kondo, W. Malaeb, Y. Ishida, T. Sasagawa, H. Sakamoto, Tsunehiro Takeuchi, T. Tohyama and S. Shin, *Nature Commun.* 6, 7699 (2015)
- [Kor05] A. A. Kordyuk, S. V. Borisenko, A. Koitzsch, J. Fink, M. Knupfer, and H. Berger, *Phys. Rev. B* 71 214513, (2005)
- [Kor07] J. D. Koralek, J. F. Douglas, N. C. Plumb, J. D. Griffith, S. T. Cundiff, H. C. Kapteyn, M. M. Murnane and D. S. Dessau, *Rev. Sci. Instrum.* 78, 053905 (2007)
- [Kor14] A. A. Kordyuk, *Low Temp. Phys.* 40 (4) 2014
- [Lan01] A. Lanzara, P. V. Bogdanov, X. J. Zhou, S. A. Kellar, D. L. Feng, E. D. Lu, T. Yoshida, H. Eisaki, A. Fujimori, K. Kishio, J.-I. Shimoyama, T. Noda, S. Uchida, Z. Hussain and Z.X. Shen, *Nature* 412, 510 (2001)
- [Lee06] P. A. Lee, N. Nagaosa, X.-G. Wen, *Rev. Mod. Phys.* 78 , 17 (2006)
- [Lee12] W. S. Lee, Y. D. Chuang, R. G. Moore, Y. Zhu, L. Patthey, M. Trigo, D. H. Lu, P. S. Kirchmann, O. Krupin, M. Yi, M. Langner, N. Huse, J. S. Robinson, Y. Chen, S. Y. Zhou, G. Coslovich, B. Huber, D. A. Reis, R.A. Kaindl, R.W. Schoenlein, D. Doering, P. Denes, W. F. Schlotter, J. J. Turner, S. L. Johnson, M. Först, T. Sasagawa, Y. F. Kung, A. P. Sorini, A. F. Kemper, B. Moritz, T. P. Devereaux, D.-H. Lee, Z. X. Shen, and Z. Hussain, *Nat. Commun.* 3, 838 (2012)
- [Li_08] Y. Li, V. Balédent, N. Bari, Y. Cho, B. Fauqué, Y. Sidis, G. Yu, X. Zhao, P. Bourges and M. Greven, *Nature* 455 , 372 (2008)
- [Li_10] Y Li, V. Balédent, G. Yu, N. Barišić, K. Hradil, R. A. Mole, Y. Sidis, P. Steffens, X. Zhao, P. Bourges & M. Greven , *Nature* 468 , 283 (2010)
- [Li_13] T. Li, A. Patz, L. Mouchliadis, J. Yan, T. A. Lograsso, I. E. Perakis, and J. Wang, *Nature (London)* 496, 69 (2013)
- [Loe96] A. G. Loeser, Z. X. Shen, D. S. Dessau, D. S. Marshall, C. H. Park, P. Fournier, and A. Kapitulnik, *Science* 273, 325–329 (1996)
- [Mad14] I. Madan, T. Kurosawa, Y. Toda, M. Oda, T. Mertelj, P. Kusar, and D. Mihailovic, *Sci. Rep.* 4, 5656 (2014)
- [Man03] A. Maniv, E. Polturak, and G. Koren, *Phys. Rev. Lett.* 91, 197001 (2003)
- [Mar96] D. S. Marshall, D. S. Dessau, A. G. Loeser, C-H. Park, A. Y. Matsuura, J. N. Eckstein, I. Bozovic, P. Fournier, A. Kapitulnik, W. E. Spicer, and Z.-X. Shen *Phys. Rev. Lett.* 76, 4841–4844 (1996)
- [Mat12] R. Matsunaga and R. Shimano, *Phys. Rev. Lett.* 109, 187002 (2012)
- [Mat15] C. E. Matt, C. G. Fatuzzo, Y. Sassa, M. Mansson, S. Fatale, V. Bitetta, X.

- Shi, X. S. Pailhes, M. H. Berntsen, T. Kurosawa, M. Oda, N. Momono, O. J. Lipscombe, S. M. Hayden, J. Q. Yan, J. S. Zhou, J. B. Goodenough, S. Pyon, T. Takayama, H. Takagi, L. Patthey, A. Bendounan, E. Razzoli, M. Shi, N. C. Plumb, M. Radovic, M. Grioni, J. Mesot, O. Tjernberg, J. Chang, *Phys. Rev. B* 92, 134524(2015)
- [Mic85] C. Michel, L. Er-Rakho, and B. Raveau, *Mat. Res. Bull.* 20, 667 (1985)
- [Mil15] T. L. Miller, C. r L. Smallwood, W. Zhang, H. Eisaki, J. Orenstein, and A. Lanzara, *Phys. Rev. B* 92, 144506 (2015)
- [Mor10] B. Moritz, T. P. Devereaux and J. K. Freericks, *Phys. Rev. B* 81, 165112 (2010)
- [Mos96] J. Mosqueira, E. G. Miramontes, C. Torrón, J. A. Campá, I. Rasines, and F. Vidal, *Phys. Rev. B* 53, 15272 (1996)
- [Mos90] M. Mostoller, J. Zhang, A. M. Rao, and P. C. Eklund, *Phys. Rev. B* 41, 6488 (1990)
- [Mou15] D. Mou, S. Manni, V. Taufour, Y. Wu, L. Huang, S. L. Bud'ko, P. C. Canfield and A. Kaminski, *PhysRevB*.91.140502 (2015)
- [Net14] E. H. da Silva Neto, P. Aynajian, A. Frano, R. Comin, E. Schierle, E. Weschke, A. Gyenis, J. Wen, J. Schneeloch, Z. Xu, S. Ono, G. Gu, M. Le Tacon, A. Yazdani, *Science* 343, 393-396 (2014)
- [Nag01] J. Nagamatsu, N. Nakagawa, T. Muranaka, Y. Zenitani, and J. Akimitsu, Superconductivity at 39 K in magnesium diboride. *Nature* 410, 63–64 (2001)
- [Nes98] W. Nessler, S. Ogawa, H. Nagano, H. Petek, J. Shimoyama, Y. Nakayama, and K. Kishio, *Phys. Rev. Lett.* 81, 4480 (1998)
- [Nor98] M. R. Norman, H. Ding, M. Randeria, J. C. Campuzano, T. Yokoya, T. Takeuchi, T. Takahashi, T. Mochiku, K. Kadowaki, P. Guptasarma and D. G. Hinks, *Nature* 392, 157 (1998)
- [Ore00] J. Orenstein, A. J. Millis, *Science* 288, 468 (2000)
- [Owe72] C. S. Owen and D. J. Scalapino, *Phys. Rev. Lett.* 28, 1559 (1972)
- [Par13] S. Parham, T. J. Reber, Y. Cao, J. A. Waugh, Z. Xu, J. Schneeloch, R. D. Zhong, G. Gu, G. Arnold, and D. S. Dessau, *Phys. Rev. B* 87, 104501 (2013)
- [Par14] S. R. Park, T. Fukuda, A. Hamann, D. Lamago, L. Pintschovius, M. Fujita, K. Yamada, and D. Reznik, *Phys. Rev. B* 89, 020506(R) (2014)
- [Per06] L. Perfetti, P. A. Loukakos, M. Lisowski, U. Bovensiepen, H. Berger, S. Biermann, P. S. Cornaglia, A. Georges and M. Wolf, *Phys. Rev. Lett.* 97, 067402 (2006)

- [Per07] L. Perfetti, P. A. Loukakos, M. Lisowski, U. Bovensiepen, H. Eisaki, and M. Wolf, *Phys. Rev. Lett.* 99, 197001 (2007)
- [Per08] L. Perfetti, P. A. Loukakos, M. Lisowski, U. Bovensiepen, M. Wolf, H. Berger, S. Biermann and A. Georges, *New J. Phys.* 10, 053019 (2008)
- [Per15] L. Perfetti, B. Sciolla, G. Birolì, C. J. van der Beek, C. Piovera, M. Wolf, and T. Kampfrath *Phys. Rev. Lett.* 114, 067003 (2015)
- [Pio15] C. Piovera, Z. Zhang, M. d'Astuto, A. Taleb-Ibrahimi, E. Papalazarou, M. Marsi, Z. Z. Li, H. Raffy, and L. Perfetti, *Phys. Rev. B* 91, 224509 (2015)
- [Ram14] J. D. Rameau, S. Freutel, L. Rettig, I. Avigo, M. Ligges, Y. Yoshida, H. Eisaki, J. Schneeloch, R. D. Zhong, Z. J. Xu, G. D. Gu, P. D. Johnson, and U. Bovensiepen, *Phys. Rev. B* 89, 115115 (2014)
- [Ram16] J. D. Rameau, S. Freutel, M. A. Sentef, A. F. Kemper, J. K. Freericks, I. Avigo, M. Ligges, L. Rettig, Y. Yoshida, H. Eisaki, J. Schneeloch, R. D. Zhong, Z. J. Xu, G. D. Gu, P. D. Johnson, U. Bovensiepen, *Nature Communications* 7, 13761 (2016)
- [Raz13] E. Razzoli, G. Drachuck, A. Keren, M. Radovic, N. C. Plumb, J. Chang, Y. B. Huang, H. Ding, J. Mesot, and M. Shi, *Phys. Rev. Lett.* 110, 047004 (2013)
- [Reb12] T. J. Reber, N. C. Plumb, Z. Sun, Y. Cao, Q. Wang, K. McElroy, H. Iwasawa, M. Arita, J. S. Wen, Z. J. Xu, G. Gu, Y. Yoshida, H. Eisaki, Y. Aiura & D. S. Dessau, *Nature Phys.* 8, 606–610 (2012)
- [Reb13] T. J. Reber, N. C. Plumb, Y. Cao, Z. Sun, Q. Wang, K. McElroy, H. Iwasawa, M. Arita, J. S. Wen, Z. J. Xu, G. Gu, Y. Yoshida, H. Eisaki, Y. Aiura, and D. S. Dessau, *Phys. Rev. B* 87, 060506(R) (2013)
- [Reb14] Reber, T. J. et al., Pre-pairing and the “Filling” Gap in the Cuprates From the Tomographic Density of States (2014)
- [Reb15] T. J. Reber, S. Parham, N. C. Plumb, Y. Cao, H. Li, Z. Sun, Q. Wang, H. Iwasawa, M. Arita, J. S. Wen, Z. J. Xu, G.D. Gu, Y. Yoshida, H. Eisaki, G.B. Arnold, D. S. Dessau, arXiv:1508.06252
- [Rez06] D. Reznik, L. Pintschovius, M. Ito, S. Iikubo, M. Sato, H. Goka, M. Fujita, K. Yamada, G. D. Gu and J. M. Tranquada, *Nature* 440, 1170-1173 (2006)
- [Ren98] Ch. Renner, B. Revaz, K. Kadowaki, I. Maggio-Aprile, and Ø. Fischer, *Phys. Rev. Lett.* 80, 3606 (1998)
- [Roh11] T. Rohwer, S. Hellmann, M. Wiesenmayer, C. Sohrt, A. Stange, B. Slomski, A. Carr, Y. Liu, L. M. Avila, M. Kallane, S. Mathias, L. Kipp, K. Rossnagel and M.

- Bauer, Nature 471, 490 (2011)
- [Rös04] O. Rösch and O. Gunnarsson, Phys. Rev. Lett. 93, 237001 (2004)
- [Rul11] F. Rullier-Albenque, H. Alloul, and G. Rikken, Phys. Rev. B 84, 014522 (2011)
- [Sea79] M. P. Seah and W. A. Dench, Surf. Interface Anal. 1, 2 (1979)
- [Seg02] G. P. Segre, N. Gedik, J. Orenstein, D. A. Bonn, R. Liang, and W. N. Hardy, Phys. Rev. Lett. 88, 137001 (2002)
- [Shu07] Shukla, A. et al., Detecting stripes in cuprates with resonant hard x- ray scattering, ESRF report HE2299 (2007), the superconducting T_c given in that report was slightly different, and refined later.
- [Sil15] E. H. da Silva Neto, R. Comin, F. He, R. Sutarto, Y. Jiang, R.L. Greene, G.A. Sawatzky, and A. Damascelli, Science 347, 282-285 (2015)
- [Sma12] C. L. Smallwood, J. P. Hinton, C. Jozwiak, W. Zhang, J. D. Koralek, H. Eisaki, D. H. Lee, J. Orenstein and A. Lanzara, Science 336, 1137 (2012)
- [Sma12_1] C. L. Smallwood, C. Jozwiak, W. Zhang, and A. Lanzara, Rev. Sci. Instrum. 83, 123904 (2012)
- [Sma14] C. L. Smallwood, W. Zhang, T. L. Miller, C. Jozwiak, H. Eisaki, D.-H. Lee, and A. Lanzara, Phys. Rev. B 89, 115126 (2014)
- [Szy06] M. H. Szymanska, J. Keeling, and P. B. Littlewood, Phys. Rev. Lett. 96, 230602 (2006)
- [Tac11] M. Le Tacon, A. Bosak, S. M. Souliou, G. Dellea, T. Loew, R. Heid, K.-P. Bohnen, G. Ghiringhelli, M. Krisch, and B. Keimer, Nat. Phys. 7, 725 (2011)
- [Tin96] M. Tinkham, Introduction to Superconductivity (McGraw-Hill, New York, 1996)
- [Tim99] T. Timusk and Bryan Stattd, Rep. Prog. Phys. 62,61 (1999)
- [Tod14] Y. Toda, F. Kawanokami, T. Kurosawa, M. Oda, I. Madan, T. Mertelj, V.V. Kabanov, and D. Mihailovic, Phys. Rev. B 90, 094513 (2014)
- [Tor13] D. H. Torchinsky, F. Mahmood, A. T. Bollinger, I. Božović and N. Gedik, Nature Materials 12, 387-391 (2013)
- [Tra94] J. M. Tranquada, D. J. Buttrey, V. Sachan, and J. E. Lorenzo, Phys. Rev. Lett. 73, 1003 (1994)
- [Tra95] J. M. Tranquada, B. J. Sternlieb, J. D. Axe, Y. Nakamura and S. Uchida, Nature 375, 561–563 (1995)
- [Tra96] J. M. Tranquada, J. D. Axe, N. Ichikawa, Y. Nakamura, S. Uchida, and B.

- Nachumi, Phys. Rev. B 54, 7489 (1996)
- [Tra04] J. M. Tranquada, H. Woo, T. G. Perring, H. Goka, G. D. Gu, G. Xu, M. Fujita and K. Yamada, Nature 429, 534–538 (2004).
- [Tri15] T. L. Miller, C. L. Smallwood, W. Zhang, H. Eisaki, J. Orenstein, and A. Lanzara, Phys. Rev. B 92, 144506 (2015)
- [Tsu00a] C. C. Tsuei and J. R. Kirtley, Rev. Mod. Phys. 72, 969–1016 (2000)
- [Tsu00b] C. C. Tsuei and J. R. Kirtley, Phys. Rev. Lett. 85, 182–185 (2000)
- [Vis10] I. M. Vishik, W. S. Lee, F. Schmitt, B. Moritz, T. Sasagawa, S. Uchida, K. Fujita, S. Ishida, C. Zhang, T. P. Devereaux, and Z. X. Shen, Phys. Rev. Lett. 104, 207002 (2010)
- [Voj09] M. Vojta, Adv. Phys. 58, 699 (2009)
- [Wan05] Y. Wang, L. Li, M. J. Naughton, G. D. Gu, S. Uchida, and N. P. Ong, Phys. Rev. Lett. 95, 247002 (2005)
- [Wan12] Y. Wang, thesis (2012) <https://dash.harvard.edu/handle/1/9823978>
- [Wis08] W. D. Wise, M. C. Boyer, Kamallesh Chatterjee, Takeshi Kondo, T. Takeuchi, H. Ikuta, Yayu Wang and E. W. Hudson, Nat Phys 4, 696 (2008)
- [Yan06] K. Y. Yang, T. M. Rice, and F. C. Zhang, Phys. Rev. B 73, 174501 (2006)
- [Yan15] S. L. Yang, J. A. Sobota, D. Leuenberger, Y. He, M. Hashimoto, D. H. Lu, H. Eisaki, P. S. Kirchmann, and Z. X. Shen, Phys. Rev. Lett. 114, 247001 (2015)
- [Yos16] T. Yoshida, W. Malaeb, S. Ideta, D. H. Lu, R. G. Moor, Z.-X. Shen, M. Okawa, T. Kiss, K. Ishizaka, S. Shin, Seiki Komiya, Yoichi Ando, H. Eisaki, S. Uchida, and A. Fujimori, Phys. Rev. B 93, 014513 (2016)
- [Zaa89] J. Zaanen and O. Gunnarsson, Physical Review B 40 (10), 739 (1989)
- [Zha13] W. Zhang, C. L. Smallwood, C. Jozwiak, T. L. Miller, Y. Yoshida, H. Eisaki, D. H. Lee, and A. Lanzara, Phys. Rev. B 88, 245132 (2013)
- [Zha14] W. Zhang, C. Hwang, C. L. Smallwood, T. L. Miller, G. Affeldt, K. Kurashima, C. Jozwiak, H. Eisaki, T. Adachi, Y. Koike, D. H. Lee & A. Lanzara, Nat Commun 5, 4959 (2014)
- [Zha16] W. Zhang, T. Miller, C. L. Smallwood, Y. Yoshida, H. Eisaki, R. A. Kaindl, D. H. Lee & A. Lanzara, Scientific Reports 6, Article number: 29100 (2016)
- [Zho15] T. Zhou, Y. Gao and J. X. Zhu, Adv. Cond. Matter Phys. 652424, 8 (2015)
- [Zha17] Z. Zhang, C. Piovera, E. Papalazarou, M. Marsi, M. d'Astuto, C. J. van der Beek, A. Taleb-Ibrahimi and L. Perfetti, <https://arxiv.org/abs/1703.07860>

Dynamique de la structure électronique, de quasi-particule dans les oxydes de cuivre supraconducteurs par spectroscopie de photoémission résolue en angle et en temps

Résumé: Les supraconducteurs à base d'oxyde de cuivre ont fait l'objet d'études approfondis mais ils restent toujours au centre de nombreux débats. Après 30 années de recherche, certaines questions scientifiques ont été éclairées, alors que d'autres restent controversées. L'évolution du paramètre d'ordre supraconducteur avec la température et le dopage en est un cas exemplaire. Dans cette thèse nous décrivons notre étude systématique de supraconducteurs à haute température critique par Angle Resolved PhotoEmission Spectroscopy (ARPES: Spectroscopie de photoémission résolue en angle) et par ARPES résolué en temps. On a mesuré du $\text{Bi}_2\text{Sr}_2\text{CaCu}_2\text{O}_{8+\delta}$ avec dopage optimale (c.a.d. montrant la T_c la plus élevée), afin d'explorer la possibilité que une photo-excitation très intense du supraconducteur crée un état avec des paires de Cooper incohérentes et sans aucune densité superfluide. La méthode expérimentale employée nous a permis de mesurer la dynamique des électrons hors équilibre et du gap supraconducteur, en fournissant des informations complémentaires à l'ARPES conventionnelle et aux mesures optiques. Nos données de ARPES résolue en temps sur $\text{Bi}_2\text{Sr}_2\text{CaCu}_2\text{O}_{8+\delta}$ montrent que une photo-excitation génère un effondrement du gap supraconducteur qui dépend du moment. La relaxation des quasi-particules acquiert une composante rapide à la fluence F de seuil ou le gap s'effondre complètement. La comparaison entre le F_{pair} et le F_{phase} par spectroscopie optique THz résolue en temps suggère que il y aurait un régime de fluence ou les paires de Cooper survivent, mais ne portant plus un courant superfluide.

Un autre défi majeur dans la physique des cuprates supraconducteurs à haute température critique (HTSCs) est la compréhension de l'état normale à haute température. Nous présentons aussi un étude ARPES du pseudo-gap proche du point nodale de la surface de Fermi dans le système $\text{La}_{2-x}\text{Ba}_x\text{CuO}_4$ (LBCO), qui montre un possible lien avec les modulations de densité de charge (stripes). Nos données suggèrent que le gap s'ouvre en dessous de la transition LTT-LTO associé à l'apparition des modulations de charge tandis que la fonction spectrale n'est pas

affecté par le modulation de la densité de spin. On observe aussi que la structure de bande dans LBCO est rénormalisé avant le "kink" à environs 70 meV. Nous corrélons cette rénormalisation en énergie et moment à l'amollissement du mode d'étirement de la liaison Cu-O.

Mots-clefs: supraconducteurs à oxyde de cuivre, pseudo-gap, quasi-particules, photo-excitation, spectroscopie de photoémission, dynamique ultra-rapide.

Electronic structures, quasi-particle and gap dynamics in copper oxides superconductors using Time and Angle Resolved Photoemission Spectroscopy

Abstract: The superconductors of the copper-oxide family have been matter of extensive investigations and are still subject of fierce debates. After 30 years of research, some issues have been settled, whereas others remain controversial. The evolution of the superconducting order parameter with temperature and doping level is an exemplary case. In this thesis, we report a systematic Time resolved Angle Resolved PhotoEmission Spectroscopy (ARPES) study of the optimally doped $\text{Bi}_2\text{Sr}_2\text{CaCu}_2\text{O}_{8+\delta}$ to explore the possibility that an intense photoexcitation of the superconductor can generate a state with incoherent copper pairs and no superfluid density. The employed experimental methods allow us to measure the dynamics of non-equilibrium electrons and of the superconducting gap, providing complementary information to conventional ARPES and optical measurement. Our time resolved ARPES data of $\text{Bi}_2\text{Sr}_2\text{CaCu}_2\text{O}_{8+\delta}$, report a momentum-dependent collapse of the superconducting gap upon photoexcitation. Interestingly, the QP relaxation develops a faster component at the threshold fluence F_{pair} where the gap has fully collapsed. The comparison between the F_{pair} and the F_{phase} extracted by tr-THz suggested the existence a fluence regime when the Cooper pairs have survived, but without holding superfluid current. A second major challenge in the physics of HTSCs is the poor understanding of the normal phase at high temperature. We also present the ARPES study of the near nodal pseudo-gap in $\text{La}_{2-x}\text{Ba}_x\text{CuO}_4$ (LBCO) to show a possible link with charge modulation (stripes). Our data show that the near nodal gap open below the LTT-LTO transition, which is linked to the formation of such modulations, instead of the one where spin modulations appear. The data show that the band structure of LBCO is affected by a renormalization setting in prior to the 70 meV kink. We were able to correlate this renormalization of the ARPES data to the region where the Cu-O bond-stretching mode soften, both in energy and momentum space.

Keywords : copper oxides superconductors, pseudo-gap, quasiparticles, photoexcitation, photoemission spectroscopy, ultrafast dynamics.